UNIVERSITY OF OKLAHOMA

GRADUATE COLLEGE

OPTIMIZING LIDAR SCANNING STRATEGIES FOR WIND ENERGY TURBULENCE MEASUREMENTS

A DISSERTATION

SUBMITTED TO THE GRADUATE FACULTY

in partial fulfillment of the requirements for the

Degree of

DOCTOR OF PHILOSOPHY

By

JENNIFER FRANCES NEWMAN
Norman, Oklahoma
2015

OPTIMIZING LIDAR SCANNING STRATEGIES FOR WIND ENERGY TURBULENCE MEASUREMENTS

A DISSERTATION APPROVED FOR THE
SCHOOL OF METEOROLOGY

BY

_____
Dr. Petra Klein, Chair

_____
Dr. Sonia Wharton

_____
Dr. Evgeni Fedorovich

_____
Dr. Mark Morrissey

_____
Dr. David Parsons

_____
Dr. Scott Greene

Dedication

To my family and friends, for their unending love and support

Acknowledgements

I would first and foremost like to thank my amazing advisors, Petra Klein and Sonia Wharton, for their patience, mentorship, and dedication throughout my dissertation research process. I have learned a huge amount from our weekly meetings, field campaigns, and the many, many paper revisions we have undergone, and will yet to undergo. Thank you for teaching me how to be a better scientist and a better writer. Thank you also to my committee for their excellent suggestions for my dissertation.

My dissertation research was made possible by a subcontract with Lawrence Livermore National Laboratory through LDRD 12-ERD-069, and I am extremely grateful for their support. I am also grateful to the many researchers I have met at conferences and corresponded with via e-mail or phone for sharing their expertise and answering my questions. Thank you to the staff of the Southern Great Plains ARM site, Rob Newsom from Pacific Northwest National Laboratory, Tim Lim from NCAR, Andreas Muschinski and Lucas Root from NorthWest Research Associates, Shiril Tichkule from the University of Colorado at Boulder, Marc Fischer and Sebastien Biraud from Lawrence Berkeley National Laboratory, the members of the Boundary Layer Remote Sensing and Simulation group at OU, and the technical support staff at Sgurr Energy, Campbell Scientific, Leosphere, and Halo Photonics for their assistance during our field campaigns.

Thank you to the faculty and staff of the School of Meteorology for making my graduate school experience so enjoyable (as enjoyable as graduate school can be,

at any rate). I am deeply grateful to my graduate school friends, many of whom I've known since I started my M.S. degree, for being great peers and confidantes. This has been a difficult experience, and I am amazed at how much we have grown in the process. Thank you to my OKC Improv family for always providing support, laughs, and a home away from home in Oklahoma City.

Thank you to my amazing family, who have always supported my endeavors, whether I'm performing in a preschool dance recital or moving to Oklahoma for six years to pursue a graduate degree. Thank you for encouraging me to follow my dreams and for being unparalleled role models throughout my life.

Finally, thank you to Tim for your love and support. Thanks for being such a great companion through all this and for alternating your dissertation meltdowns with mine to maintain general sanity.

Contents

List of Tables

List of Figures

Abstract

Turbulence has a significant effect on wind farm power production and turbine reliability. Since remote sensing devices, such as lidars, are commonly used in wind energy studies, the accurate measurement of turbulence with lidars is an important research goal in the wind energy industry. However, several factors cause lidars to measure different values of turbulence than a sonic anemometer on a tower, including the use of a scanning circle with a diameter of $\sim$100 m to estimate the three-dimensional wind field and the velocity variance contamination that can occur when a traditional Doppler-beam swinging (DBS) or velocity-azimuth display (VAD) strategy is used. In this work, several techniques for obtaining more accurate turbulence information from lidars were investigated.

One way to avoid the use of a scanning circle is to deploy multiple scanning lidars and point them toward the same volume in space to collect velocity measurements. If the lidar scans are synchronized, measurements from multiple lidars can be used to extract turbulence information. To test the ability of multi-lidar scanning strategies to measure mean wind speeds and turbulence, a lidar experiment was conducted in summer 2013 at the Southern Great Plains Atmospheric Radiation Measurement site. Two scanning strategies were tested – the tri-Doppler technique, where three scanning lidars were pointed to approximately the same point in space, and the virtual tower technique, where the lidars were pointed at several different locations above the ground.

Another field campaign was conducted at the Boulder Atmospheric Observatory in Colorado to evaluate the ability of a new six-beam lidar scanning technique, which was designed to mitigate variance contamination, as well as the DBS and VAD techniques, to measure turbulence under different atmospheric stability conditions. Measurements from two vertically profiling lidars indicated that the choice of scanning angle has significant impacts on the measurement of the horizontal variance components. Large elevation angles increase the contribution of vertical velocity to radial wind speed measurements, which can increase the u and v variance if the vertical velocity field is not uniform across the lidar scanning circle.

Based on results from the two lidar campaigns, the vertical component of turbulence can be measured accurately by using a vertically pointed lidar beam position, but the horizontal components of lidar-measured turbulence are often inaccurate under unstable conditions as a result of variance contamination and horizontal heterogeneity across the lidar scanning circle. To improve lidar variance estimates under unstable conditions, two correction techniques were developed and tested on data from the field campaigns. Similarity theory was used to estimate the approximate ratio of the horizontal variance components to the vertical variance as a function of stability, which can then be used to calculate new values of the horizontal variance components, if an accurate measure of vertical variance has been obtained. Taylor's frozen turbulence hypothesis was used to estimate changes in the vertical velocity field across the lidar scanning circle, such that the contribution

of vertical velocity to the horizontal velocity components could be taken into account. Both techniques reduced lidar variance estimates significantly and brought the estimates closer to variance estimated by sonic anemometers.

Chapter 1

Introduction

1.1 Motivation

Wind energy is expected to be one of the primary sources for renewable energy growth in the United States over the next several decades (United States Energy Information Administration 2014). The replacement of fossil fuels with wind energy will reduce CO_2 emissions, decrease water use, and reduce the United States' reliance on foreign fuel sources (U.S. DOE 2008). However, wind is an intermittent resource and is highly dependent on atmospheric inflow conditions (e.g., Petersen et al. 1998). Differences in power production are extremely important for utility operators, who must decide which combination of energy sources will best meet consumer demand at a given time. In some areas, penalties are issued to wind farm owners if the amount of available wind energy is overestimated and the wind power supply does not meet the energy demand (Lundquist et al. 2010).

In order to improve the efficiency of existing wind farms and promote wind energy growth, the U. S. Department of Energy (DOE) has established the Atmosphere to Electrons (A2e) initiative, a multi-year research project that will involve scientists at several national laboratories (U.S. DOE 2015). One of the primary research thrusts of A2e is improving the understanding of turbine inflow physics

through field campaigns. A better understanding of inflow conditions will help improve wind power forecasts and reduce wind farm operations and maintenance costs, making wind energy much more economically viable (e.g., Blanco 2009). In order to meet these objectives, accurate measurements of turbine inflow conditions are needed.

An accurate assessment of turbine inflow conditions requires an estimate of wind speeds across the heights spanned by a turbine rotor disk (typically 40 to 120 m above ground level; AGL) (Schreck et al. 2008). Traditionally, wind energy measurements have been made with cup anemometers on tall meteorological towers (International Electrotechnical Commission 2005b). However, as turbine hub heights extend further into the atmosphere, it has become more difficult and costly to build tall towers that reach these heights. In response to this issue, remote sensing devices have recently emerged as an alternative to tall towers and are now commonly employed in wind-energy studies (Emeis et al. 2007).

One frequently used remote-sensing instrument is a Doppler lidar (light detection and ranging), which utilizes the Doppler shift of backscattered laser energy to estimate the wind speed within a volume of air (Emeis 2010). Lidars can measure wind speeds up to several hundred meters above the ground and are ideally suited for estimating wind speeds across a typical turbine rotor disk area. However, the measurement of turbulence, small-scale fluctuations in wind speed, with remote-sensing devices such as lidars is not as straightforward (e.g., Sathe et al. 2011).

Turbulence can occur on a variety of temporal and spatial scales (Stull 1988), and is typically measured by sonic or cup anemometers on a tower, which estimate the amount of turbulence at a small point in the atmosphere (Kaimal and Finnigan 1994). In contrast, lidars estimate the mean wind speed of volumes of air that are typically 10–30 meters in length, and thus cannot measure small-scale, high-frequency turbulent motions (e.g., Mann et al. 2008). In addition, the scanning strategies used by most lidars, the Doppler-beam swinging (DBS) technique and the velocity-azimuth display (VAD) technique, were designed to measure mean wind speeds, not turbulence (Browning and Wexler 1968; Strauch et al. 1984). Atmospheric turbulence is extremely important in the wind energy field; turbulence has profound effects on turbine power production (e.g., Wharton and Lundquist 2012b; Clifton and Wagner 2014) and can induce damaging loads on turbine blades (e.g., Kelley et al. 2006). Wind energy developers need accurate measurements of turbulence to make decisions about wind farm design and profitability. Thus, in order to be considered a viable alternative to cup anemometers, remote sensing devices must be able to accurately measure turbulence.

The requirement for remote sensing devices to accurately measure turbulence was the primary motivation for this dissertation. Interest in turbulence measurements from lidars has increased in recent years (Sathe and Mann 2013), but few extensive field campaigns have been conducted to assess the ability of current lidar devices to measure turbulence. This dissertation summarizes results from two

field campaigns where multiple lidars were deployed at sites with extensive in-situ instrumentation for verification. Commonly used lidar scanning strategies are evaluated, as well as newer scanning strategies that have largely been used only in a research capacity. At the end of the dissertation, correction techniques are developed to improve the accuracy of turbulence measurements from current lidars. Results from this dissertation will be directly applicable to other lidar researchers, wind farm managers, and lidar manufacturers.

1.2 Research questions

The primary research objective addressed in this dissertation is determining how current lidar technology can be used to accurately measure turbulence. In order to meet this objective, the main factors that affect lidar turbulence accuracy must be considered. These factors are the following:

1. The averaging of small scales of turbulence due to the lidar measurement volume;

2. The assumption that flow is horizontally homogeneous across the scanning circle enclosed by the lidar scan;

3. Variance contamination that occurs as a result of combining information from different lidar beam positions;

4. Instrument noise.

The first item, volume averaging, is inherent to remote sensing technology and will always impact turbulence measurements from lidars. Similarly, the last item, instrument noise, defined as random, uncorrelated fluctuations in the velocity field, is a factor that cannot be easily mitigated. The effects of volume averaging can be estimated by modeling the spectral velocity tensor (e.g., Mann et al. 2010) and instrument noise can be estimated from the autocovariance function of the lidar (Lenschow et al. 2000). Items 2 and 3 can be addressed by adjusting the scanning strategy of the lidar. In order to avoid the horizontal homogeneity assumption, multiple lidars can be pointed to the same volume of air to deduce the three-dimensional velocity vector. To reduce variance contamination, a new six-beam technique (Sathe et al. 2015) can be implemented with a scanning lidar.

This dissertation focuses on the following three research questions in order to determine how lidar technology can best be used to measure turbulence:

1. What additional turbulence information can be obtained from multi-lidar scanning strategies that is not available from a vertically profiling lidar?

2. How well do the six-beam scanning technique and commonly used scanning techniques measure turbulence under different stability conditions?

3. How can available lidar data be used in new ways to correct errors in lidar turbulence measurements?

1.3 Dissertation structure

Chapter 2 of the dissertation includes a background of relevant research. A mathematical description of turbulence is provided and techniques for studying and quantifying turbulence are described. Next, a preliminary background of wind turbine structure and terminology is given and meteorological factors that impact wind energy are discussed. Lidar technology is also described and a survey of lidar scanning techniques is presented in Ch. 2. In Ch. 3, the field campaigns conducted to evaluate lidar-measured turbulence are described, while data processing methods used in the field campaigns are discussed in Ch. 4. The next three chapters address the research questions presented in Sect. 1.2. The text in these chapters is comprised of manuscripts that are currently being prepared for publication. Multi-lidar techniques are discussed in Ch. 5, which is currently being prepared for publication in *Wind Energy*. Single-lidar scanning techniques are discussed in Ch. 6, which is undergoing final revisions for submission to *Atmospheric Measurement Techniques*. Two variance correction techniques are described and evaluated in Ch. 7. Text from this chapter will likely be prepared for submission to *Boundary-Layer Meteorology*. Final discussion and conclusions are given in Ch. 8.

Chapter 2

Background

2.1 Turbulence

2.1.1 Description of atmospheric turbulence

The atmospheric boundary layer (ABL) is defined as the lowest part of the atmosphere that is directly influenced by the Earth's surface. The atmospheric wind field in the ABL can be broadly described as a combination of the mean wind, turbulence, and waves (Stull 1988). The mean horizontal wind, typically ranging in magnitude from 2 to 10 m s^{-1} in the ABL, is relatively constant on time periods of 30 min– 1 hr. (in lieu of any forcing) and is responsible for advecting heat, momentum, water vapor, pollutants, and other scalars in the boundary layer. Waves mainly transport heat and momentum in the ABL. Finally, turbulence, the rapidly fluctuating part of the wind, transports the effects of surface fluxes vertically throughout the ABL. Turbulence is responsible for distributing heat from the surface throughout the ABL during the day and distributing the effects of surface friction on the mean wind field. Turbulent transport is also largely responsible for transporting water vapor from the ground and plants to the free atmosphere to form clouds and redistributing pollen from crops (Stull 1988).

Although turbulence is a significant process for human and plant life, aviation, air pollution, and wind energy, among other fields (Stull 1988), it is perhaps one of the least understood atmospheric features in modern meteorology (Wyngaard 2010). Turbulence occurs on a variety of spatial scales, ranging from centimeters to kilometers, requiring a diverse set of in-situ and remote sensing instrumentation to study it in great detail (Kaimal and Finnigan 1994) . Further complicating matters is the fact that turbulence is a random process, producing different results for each realization in even the most tightly controlled laboratory experiment (Lumley and Panofsky 1964). Finally, turbulent processes are highly nonlinear, precluding the ability to solve turbulence equations analytically (e.g., Wyngaard 2010). However, several methods can be used to describe and quantify turbulence.

2.1.2 Techniques used to study turbulence

2.1.2.1 Reynolds averaging and Taylor's frozen turbulence hypothesis

Since turbulence is a random process, statistical methods are generally needed to describe its characteristics (Tennekes and Lumley 1972). As a first step, the wind velocities in all three directions are separated into mean and fluctuating components. For example, the wind in the zonal direction, u, would be written as follows:

$$u = \overline{u} + u', \tag{2.1}$$

where $\overline{u}$ is the mean component and u' is the fluctuating component. In a statistical sense, $\overline{u}$ is assumed to be the ensemble average and u' is the deviation from that ensemble average. However, typically only specific realizations of a time or spatial series are available and it is not possible to evaluate the ensemble average. Thus, $\overline{u}$ is usually defined as an average value over some length of time or space, while the fluctuating, or turbulent, component is defined as the deviation from this mean value. In this dissertation, the overbar will refer to temporal averaging, as only time series are discussed. This separation of wind fields into mean and fluctuating components is known as Reynolds averaging and was originally proposed by Reynolds (1894).

The degree of fluctuation in different directions can be quantified by the velocity variance $\overline{u'^2} = \sigma_u^2$. The three velocity-component variances can then be combined to form turbulence kinetic energy (TKE), e:

$$e = \frac{1}{2}(\sigma_u^2 + \sigma_v^2 + \sigma_w^2), \tag{2.2}$$

which is a measure of the kinetic energy per unit mass that is associated with 3-D turbulence (e.g., Arya 2001).

Turbulence varies in both time and space, similar to most other atmospheric variables. Since most boundary layer sensors (e.g., sonic anemometers, ground-based lidars, etc.) are stationary, it is difficult to study the spatial characteristics of turbulence. As a solution to this problem, Taylor (1938) proposed the frozen turbulence hypothesis, which states that turbulence is considered "frozen" as it

is advected past a sensor. Mathematically, Taylor's frozen turbulence hypothesis states that for any variable ξ, which could represent, e.g., the velocity variance or TKE, the material derivative is equal to 0 (Stull 1988):

$$\frac{d\xi}{dt} = 0. \tag{2.3}$$

From the definition of the total derivative, the following equation results:

$$\frac{\partial \xi}{\partial t} = -u\frac{\partial \xi}{\partial x} - v\frac{\partial \xi}{\partial y} - w\frac{\partial \xi}{\partial z}. \tag{2.4}$$

Equation 2.4 indicates that local changes in variable ξ are due only to advection by the wind. In the case of Taylor's frozen turbulence hypothesis, the assumption is made that turbulence is advected by the mean wind and that the turbulent eddies in the flow do not evolve in the time it takes the eddies to move past the sensor. Taylor's frozen turbulence hypothesis can also be expressed by relating the mean wind velocity and temporal scale of the turbulence to the spatial scale of the turbulence through the following equation:

$$P = \lambda / \overline{u}, \tag{2.5}$$

where P is the time it takes a turbulent eddy to move past a sensor, λ is the wavelength of the eddy, and $\overline{u}$ is the mean velocity of the eddy transport (Stull 1988). The frozen turbulence hypothesis works best in the surface layer and is not appropriate for a strongly turbulent mixed layer (Kaimal and Finnigan 1994).

2.1.2.2 Similarity theory

Traditionally, the method known as K-theory is used to relate turbulent fluxes to vertical gradients of different variables in the ABL, where it is assumed that turbulent transport behaves like molecular transport. If the atmosphere is neutrally stratified and turbulent fluxes are constant with height in a horizontally homogeneous surface layer, the surface-layer mean wind profile follows a logarithmic law (e.g., Kaimal and Finnigan 1994):

$$\overline{u}(z) = \frac{u_*}{k} \ln\left(\frac{z}{z_0}\right), \tag{2.6}$$

where u_* (m s^{-1}) is the friction velocity, k is the von Kármán constant, and z_0 (m) is the roughness length. Friction velocity represents the surface Reynolds stress, where the surface value of the stress is assumed to be representative of the momentum transport throughout the surface layer. The friction velocity may thus be obtained by the following equation:

$$u_* = \left(\overline{u'w'}^2 + \overline{v'w'}^2\right)^{1/4}, \tag{2.7}$$

where the turbulent fluxes are assumed to be measured near the surface. A simpler form for the friction velocity can be found by applying a coordinate rotation. Typically, three rotations can be applied to flux measurement devices, such as sonic anemometers (e.g., Kaimal and Finnigan 1994):

1. A rotation that aligns u with the mean wind direction and sets $\overline{v} = 0$;

2. A rotation that forces $\overline{w} = 0$;

3. A rotation that forces $\overline{v'w'} = 0$.

The last rotation is usually not used, as it does not have a large effect on fluxes since $\overline{v'w'}$ is close to zero over flat surfaces (Kaimal and Finnigan 1994), and the rotation can produce unrealistically large rotation angles under low wind speed conditions (Lee et al. 2004). Thus, after the first two coordinate rotations are applied and $\overline{v'w'}$ is assumed to be small, Eq. 2.7 simplifies to the following form:

$$u_* = \left|\overline{u'w'}\right|^{1/2}. \tag{2.8}$$

In a stratified atmosphere, the wind profile deviates from the logarithmic profile given in Eq. 2.6, which was the motivation for the development of Monin-Obukhov (MO) similarity theory (Monin and Obukhov 1954). MO similarity theory is based on the theory of dynamic similarity that is commonly used in fluid mechanics, which states that a series of dimensionless parameters can be used to describe the dynamics of a physical situation (e.g., Kundu and Cohen 2008). According to MO theory, the turbulence statistics of meteorological variables in the surface layer should depend only on four quantities:

1. The height above ground, z;

2. The kinematic shear stress at the surface, $\frac{\tau_0}{\rho} = -\overline{u'w'_0}$;

3. The kinematic heat flux at the surface, $\frac{H_0}{\rho c_p} = \overline{w'\theta'}$;

4. The buoyancy parameter, $\frac{g}{\theta_0}$;

where τ_0 is the surface shear stress (kg m^{-1} s^{-2}), ρ is the reference density (kg m^{-3}), H_0 is the surface heat flux (W m^{-2} = kg s^{-3}), c_p is the specific heat capacity (J kg^{-1} K^{-1} = m^2 s^{-2} K^{-1}), θ_0 is the reference potential temperature (K), and g is the gravitational acceleration (m s^{-2}). These parameters can be used to define velocity, temperature, and length scaling parameters:

$$u_* = \left(\frac{\tau_0}{\rho}\right)^{1/2} = \left|\overline{u'w'}\right|^{1/2}, \tag{2.9}$$

$$\theta_* = -\frac{H_0}{\rho c_p u_*} = -\frac{\overline{w'\theta'}}{u_*}, \tag{2.10}$$

$$L = -\frac{\theta_0}{g}\frac{(\tau_0/\rho)^{3/2}}{kH_0/\rho c_p} = -\frac{u_*^3\theta_0}{kg\overline{w'\theta'}}. \tag{2.11}$$

In order to take the effects of atmospheric moisture into account, θ can be replaced by θ_v, the virtual potential temperature, in the equations for the scaling variables.

The non-dimensionalized wind speed and temperature gradients then take the following forms:

$$\frac{kz}{u_*}\frac{d\overline{u}}{dz} = \phi_m\left(\frac{z}{L}\right), \tag{2.12}$$

$$\frac{kz}{\theta_*}\frac{d\overline{T}}{dz} = \phi_h\left(\frac{z}{L}\right), \tag{2.13}$$

where ϕ_m and ϕ_h are the similarity functions for momentum and heat, respectively. The only non-dimensional variable that can be formed from all the MO parameters is z/L, such that the dimensionless wind speed and temperature gradients become universal functions of z/L, as shown in Eqs. 2.12 and 2.13 (Monin and Obukhov 1954). This analysis can be extended to other turbulent quantities, which, when nondimensionalized by the appropriate scaling parameters, also become universal functions of z/L. Since L is defined as a stability parameter (and can also be related to the more commonly used gradient Richardson number), MO similarity theory describes nondimensional wind speed and temperature profiles, as well as turbulent quantities, as a function of stability. This relation is extremely valuable for surface layer studies, where measurements may be limited by tower height or the absence of sonic anemometers may preclude the measurement of turbulent quantities. If the appropriate similarity theory functions are known, the wind speed and temperature profiles, as well as turbulent quantities of these fields, can be deduced based on atmospheric stability information.

2.1.2.3 Spectral analysis

The turbulent boundary layer is composed of turbulent eddies of a variety of sizes. The largest eddies have spatial scales on the order of kilometers while the smallest eddies have spatial scales on the order of millimeters. Because the typical wavelengths of these turbulent eddies span several orders of magnitude, researchers

often find it useful to employ spectral analysis to examine the contribution of turbulent energy from eddies of different wavelengths. Basic spectral analysis theory, originally proposed by Taylor (1938) and reviewed by Tennekes and Lumley (1972), is presented here.

In order to study the spatial extent of turbulent eddies, the spatial covariance function, $R_{ij}(\vec{r})$, is employed. The spatial covariance function is used to define the average covariance between u_i' and u_j' at two different locations in an atmospheric flow:

$$R_{ij}(\vec{r}) = \overline{u_i'(\vec{x},t)u_j'(\vec{x}+\vec{r},t)}, \tag{2.14}$$

where the overbar denotes ensemble averaging and $\vec{x}$ and $\vec{r}$ are position and distance vectors, respectively. If the turbulence is spatially homogeneous, then R_{ij} is a function of separation distance, $|\vec{r}|$, only. The Fourier transform of $R_{ij}(\vec{r})$ gives the spatial spectral density for the fluctuating u_i' and u_j' components of the wind, $\Phi_{ij}(\vec{k})$:

$$\Phi_{ij}(\vec{k}) = \frac{1}{(2\pi)^3} \iiint_{-\infty,\infty} R_{ij}(\vec{k}) e^{-i\vec{k}\cdot\vec{r}}\, \mathrm{d}\vec{r}, \tag{2.15}$$

where $\vec{k}$ is the three-dimensional wavenumber vector, (k_1, k_2, k_3). $\Phi_{ij}(\vec{k})$ describes the contribution of atmospheric processes with different wavenumbers to the total covariance between $u_i'(\vec{x})$ and $u_j'(\vec{x}+\vec{r})$.

Of particular interest are the diagonal elements of the covariance function evaluated at $\vec{r} = (0,0,0)$, as the sum of these elements is equal to twice the TKE in the flow:

$$R_{ii}(0) = \overline{u_i' u_i'} = \overline{u'u'} + \overline{v'v'} + \overline{w'w'} = 2e = \iiint_{-\infty,\infty} \Phi_{ii}(\vec{k}) \mathrm{d}\vec{k}. \tag{2.16}$$

Tennekes and Lumley (1972) integrate $\Phi_{ii}(\vec{k})$ over a spherical shell of radius $k = |\vec{k}|$ with surface element $d\sigma$ to remove the directional dependence of $\Phi_{ii}(\vec{k})$:

$$E(k) = \frac{1}{2} \oiint \Phi_{ii}(\vec{k}) d\sigma. \tag{2.17}$$

$E(k)$ is the three-dimensional energy spectrum. The 1/2 factor in Eq. 2.17 is used so that integrating $E(k)$ over all possible k values yields the total TKE in the flow.

Generally, one-dimensional spectra, rather than three-dimensional spectra are measured. For example, the one-dimensional spectra describing variations in u' and v' in the x direction are given by the following equations:

$$P_u(k) = \frac{1}{2\pi} \int_{-\infty}^{\infty} R_u(r) e^{-ikr} dr \tag{2.18}$$

and

$$P_v(k) = \frac{1}{2\pi} \int_{-\infty}^{\infty} R_v(r) e^{-ikr} dr, \tag{2.19}$$

where $R_u(r) = \overline{u'(x)u'(x+r)}$ and $R_v(r) = \overline{v'(x)v'(x+r)}$. These spatial spectra can easily be expressed as frequency spectra by employing the temporal covariance function, $R(\tau)$:

$$S_u(f) = \frac{1}{2\pi} \int_{-\infty}^{\infty} R_u(\tau) e^{-i2\pi f\tau} d\tau, \tag{2.20}$$

where $S_u(f)$ is the one-dimensional frequency spectrum of u', f is the frequency, τ is a time lag, and $R_u(\tau) = \overline{u'(t)u'(t+\tau)}$. The conversion of $P_v(k)$ to a frequency spectrum is similar.

A schematic representation of a typical energy spectrum as a function of wavenumber in the ABL is shown in Fig. 2.1. Regions A, B, and C are referred to as the energy-containing range, inertial subrange, and dissipation range, respectively. The energy-containing range consists of the largest turbulent eddies ($\sim \Lambda$), which are typically driven by buoyancy fluxes from the ground and wind shear. Region B represents the inertial subrange, where energy is neither produced nor dissipated, but transferred from larger to smaller scales through inertial cascade. In this range, the rate of turbulence transfer from the energy-producing range of the spectrum (A) is equal to the rate of turbulence transfer to the dissipative range of the spectrum (C). Kolmogorov (1941) assumed that this energy transfer is controlled entirely by the TKE dissipation rate, ε, and determined from dimensional considerations that $E(k) = \alpha\varepsilon^{2/3}k^{-5/3}$ where α is an empirically determined constant of proportionality. Hence, the slope of $E(k)$ in the inertial subrange is proportional to $k^{-5/3}$, as shown in Fig. 2.1. In Region C, the dissipation range, kinetic energy from the smallest turbulent eddies ($\sim \eta$) is converted to heat through viscous forces.

Spectra are typically plotted with log f on the x-axis and log $fS(f)$ on the y-axis, as this representation allows for the display of a wide range of frequencies. In addition, power law relationships (e.g., the -5/3 power law in the inertial subrange)

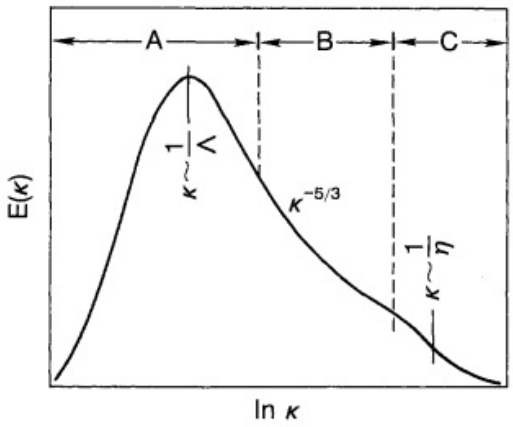

Figure 2.1: Typical energy spectrum in the atmospheric boundary layer. A, B, and C correspond to different spectral regions and Λ and η correspond to different length scales. From Kaimal and Finnigan (1994).

can be displayed as straight lines with constant slopes in a log-log graph (Stull 1988). (When log $fS(f)$ is plotted on the y-axis, the spectra follow a -2/3 law in the inertial subrange as a result of multiplication by f.) Spectra can also be scaled by appropriate factors such that spectra from boundary layers with different mean wind speeds, surface fluxes, and boundary layer heights collapse to the same set of curves. An example of normalized surface layer spectra is shown in Fig. 2.2, where spectra are normalized by u_* and ϕ_ε, the similarity function for dissipation rate, and $\phi_\varepsilon = \frac{kz\varepsilon}{u_*^3}$ where ε ($m^2 s^{-3}$) is the eddy dissipation rate. Frequencies are normalized by z and the mean wind speed, $\overline{u}$. Peaks in the spectra occur at higher and higher frequencies as stability increases and turbulent scales decrease, with the w spectra showing peaks at higher frequencies in comparison to the u and v spectra as a result of smaller turbulent length scales in the vertical.

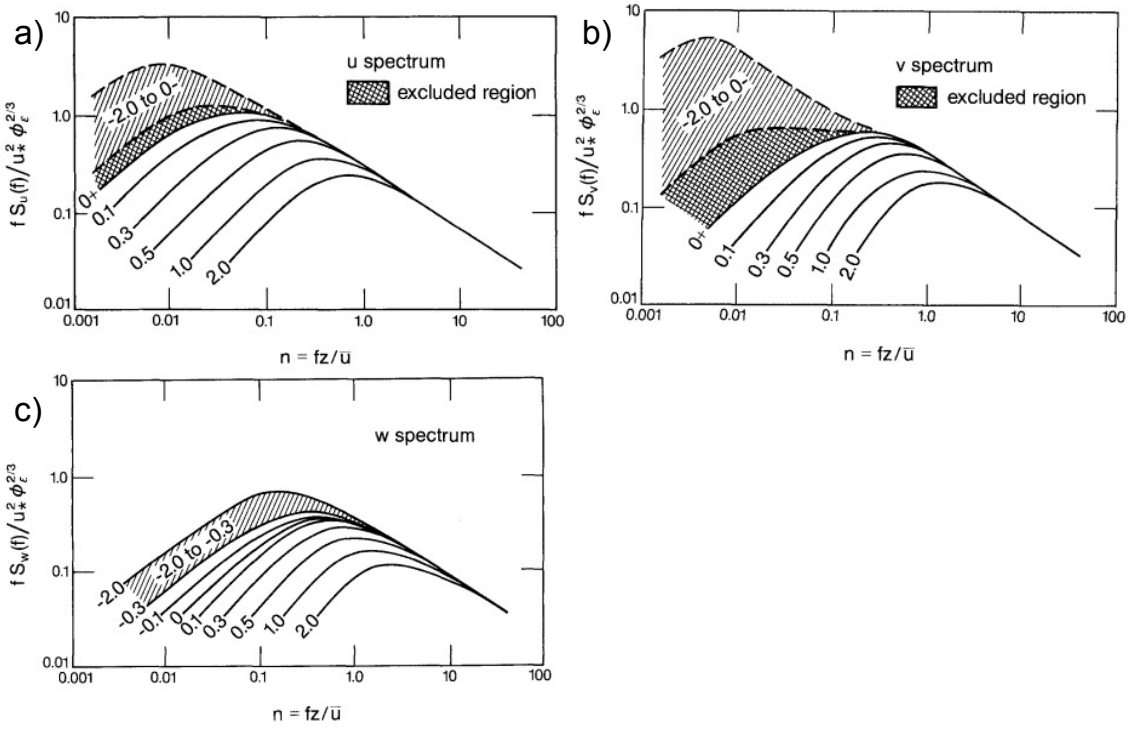

Figure 2.2: Normalized velocity spectra as a function of dimensionless frequency and z/L from the 1968 Kansas field experiment. Spectra for a) u b) v and c) w are shown. Hatched area denotes region of unstable spectra and crosshatched region indicates "excluded region", the region that separates the unstable and stable spectra. From Kaimal et al. (1972). Reprinted in Kaimal and Finnigan (1994).

2.2 Atmospheric stability

Atmospheric stability for the ABL is usually classified by either the Obukhov length, L (Eq. 2.11), or the gradient Richardson number, Ri. Ri is defined by the following equation (Arya 2001):

$$Ri = \frac{g}{\theta_0} \frac{\frac{\partial \overline{\theta}}{\partial z}}{(\frac{\partial \overline{u}}{\partial z})^2}, \tag{2.21}$$

where g (m s^{-2}) is the gravitational acceleration, as before, θ_0 (K) is the reference potential temperature, and $\frac{\partial \overline{u}}{\partial z}$ (s^{-1}) and $\frac{\partial \overline{\theta}}{\partial z}$ (K m^{-1}) are the vertical gradients of mean wind speed and potential temperature, respectively. The reference potential

temperature, θ_0, is often replaced with the reference temperature, T_0 (K), as these variables are approximately equal at the surface (Stull 2000). The potential temperature gradient can be approximated by adding the dry adiabatic lapse rate, Γ_d (K m^{-1}), to the temperature gradient, and the derivatives of temperature and wind speed can be approximated by using a finite differencing approach, as in Bodine et al. (2009):

$$Ri = \frac{g[(T_{z2} - T_{z1})/\Delta z_T + \Gamma_d)]\Delta z_u^2}{T_{z1}(u_{z2} - u_{z1})^2}, \tag{2.22}$$

where *z1* (m) and *z2* (m) correspond to two different measurement heights, and Δz_T (m) and Δz_u (m) refer to the differences in measurement levels for T (K) and u (m s^{-1}). The bulk Richardson number can be calculated by using a bulk wind shear quantity in Eq. 2.22, where $z_1 = 0$ m is assumed for wind speed, with u_{z1} = 0 m s^{-1}.

2.3 Wind turbines

2.3.1 Turbine components

In order to convert energy from the wind into electrical power, wind turbines use airfoil-shaped blades, similar to airplane wings. According to the Bernoulli effect, as air moves over the airfoil and speeds up over the curved edge of the turbine blade, an area of relatively low pressure develops, creating a lift force that moves the blades (Boyle 2004). Most modern turbines are horizontal-axis turbines, meaning that the blades rotate around a horizontal axis.

A schematic of a typical modern turbine is shown in Fig. 2.3. The turbine blades are attached to the rotor shaft by a hub. As the blades move, the rotor shaft rotates in the turbine and turns gears in a gearbox, which increases the rotational speed to a speed at which electricity can be produced. Finally, this causes a coil to rotate through a generator, which generates electricity through electromagnetic induction. These components are housed within the wind turbine nacelle. Also attached to the nacelle are typically a cup anemometer and a wind vane. These components work in conjunction with the pitch system and yaw drive to ensure that the blades are pitched at an optimal angle to decrease loads on the blades and safely harness power and that the turbine is pointing into the direction of the wind (Hau and Von Renouard 2013).

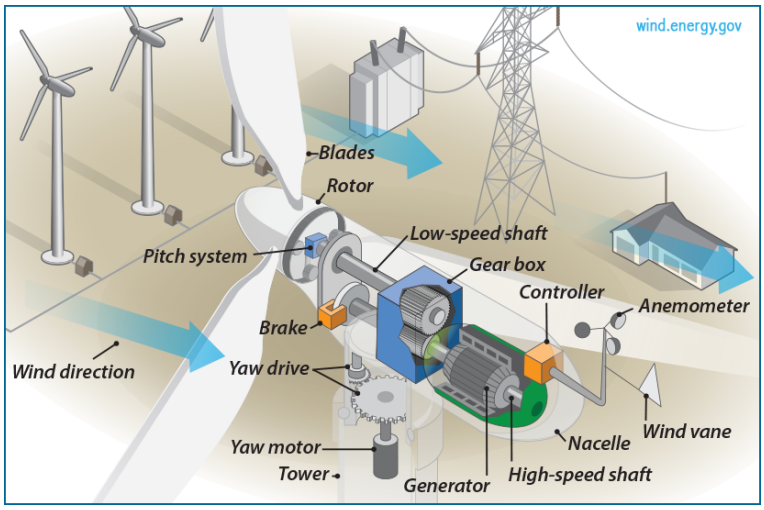

Figure 2.3: Diagram of modern wind turbine components. From wind.energy.gov.

2.3.2 Conversion of energy to power

Wind turbines convert kinetic energy in the wind to electrical power. In general, the kinetic energy, KE, of an object is given by the following equation:

$$KE = \frac{1}{2}mV^2, \tag{2.23}$$

where m is the mass of the object (kg) and V is the wind speed (m s^{-1}). For a turbine, it is assumed that air flows through a cylinder with an area, A (m^2), equal to that spanned by the turbine blades. Since the volume of a cylinder is Ah, where h (m) is the height of the cylinder, every second, air moves through a volume equal to AV. The mass of this volume of air is given by ρAV, where ρ is the density of air (kg m^{-3}). Thus, the kinetic energy intercepted by the turbine every second is given by the following equation:

$$KE_{1s} = \frac{1}{2}\rho AV^3. \tag{2.24}$$

Since power is a measure of energy per unit time, the power intercepted by the wind is equal to $P = \frac{1}{2}\rho AV^3$. However, this equation assumes that 100% of the kinetic energy intercepted by the turbine is converted to power. In reality, the turbine can only capture a fraction of the wind, which is described by the capacity factor, c_f. The equation for wind turbine power now becomes:

$$P = \frac{1}{2}c_f\rho AV^3. \tag{2.25}$$

The theoretical maximum value of the capacity factor is given by the Betz limit, $c_f = 16/27 = 59.3\%$ (Boyle 2004). The cubed factor in Eq. 2.25 implies that turbine power is proportional to the cube of the wind speed intercepted by

the blades, such that power production is extremely sensitive to changes in wind speed.

2.3.3 Determination of power curve

A turbine's power curve describes the expected power produced for a particular mean wind speed at the hub height of the turbine. The International Electrotechnical Commission (IEC) outlines rules for power performance testing of turbines, where the 10-min mean wind speed at hub height and the power produced by a turbine are recorded for a sufficient period of time to determine the power produced for different wind speed bins (International Electrotechnical Commission 2005b). These results are then used to determine the power curve for the turbine. A sample power curve is shown in Fig. 2.4.

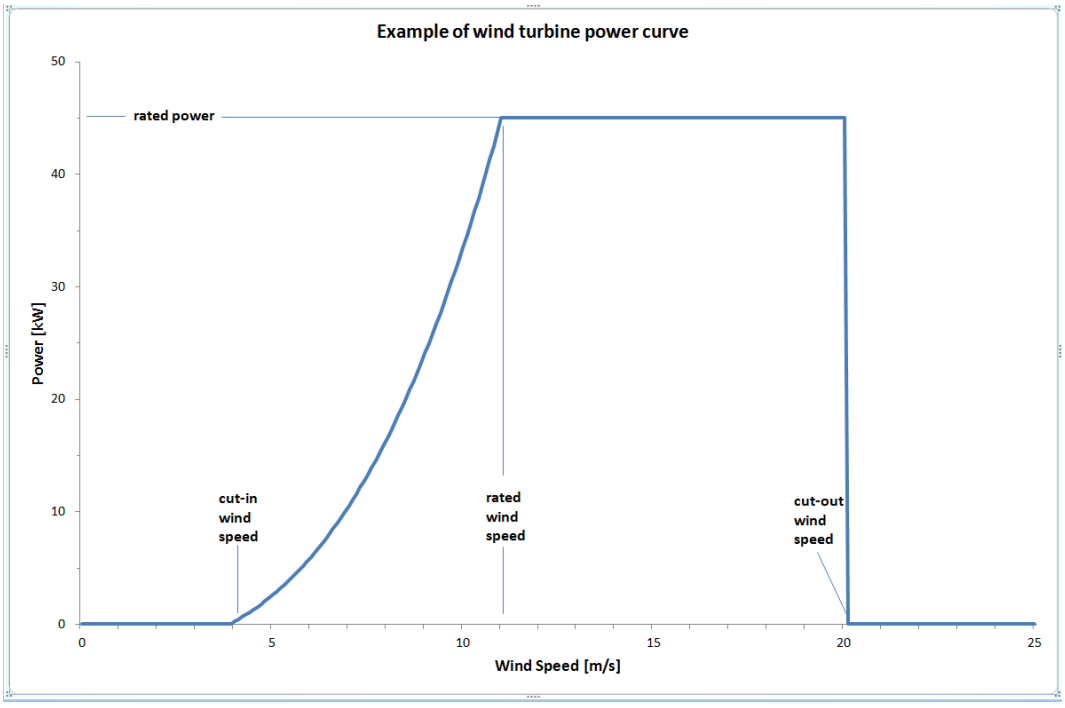

Figure 2.4: Schematic of a wind turbine power curve. From elm.eru.rl.ac.uk.

The cut-in wind speed of the turbine is the speed at which the turbine begins producing power. At this speed, the rotor is rotating fast enough to produce more power than is being consumed by the system to operate, such that the net power production becomes positive. The rated wind speed is the wind speed at which the rated power of the generator is reached. Between the cut-in and rated wind speed, the power increases approximately as the cube of the wind speed, in accordance with Eq. 2.25. Once the rated wind speed is exceeded, the turbine blades are pitched such that the power produced remains constant. At the cut-out wind speed, it becomes damaging for the turbine to continue operating, so the blades are halted and the turbine stops producing power (Hau and Von Renouard 2013).

2.3.4 Meteorological factors that impact wind energy

The power produced by a wind turbine is affected by a number of meteorological factors, including the thermodynamic stability of the atmosphere (e.g., Sumner and Masson 2006; Wharton and Lundquist 2012b; Vanderwende and Lundquist 2012; Abkar and Porté-Agel 2013; Peña et al. 2014), turbulence (e.g., Elliott and Cadogan 1990; Sheinman and Rosen 1992; Rohatgi and Barbezier 1999; Peinke et al. 2004; Clifton and Wagner 2014), and the entire wind speed profile intercepted by the turbine blades, i.e., across the rotor-disk swept area (e.g., Wagner et al. 2009; Antoniou et al. 2009; Castellani et al. 2010; Clifton et al. 2013). In this section, the effects of wind shear and turbulence on wind power production and methods for incorporating these effects into turbine power curves are discussed.

Effects of a direct measure of atmospheric stability are not discussed separately, as stability affects both the wind shear and turbulence present in turbine inflow.

2.3.4.1 Wind shear

As discussed in Sect. 2.3.3, IEC standards state that turbine power production should be estimated based on the mean wind speed at hub height (International Electrotechnical Commission 2005b). However, this standard assumes that the hub height wind speed is representative of the wind speed profile experienced across the entire rotor disk, an assumption that will often not be valid under high-shear situations or for modern turbines with larger rotor disk areas. Not surprisingly, differences in wind power production according to the amount of wind speed and directional shear have been noted in both observations (e.g., Elliott and Cadogan 1990; Wharton and Lundquist 2012b) and in simulations (e.g., Wagner et al. 2010; Clifton et al. 2013). Wind shear can either increase or decrease the power produced by a turbine, depending on the turbulence present in the turbine inflow and the mean wind speed measured at hub height (e.g., Clifton et al. 2013). Antoniou et al. (2009) showed that neglecting wind shear in the estimation of the Annual Energy Production (AEP) for a wind turbine can result in significant uncertainty and errors.

Motivated by the effects of wind shear on power production, formulas for a rotor-equivalent wind speed have been developed (Antoniou et al. 2007; Wagner et al. 2009). The general formula for the rotor-equivalent wind speed, U_{eq} is:

$$U_{eq} = \frac{1}{A}\sum_i \overline{U}_i \cdot A_i, \tag{2.26}$$

where $\overline{U}_i$ is the 10-min mean wind speed (m s^{-1}), A_i is the area corresponding to each measurement height (m^2), and A is the rotor disk area (m^2). Thus, U_{eq} is essentially an area-averaged value of the mean wind speed experienced at different points across the rotor disk.

In order to optimize the calculation of U_{eq}, Wagner et al. (2009) used a series of different wind profiles, collected at the Danish National Test Station for Large Wind Turbines in Høvsøre, Denmark, as input to the simulation of a 3.6 MW turbine with a hub height of 90 m and a rotor diameter of 107 m. Wagner et al. (2009) normalized the profiles such that the hub-height wind speed for all profiles was 7 m s^{-1} and plotted the power produced as a function of equivalent wind speed. Three different variations of Eq. 2.26 were tested with measurements taken from either one, three, or five points across the rotor disk. Wagner et al. (2009) found that the simplest formula for U_{eq}, the one shown in Eq. 2.26, provides the strongest correlation between equivalent wind speed and power. In addition, Wagner et al. (2009) showed that increasing the number of measurement points for the calculation of U_{eq} substantially improves the accuracy of power estimation. The rotor-equivalent wind speed is now commonly used in addition to the mean hub height wind speed in wind power production studies (e.g., Wharton and Lundquist 2012b; Krishnamurthy et al. 2013; Capps et al. 2014).

2.3.4.2 Turbulence

Even when the wind shear has been taken into account, wind power production can differ substantially at the same equivalent wind speed as a result of turbulence, as demonstrated in both simulations (Clifton and Wagner 2014) and at operational wind farms (Wharton and Lundquist 2012b). Mathematically, the average energy flux intercepted by the turbine increases with the presence of turbulence, as turbulence adds extra energy to the flow (de Vries 1979). However, the actual influence of turbulence on the power produced by a turbine will be affected by the power curve of the turbine. For wind speeds below the cut-in wind speed, the turbine is able to translate the extra turbulent energy into power and power is increased in comparison to non-turbulent flow at the same wind speed. In contrast, turbulence reduces power production for wind speeds above and just below the rated wind speed. When the mean wind speed approaches the rated wind speed of the turbine, the maximum power of the turbine has been reached and positive wind speed fluctuations due to turbulence (i.e., wind speed fluctuations that are greater than the mean wind speed) will not increase the power produced by the turbine. However, negative turbulent fluctuations (wind speed fluctuations that are less than the mean wind speed) will decrease the power produced by the turbine, so the net impact on power production due to turbulence near rated wind speed is negative (e.g., Albers et al. 2007; Wagner et al. 2010; Clifton et al. 2013). In addition to influencing power production, coherent structures of turbulence can also cause the turbine rotor and blades to vibrate; when these vibrations are in phase, damaging loads can

occur, reducing the turbine's reliability and expected lifetime (e.g., Kelley et al. 2004, 2006).

A method for incorporating turbulence into the turbine power curve is described in a committee draft of the IEC standard for power performance testing (International Electrotechnical Commission 2005b) and is presented in Clifton and Wagner (2014). The method involves defining a zero-turbulence power curve for a turbine such that the turbulence characteristics of different sites can be added back into the power curve for site-specific power predictions. Clifton and Wagner (2014) conducted a series of wind turbine simulations and defined the simulated power as the integral of the theoretical zero-turbulence power curve multiplied by the distribution of turbulence:

$$\hat{P}(i) = \int (P_{0,th}(u(i)) \cdot f(u(i), \sigma_u(i)), \tag{2.27}$$

where $\hat{P}(i)$ is the simulated power for wind speed bin i (W), $P_{0,th}(u(i))$ is the theoretical power curve (W), and $f(u(i), \sigma_u(i))$ is the frequency of turbulence intensity values in each bin (unitless). Since the turbine power and wind speed and turbulence distribution are known from the simulations, an iterative process can be used to find the zero-turbulence power curve. At a new site, the turbulence-specific power curve can be estimated by replacing the simulated turbulence distribution in Eq. 2.27 with the site-specific turbulence distribution and using the new power curve to determine the power produced for each wind speed and turbulence bin.

2.4 Lidar technology

Lidars (light detection and ranging) emit laser light into the atmosphere and measure the Doppler shift of the backscattered energy to estimate the mean wind velocity of volumes of air. Laser light from Doppler lidars is typically scattered from aerosols in the atmosphere, which are normally prevalent in the boundary layer (Emeis 2010). For pulsed Doppler lidars, the time series of the returned signal is split up into blocks that correspond to range gates and processed to estimate the average radial wind speed at each range gate. The sign and magnitude of the radial wind speed are determined from the Doppler shift of the returned signal with respect to the original signal (Huffaker and Hardesty 1996).

Pulsed lidars emit a short pulse of energy, then wait to receive backscattered energy from aerosols, so they cannot accurately measure wind speeds close to the lidar. Backscattered radiation from close ranges will arrive at the lidar while it is still in pulse transmission mode, and thus the lidar will not be able to receive and process this backscattered radiation. In addition, the intensity of backscattered radiation from close ranges could blind the lidar receiver (Emeis 2011). Thus, most pulsed Doppler lidars have minimum ranges of 50–100 m. In contrast, continuous wave lidars focus the laser beam at different heights to obtain wind speed measurements. Continuous wave lidars continuously receive backscattered radiation, so they can collect data at ranges as low as 10 m (e.g., Slinger and Harris 2012). However, continuous wave lidars cannot determine the direction of the Doppler

shift in the received time series, and there is a 180° ambiguity in the wind direction. The ZephIR 300, a continuous wave lidar commonly used in the wind energy industry, has an attached met station with wind direction measurements, which can provide a best estimate for the remotely measured wind direction (Slinger and Harris 2012).

Lidar technology has been used to measure wind speeds in the atmosphere since the 1960s (Huffaker and Hardesty 1996). However, it was not until the late 1990s, when large advancements in laser technology and fiber optics were made in association with the telecommunications boom, that the cost to build lidars dropped drastically (e.g. Karlsson et al. 2000). Researchers soon realized that lidars could be used for a variety of wind energy applications, including site assessment of mean wind speeds, wind directions, and turbulence, and real-time monitoring of wind profiles for turbine control (Emeis et al. 2007). Although the ability of wind lidars to accurately measure mean horizontal wind speeds has been well-documented in the literature (e.g., Sjöholm et al. 2008; Pichugina et al. 2008; Peña et al. 2009; Barthelmie et al. 2013; Machta and Boquet 2013; Sathe et al. 2015), the measurement of turbulence with lidars is still an active area of research (Sathe and Mann 2013). Loads on turbines (e.g., Kelley et al. 2006) and turbine power production (e.g., Wharton and Lundquist 2012b) are strongly affected by the three-dimensional turbulence field, but it is challenging to accurately measure this turbulence field with lidars (Sathe and Mann 2013).

In an industry that has traditionally used cup anemometers mounted on towers to measure turbulence, the use of a remote sensing device represents a significant shift in measurement technique. Lidars produce a volume-averaged value of wind speed, which precludes the measurement of high-frequency turbulent motions (e.g., Sathe et al. 2011). In addition, most commercially available lidars are programmed with scanning strategies that were optimized to measure mean wind speeds, but not turbulence.

2.4.1 Lidars used in wind energy

Several lidar companies are now specifically marketing Doppler lidars to the wind energy community. These wind energy lidars are often relatively inexpensive and easy to install and operate. Two wind energy lidars, the WindCube v2 and ZephIR 300, were used for the field experiments described in this dissertation, in addition to a research-grade scanning Halo lidar.

The Leosphere WindCube lidar is one of the most commonly used lidars in the wind energy industry. The WindCube v2 model, which was used for the experiments described in this dissertation, is a relatively inexpensive vertically profiling lidar with a low operational power consumption. The low power requirement for the WindCube v2 and other commercially available lidars (e.g., the ZephIR 300, also discussed in this section) enables users to collect data in remote locations by connecting the lidar to solar panels (e.g., Barthelmie et al. 2013; Mathisen 2013;

Wharton et al. 2015). The WindCube v2 is a pulsed Doppler lidar with a minimum range of 40 m and a maximum range of 200 m. The WindCube uses a rotating prism to employ a DBS technique (Strauch et al. 1984), which will be described in Section 2.4.2.1. More information on the WindCube lidar can be found in Cariou and Boquet (2010).

The ZephIR 300 is a continuous wave lidar that has a similar measurement range and operating power to the WindCube v2 lidar. The ZephIR 300 lidar employs a rotating mirror to conduct a 50-point VAD scan (Browning and Wexler 1968) at each measurement height, using a similar elevation angle to the WindCube lidar ($\phi = 60^\circ$ for the ZephIR compared to $\phi = 62^\circ$ for the WindCube lidar, where ϕ is the elevation angle measured from the ground). Slinger and Harris (2012) discuss the technical specifications of the ZephIR system.

The Halo Streamline Pro is a pulsed Doppler lidar equipped with a scanner that can move in both azimuth and elevation, allowing for the implementation of user-defined scanning strategies. Technical specifications for the Halo system can be found in Pearson et al. (2009). The Galion lidar is a scanning lidar manufactured by Sgurr Energy that has identical hardware to the Halo Streamline Pro lidar.

2.4.2 Commonly used scanning strategies

2.4.2.1 Doppler beam-swinging (DBS) technique

The DBS technique was traditionally used with radars (Balsley and Gage 1980; Gage and Balsley 1984; Strauch et al. 1984) and is now being applied to Doppler

lidars. In a DBS scan, the lidar beam is pointed to the four cardinal directions (north, east, south, and west) to deduce the three-dimensional wind field using the following equations:

$$u = \frac{v_{rE} - v_{rW}}{2\cos\phi}, \tag{2.28}$$

$$v = \frac{v_{rN} - v_{rS}}{2\cos\phi}, \tag{2.29}$$

$$w = \frac{v_{rN} + v_{rS} + v_{rE} + v_{rW}}{4\sin\phi}, \tag{2.30}$$

where v_{rN}, v_{rE}, v_{rS}, and v_{rW} are the radial velocities measured by the north-, east-, south-, and west-pointing beams, respectively (m s^{-1}), and ϕ is the elevation angle used by the lidar with respect to the ground (degrees). Combining the radial velocities measured at different points of the scanning circle to calculate the three-dimensional wind components involves assuming that flow is homogeneous across the scanning circle at each measurement height. Some lidars, including the WindCube v2 used in this work, add a vertically pointing beam position, v_{rz}, which provides a direct measurement of the vertical velocity, w.

2.4.2.2 Velocity-azimuth display (VAD) technique

In a VAD scan, the lidar beam is directed to different points around a scanning circle at a constant elevation angle. Browning and Wexler (1968) proposed a method for using information from a VAD scan from a Doppler radar to deduce kinematic properties of the wind field. If the wind field encompassed by the radar (or lidar) scanning circle is horizontally homogeneous, the radial velocities measured by the

instrument should create a sine curve as a function of azimuth angle (Lhermitte and Atlas 1961). This sine curve can be described by the following equation:

$$v_r(\theta) = a + b\cos(\theta - \theta_{max}), \tag{2.31}$$

where θ is the azimuthal angle of the lidar beam (degrees), a is the offset of the sine curve from the zero-velocity line (m s^{-1}), b is the amplitude of the curve (m s^{-1}), and θ_{max} is the phase shift of the curve (degrees). The horizontal wind speed, wind direction, and vertical wind speed are then derived from the following relations:

$$v_h = \frac{b}{\cos(\phi)}, \tag{2.32}$$

$$WD = \theta_{max}, \tag{2.33}$$

$$w = \frac{a}{\sin(\phi)}. \tag{2.34}$$

The values of u and v can then be derived from the horizontal wind speed, v_h, and the wind direction. Deviations of radial wind speed measurements from the sinusoidal curve can be related to turbulence (Kropfli 1986) and wave motion (Testud et al. 1980).

2.4.2.3 Issues with current scanning strategies

In the wind power industry, turbulence has traditionally been estimated from cup anemometer measurements on meteorological towers. Measurements from cup anemometers are limited by tower height and can be plagued by issues with over-speeding and slow response times, which can lead to inaccurate mean wind speed and turbulence measurements (Kaimal and Finnigan 1994). Cup anemometers also offer no direct measurement of the vertical component of turbulence and the significance of not measuring the full 3-D structure of turbulence across the turbine rotor disk is not well understood. Sonic anemometers can measure turbulence much more accurately than cup anemometers, but are also limited by tower height. In response to these issues, lidars have recently emerged as a promising alternative to cup anemometers, as they can measure wind speed and turbulence well beyond the height of meteorological towers and can be easily deployed at different locations. However, several discrepancies cause lidars to measure different values of turbulence than a cup or sonic anemometer, as discussed in Sect. 1.1. The scanning strategy used by the remote sensing device can also induce errors in the different turbulence components (Sathe and Mann 2012).

The use of either the DBS or the VAD technique introduces a number of known systematic errors into the turbulence calculations. For example, Sathe and Mann (2012) show that a "beam interference" phenomenon can occur with a DBS scan, where the same turbulent eddy is measured by two different beam positions as it

moves across the scanning circle, resulting in an increase in spectral energy at certain wavenumbers. In addition, Sathe et al. (2011) demonstrate that the calculated variance values of the wind components u, v, and w are linear combinations of all the components of the Reynolds stress tensor (i.e., the velocity variances and covariances). Therefore, the variance of the u wind component is not just affected by fluctuations in the u wind speed, but also by fluctuations in the remaining velocity components. Sathe et al. (2011) refers to this effect as variance contamination, noting that the increase in variance due to contamination can often mask the effects of volume averaging (which reduces the lidar-estimated variance), sometimes causing the lidar-estimated variance to be higher than the variance estimated by a sonic anemometer. In unstable environments, where turbulent motions tend to occur on larger spatial scales (e.g., Stull 1988), the effects of variance contamination can overcompensate for the effects of volume averaging in the u and v components and cause the lidar to overestimate the true value of the u and v variance (Sathe et al. 2011). In addition, the horizontal homogeneity assumption that is required for the VAD and DBS techniques will often be invalid, which can cause errors in wind speed estimates in complex terrain (e.g., Bingöl et al. 2009), wind turbine wakes (Lundquist et al. 2015) and under convective conditions (Wainwright et al. 2014). Horizontal heterogeneity does not have a large effect on 10- or 30-min mean wind speeds, but will impact instantaneous wind speed measurements, which are needed for the calculation of turbulence parameters (Wainwright et al. 2014).

While volume averaging is a problem inherent to remote sensing devices, the scanning strategy of a lidar can be changed to reduce the effects of variance contamination and horizontal heterogeneity. In the following sections, three research scanning strategies are described: the six-beam scanning strategy, the tri-Doppler technique, and the virtual tower technique. While these scanning strategies cannot currently be evaluated with wind energy lidars, recent research has focused on evaluating the techniques with research-grade scanning lidars (e.g., Fuertes et al. 2014; Newsom et al. 2015; Sathe et al. 2015).

2.4.3 Research scanning techniques

2.4.3.1 Six-beam scanning strategy

In order to mitigate the effects of variance contamination, Sathe (2012) developed a new lidar scanning strategy that uses six beam locations to estimate the 3-D turbulence field. A brief description of the development of the technique is presented here.

In a homogeneous atmosphere, the radial velocity values measured by a lidar completing a VAD or DBS scan should take the following form (Weitkamp 2005):

$$v_r = u\sin\theta\cos\phi + v\cos\theta\cos\phi + w\sin\phi. \tag{2.35}$$

Taking the variance of Eq. 2.35 gives the following equation:

$$\overline{v_r'^2} = \overline{u'^2}\cos^2\phi\sin^2\theta \; + \; \overline{v'^2}\cos^2\phi\cos^2\theta \; + \; \overline{w'^2}\sin^2\phi \; + \; 2\overline{u'v'}\cos^2\phi\cos\theta\sin\theta$$
$$+ \; 2\overline{u'w'}\cos\phi\sin\phi\sin\theta \; + 2\overline{v'w'}\cos\phi\sin\phi\sin\theta, \tag{2.36}$$

where primes denote deviations from a temporal mean, the overbar denotes temporal averaging, and θ and ϕ refer to the azimuth and elevation angle of the lidar beam, respectively. For each beam position (i.e., for each combination of θ and ϕ), the variances and covariances create a set of six unknown quantities. In order to independently solve for the six unknown variables, Sathe (2012) creates a set of six equations with six different combinations of θ and ϕ. The optimum values for θ and ϕ are selected by using a minimization algorithm to determine the combination of parameters that minimizes the random errors in the variance estimates. The optimal configuration is as follows: five beams at an elevation angle of 45° that are equally spaced 72° apart (i.e., located at azimuths of 0, 72, 144, 216, and 288°), and one vertically pointed beam. This scanning strategy is hereafter referred to as the six-beam technique.

In the six-beam technique, the variance of u, v, and w is determined by solving Eq. 2.36 for $\overline{u'^2}$, $\overline{v'^2}$, and $\overline{w'^2}$. This results in the following equations:

$$\overline{u'^2} = -0.4\overline{v_{r1}'^2} + 1.05(\overline{v_{r2}'^2} + \overline{v_{r5}'^2}) + 0.15(\overline{v_{r3}'^2} + \overline{v_{r4}'^2}) - \overline{v_{r6}'^2}, \tag{2.37}$$

$$\overline{v'^2} = 1.2\overline{v_{r1}'^2} - 0.25(\overline{v_{r2}'^2} + \overline{v_{r5}'^2}) + 0.65(\overline{v_{r3}'^2} + \overline{v_{r4}'^2}) - \overline{v_{r6}'^2}, \tag{2.38}$$

$$\overline{w'^2} = \overline{v_{r6}'^2}, \tag{2.39}$$

where subscripts 1–6 refer to the beam positions, with beams 1–5 spaced 72° apart in the scanning circle and beam 6 pointing vertically upward. The variance values can also be rotated such that u is aligned with the mean wind direction and $\overline{v}$ is forced to 0. This coordinate rotation uses the first coordinate transformation that is typically applied to sonic anemometer data (e.g., Kaimal and Finnigan 1994; Foken 2008) and multiplies the coordinate transformation matrix by its transpose to obtain the coordinate rotation for the variance components (Sathe et al. 2015). The rotated variance components are described as follows:

$$\overline{u'^2}_{rot} = \overline{u'^2}\sin^2\Theta + \overline{v'^2}\cos^2\Theta + \overline{u'v'}\sin 2\Theta, \tag{2.40}$$

$$\overline{v'^2}_{rot} = \overline{u'^2}\cos^2\Theta + \overline{v'^2}\sin^2\Theta - \overline{u'v'}\sin 2\Theta, \tag{2.41}$$

$$\overline{w'^2}_{rot} = \overline{w'^2}, \tag{2.42}$$

where Θ is the mean wind direction and the subscript *rot* refers to variance components in the rotated coordinate system.

Sathe et al. (2015) evaluated the six-beam technique at the Danish National Test Center for Large Wind Turbines in Høvsøre, Denmark using the WindScanner lidar developed at Denmark Technical University. The WindScanner was deployed 41 m west of a high-frequency 2-D cup anemometer mounted at 89 m on a meteorological tower. A wind vane on the tower was used to separate the cup anemometer wind speeds into the zonal and meridional directions, but an estimate

of the vertical velocity could not be obtained from the tower set-up. Sathe et al. (2015) calculated the turbulence from the WindScanner lidar in two ways: using the six-beam technique, and using a VAD technique. The VAD technique was used to calculate a different value of u, v, and w for each complete scan; these values were then used to calculate the variance over a 30-min time period.

Sathe et al. (2015) found that the six-beam technique measured higher values of variance than the VAD technique for all stability classes, with values that were closest to the cup anemometer values under stable conditions. These findings are in contrast to observations presented by Sathe et al. (2011) for the same site, which indicate that lidars measure variance most accurately under unstable conditions due to the larger turbulent motions present under unstable conditions. Sathe et al. (2015) attribute this difference to the wind directions selected for each of the studies; while only westerly wind directions were analyzed in the six-beam study, Sathe et al. (2011) analyzed only data that were associated with easterly wind directions. Since the WindScanner used by Sathe et al. (2015) was located 2 km east of the coast of the North Sea, data from the westerly wind direction could be influenced by the land-sea transition. As discussed by Sathe et al. (2015), this transition likely caused an internal boundary layer to develop, which, in conjunction with the current atmospheric stability regime, would affect the turbulent scales of motion intercepted by the lidar and the cup anemometer.

2.4.3.2 Tri-Doppler lidar technique

In the tri-Doppler technique, beams from three lidars are pointed to approximately the same volume of air. Since three lidars are used in the tri-Doppler technique and there are three unknown wind components, u, v, and w, a set of three equations can be used to solve for the wind components. In this work, the dual-Doppler lidar technique described by Calhoun et al. (2006) was extended to include an additional lidar. In this technique, the radial velocity measured by each lidar, $v_{r,lidar}$ (m s^{-1}), is written as the dot product between the true three-dimensional velocity vector, $\mathbf{U}$ (m s^{-1}), and the unit vector of the lidar system, $\mathbf{r_{lidar}}$ (unitless):

$$\begin{aligned} v_{r,lidar} &= \mathbf{r_{lidar}} \cdot \mathbf{U} \\ &= u\cos(\phi)\sin(\theta) + v\cos(\phi)\cos(\theta) \\ &+ w\sin(\phi), \end{aligned} \tag{2.43}$$

where u, v, and w are the zonal, meridional, and vertical components of the velocity, respectively, ϕ is the elevation angle of the lidar beam, and θ is the azimuthal angle of the lidar beam, measured from true north. After the radial velocity equations are written for each scanning lidar, a set of three equations and three unknowns is obtained and the equations can be solved to estimate the three true wind components.

Data from the tri-Doppler technique can also be used to estimate mean wind speed profiles. Since at least two of the lidars will scan at non-zero elevation angles, the height above ground of the lidar beams increases with increasing distance

from each lidar. Thus, the radial velocity data measured by these two lidars at different ranges can be combined using a dual-Doppler technique to calculate a mean horizontal wind speed profile. The dual-Doppler technique uses Eq. 2.43 with the assumption that $w = 0$ m s^{-1}. The calculation also involves assuming that the flow is horizontally homogeneous across the area encompassed by the lidars; neither assumption is likely valid for short time scales. However, if the lidar data are averaged over an appropriate amount of time (e.g., 1 min-1 hour), the averaged flow can be assumed to be horizontally homogeneous with a mean vertical velocity of 0 m s^{-1}. During the multi-lidar campaign, 1-min mean wind speeds and wind directions were strongly correlated for measurements from different parts of the ARM site and 1-min mean vertical velocities were approximately 0 m s^{-1}. Thus, a 1-min averaging time was used for the dual-Doppler technique in this work, as discussed in Ch. 5.

Several tri-Doppler experiments were conducted in the last decade. Mikkelsen et al. (2008) describe the development of the Windscanner facility, a set of three lidars that can be deployed to estimate the three-dimensional turbulence field at different sites. The Windscanner facility consists of three or more lidars mounted on steerable platforms so that the lidar beams can be pointed to different heights. Mann et al. (2008) tested the Windscanner facility concept by pointing three WindCube pulsed Doppler lidars toward a sonic anemometer at 78 m AGL at the Test Station for Large Wind Turbines in Høvsøre, Denmark. Mann et al. (2008) examined the ratio between the velocity spectra measured by the sonic anemometer and

the lidars and also modeled this ratio, using the Mann turbulence model (Mann 1994) and a spatial weighting function. The ratio of the sonic spectra to the lidar spectra was close to one for low frequencies, up to approximately 0.05 Hz, before decreasing rapidly for high frequencies as the effects of spatial averaging began to dominate. Mann et al. (2008) were able to model this change in the spectrum ratio relatively accurately. Similar to Mann et al. (2008), Khadiri-Yazami et al. (2013) deployed three WindCube lidars on maneuverable platforms at a site in Germany. Initial results show good agreement between the lidar-derived wind speeds and wind speeds from a cup anemometer on a tower at 135 m AGL.

Fuertes et al. (2014) used three Halo Streamline Pro lidars at the Experimental Site for Atmospheric Research in Cabauw, The Netherlands to conduct a tri-Doppler scan technique. Fuertes et al. (2014) used spatial and temporal filters to approximate the wind speed that would be measured by sonic anemometers on the measurement site tower if they were subject to the same temporal resolution and volume averaging constraints as the Halo lidars. Turbulence statistics determined from the tri-Doppler technique and the filtered sonic data compared favorably at a height of 60 m AGL. Velocity spectra also agreed well up to a frequency of approximately 0.1 Hz, when the filtered sonic and tri-Doppler spectra dropped off rapidly and the unfiltered sonic measurements continued throughout the inertial subrange.

2.4.3.3 Virtual tower technique

The virtual tower technique involves the use of three scanning lidars to build a "virtual tower" that consists of multiple measurement heights. This strategy is similar to the tri-Doppler technique, except the beams are periodically moved to different heights to obtain a wind speed and turbulence profile. The lidars used in a virtual tower scan point consistently toward the same azimuth angle and periodically change the elevation angle to move to a different measurement height in what is referred to as a range-height indicator (RHI) scan. The lidars can also change the azimuth angle of the RHI scan to build a virtual tower at another location.

Traditionally, the virtual tower technique has only been used to estimate mean wind speed profiles. With a focus on measuring mean wind speed profiles in an urban area for dispersion model verification, Calhoun et al. (2006) deployed two WindScanner Doppler lidars during the Joint Urban 2003 (JU2003) experiment in Oklahoma City. The lidars performed a series of overlapping RHI scans to measure the horizontal wind speed at several virtual towers in the downtown Oklahoma City area. Because the focus of the study was to measure mean wind speed profiles, not turbulence, Calhoun et al. (2006) did not aim to measure precisely the same volumes of air at the same point in time. Similarly, Newsom et al. (2015) deployed two scanning Halo Streamline Pro lidars at the Southern Great Plains Atmospheric Radiation Measurement (ARM) site and conducted intersecting RHI scans to build a series of virtual towers that enclosed a "virtual box" for

a dual-Doppler analysis. Since two lidars were used, only two of the three velocity components could be independently determined. Thus, Newsom et al. (2015) assumed that the vertical velocity was zero at the surface (e.g., the impermeability condition) and used the incompressible form of the continuity equation ($\nabla \cdot \mathbf{u} = 0$) to determine the profile of the vertical velocity. In comparison to JU2003, Newsom et al. (2015) had in-situ data from a sonic anemometer and radiosondes, as well as remotely sensed data from a radar wind profiler at the ARM site. One-min averages of the horizontal wind speed and direction determined from the dual-Doppler data compared well with data from these instruments at the site, although a consistent positive bias was noted in mean wind speed measurements from the sonic anemometer. Newsom et al. (2015) note that this bias likely occurred because the sonic anemometer had not been recently calibrated.

Chapter 3

Field experiments

In order to evaluate the ability of lidars to measure atmospheric turbulence, two field experiments were conducted at locations with instrumented meteorological towers. An overview of the field experiments undertaken for this work is given in this chapter and data processing methodology is described in Ch. 4. Results from the experiments are discussed in Ch. 5 and 6. Instruments used to evaluate turbulence measurements during the experiments are summarized in Table 3.1.

3.1 Lower Atmospheric Boundary Layer Experiment

The Lower Atmospheric Boundary Layer Experiment (LABLE), took place in two phases: LABLE 1 was conducted from 18 September to 13 November 2012 and LABLE 2 was conducted from 12 June to 2 July 2013. During the LABLE campaigns, several remote sensing devices were deployed at the Southern Great Plains ARM site in northern Oklahoma. The primary goals of the LABLE campaign were to evaluate the ability of different instruments to measure turbulence and mean wind speeds, to investigate differences in turbulence caused by upwind surface roughness, and to better characterize the vertical turbulence structure of the

Instrument	Campaign	Measurement Range	Temporal Resolution	Scanning Strategy	Owner
WindCube v2 Pulsed Doppler Lidar	LABLE 2 LATTE	40–200 m 20-m range gates	1 Hz Full scan: 4 s	DBS 62° elevation angle	LLNL
ZephIR 300 Continuous Wave Doppler Lidar	LATTE	10–200 m Variable range gate size	0.07 Hz Full scan: 15 s	VAD 60° elevation angle	LLNL
Halo Streamline Pro Scanning Doppler Lidar	LABLE 2 LATTE	105 m–9.6 km 30-m range gates	1 Hz	Various	OU, ARM
Galion Scanning Doppler Lidar	LABLE 2	105 m–4 km 30-m range gates	1 Hz	Various	Sgurr Energy
Gill Windmaster Pro 3-D Sonic Anemometer	LABLE 2	4, 25, and 60 m	10 Hz	—	Lawrence Berkeley National Laboratory
RM Young 3-D Sonic Anemometers	LATTE	50, 100, 150, 200, 250, and 300 m, NW booms	30 Hz	—	OU
Campbell Scientific CSAT3 3-D Sonic Anemometers	LATTE	50, 100, 150, 200, 250, and 300 m, SE booms	60 Hz	—	NCAR

Table 3.1: Overview of instruments used to evaluate different scanning strategies during LABLE 2 and LATTE.

nocturnal boundary layer (Klein et al. 2015). LABLE 2 was a multi-lidar experiment designed to test different scanning strategies and results from LABLE 2 are discussed in Ch. 5.

The ARM site is operated by the Department of Energy and serves as a field site for an extensive suite of various in-situ and remote sensing instruments (Mather and Voyles 2013). The location of the ARM site in northern Oklahoma is shown in Fig. 3.1a. The ARM site is relatively flat and is surrounded by a patchwork of farmland. During the spring of 2013, much of Oklahoma was under a persistent drought (Oklahoma Climatological Survey 2013), and crops and pasturelands surrounding the ARM site were short in the following summer; as such, spatial heterogeneity in canopy roughness (due to the patchiness of crop planting) was not expected to significantly impact flow at the site during LABLE 2.

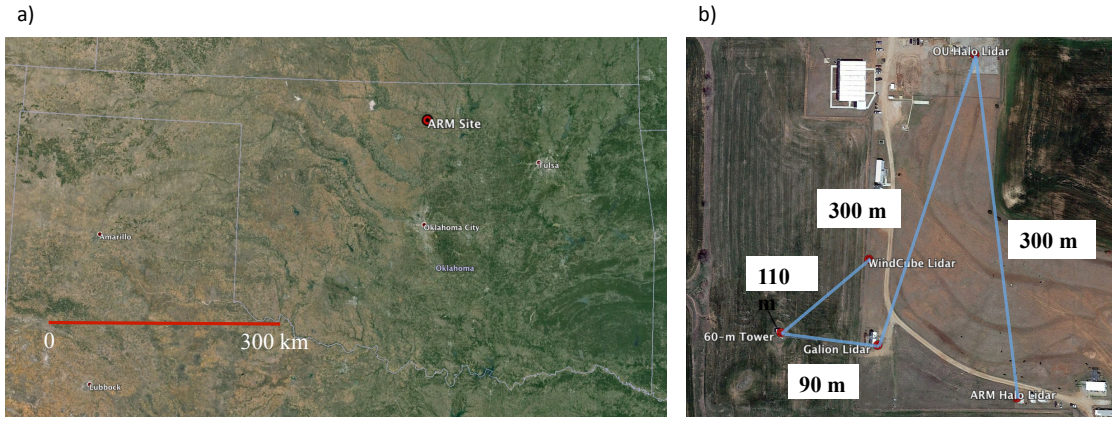

Figure 3.1: a) Google Earth image of the state of Oklahoma. Location of Southern Great Plains ARM site is denoted by red marker. b) Google Earth image of the central facility of the Southern Great Plains ARM site. Instrument locations are denoted by red markers. Approximate distances between instruments are indicated by blue lines and labels.

Locations of the lidars deployed during LABLE 2 are shown in Fig. 3.1b. The ARM Halo lidar is a scanning lidar operated by the ARM site and is nearly identical to the Halo Streamline Pro lidar owned by the University of Oklahoma (OU). The Galion lidar is a scanning lidar rented by OU that is also very similar to the OU Halo lidar. A WindCube v2 lidar owned by Lawrence Livermore National Laboratory (LLNL) was deployed at the ARM site from 12 November 2012 to 8 July 2013 and was also used for turbulence analysis (Table 3.1).

3.1.1 Data availability and synoptic-scale features

During LABLE 2, three scanning strategies were evaluated. A summary of the data availability for the different instruments and scanning strategies is shown in Fig. 3.2. The tri-Doppler, six-beam, and virtual tower scanning strategies were each evaluated for approximately one week. Throughout the evaluation of the tri-Doppler and six-beam techniques, the scanning lidars were all pointed vertically during the daytime hours for a different experiment, so there are large gaps in the scanning lidar data availability from approximately 1500 to 0000 UTC every day (Fig. 3.2). However, in general, the lidar data availability was nearly 100% during LABLE 2. (The gap in WindCube data from 21 to 23 June was related to a power issue at the ARM site.) In contrast, the sonic data had large gaps in availability, particularly at 60 m. During the week of 12 June, a transmission line was being fixed on the 60-m tower, which had caused gaps in the 25- and 60-m sonic data streams since January 2013. The 25- and 60-m sonic data streams came back

online on 18 June, but the 60-m sonic data began having transmission issues again on 28 June. Thus, unfortunately, there was not a sufficient amount of sonic data available for comparison during LABLE 2.

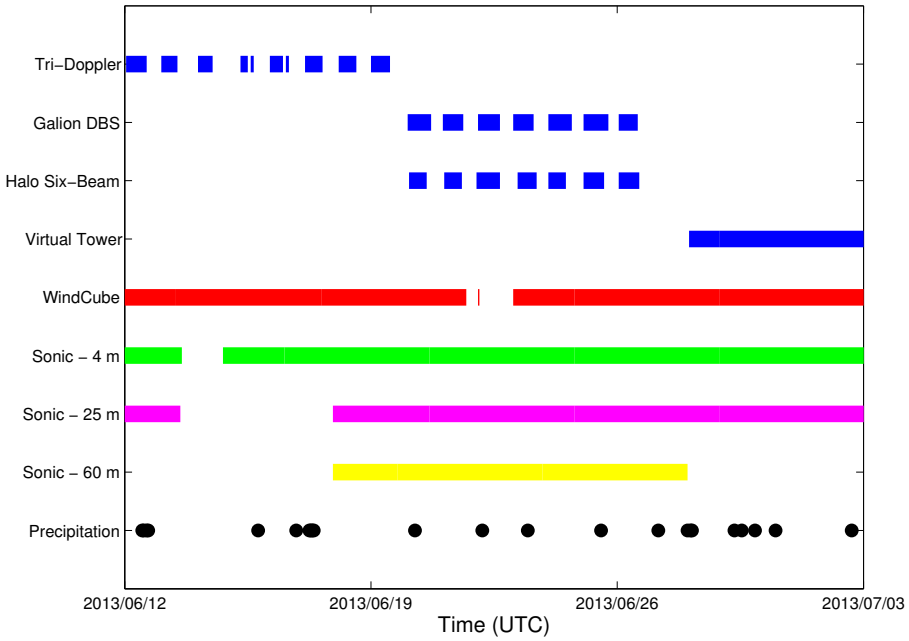

Figure 3.2: Summary of 100-m lidar and 4-, 25-, and 60-m sonic data availability during LABLE 2. Solid bars indicate hourly periods for which data availability for the vertical wind speed component was greater than 80% after application of the signal-to-noise ratio (SNR) and spike filters described in Sect. 4.2. Black circles indicate hourly periods in which rainfall was measured at the ARM site.

The mean wind speeds, wind directions, and stability conditions experienced at the ARM site during LABLE 2 are summarized in Fig. 3.3. (Data from the WindCube lidar are shown, as this was the only lidar that used the same scanning strategy for the entire experiment.) For the majority of LABLE 2, winds were southerly and south-southeasterly with wind speed maxima occurring during the overnight hours in association with the low-level jet (LLJ). From 17 to 27 June, wind speeds increased from 40 to 200 m in association with the passage of short-wave impulses from a series of upper-level troughs located off the coast of California. From 28

June to 3 July, an upper-level trough stalled and began amplifying to the east of the Southern Plains, resulting in a shift to northerly winds (Fig. 3.3b). A distinct diurnal pattern was present in the stability measured at the ARM site, with stable conditions present overnight and unstable conditions present during the daytime hours (Fig. 3.3c).

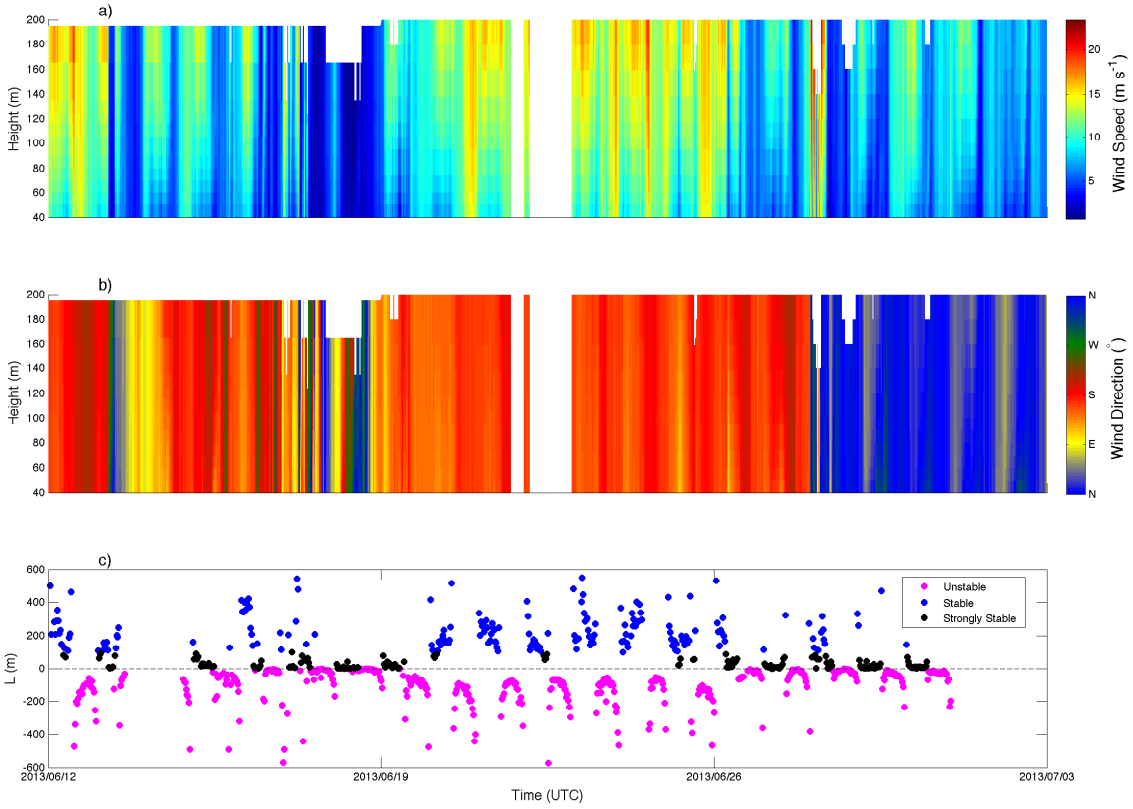

Figure 3.3: Time-height cross-sections of a) 30-min mean wind speed and b) 30-min mean wind direction from WindCube lidar data during LABLE 2. Time series of MO length calculated from 4-m sonic data is shown in c), with stability classifications described in Sect. 4.5.

3.1.2 Scanning strategies

For the first week of the experiment, the OU Halo and Galion lidars were pointed 105 m above the ARM Halo lidar, which corresponds to the first useable range gate of the Halo lidars. While the ARM Halo lidar pointed directly upward to obtain

a direct measurement of the vertical velocity, the OU Halo and Galion lidars obtained measurements of the radial velocity along their line of sight (Fig. 3.4). The tri-Doppler technique (Sect. 2.4.3.2) was used to derive turbulence measurements at 105 m AGL. Measurements along the OU Halo and Galion lidar beams were also used with a dual-Doppler technique to calculate mean wind speed profiles.

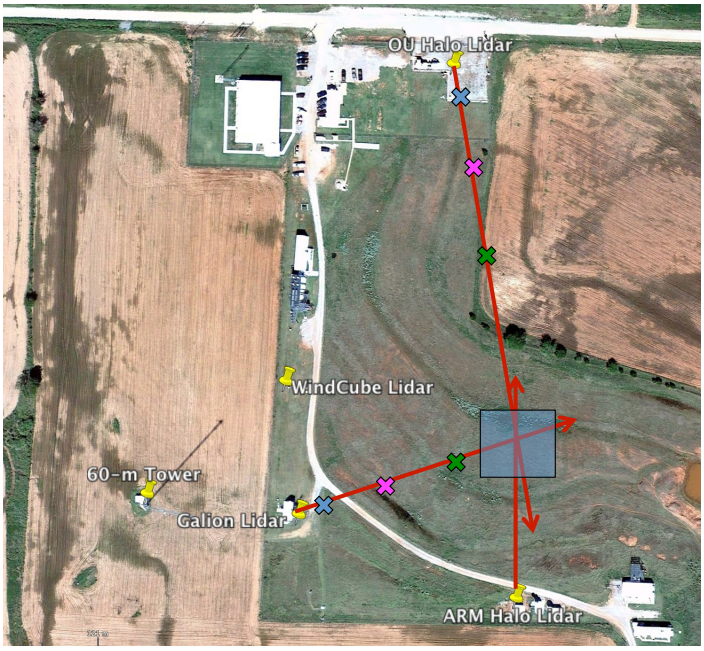

Figure 3.4: Schematic of the tri-Doppler technique tested during LABLE 2. Approximate pointing angles of lidars are indicated by red lines with arrows and the analysis area at 105 m AGL is highlighted by blue box. Colored symbols along OU Halo and Galion lidar beams illustrate matching measurement heights used to calculate wind profiles with the dual-Doppler technique.

Next, the six-beam scanning strategy (Sect. 2.4.3.1) was evaluated with the OU Halo lidar. The Galion lidar mimicked the DBS technique used by the WindCube lidar but employed an elevation angle of 45° to match the elevation angle of the OU Halo lidar and to maximize overlapping measurement heights among the different lidars.

Finally, all three scanning lidars were used to build a "virtual tower" (Sect. 2.4.3.3) over the WindCube lidar (Fig. 3.5), where the beams were moved to different heights AGL every 10 min. The sampled heights were 60, 100, 200, 350, and 500 m. The 60-m height corresponded to a sonic anemometer on the tower (Table 3.1), while the 60-, 100-, and 200-m heights corresponded to WindCube measurement heights. The additional heights above 200 m were used to sample the LLJ.

Figure 3.5: Schematic of the virtual tower technique tested during LABLE 2. Approximate pointing angles of lidars are indicated by red lines with arrows and two sample analysis areas are highlighted by blue boxes.

3.2 Lower Atmospheric Turbulence and Thermodynamics Experiment

The Lower Atmospheric Turbulence and Thermodynamics Experiment (LATTE) was conducted from 10 February to 28 March 2014, with a small-scale extension

of the project from 28 March to 28 April 2014. LATTE was conducted at the Boulder Atmospheric Observatory (BAO), a NOAA facility located in Erie, Colorado (Fig. 3.6a). The BAO site is situated approximately 25 km east of the foothills of the Rocky Mountains. Although the diurnal heating cycle can induce upslope and downslope winds in the vicinity of a mountain range (e.g., Defant 1951), these effects are only expected to influence flow at the BAO when the synoptic-scale pressure gradient is weak (Hahn 1981). During LATTE, the synoptic pattern in Colorado was fairly active (Table B.1) and flow throughout the boundary later appeared to be mainly associated with the upper-level flow pattern (not shown).

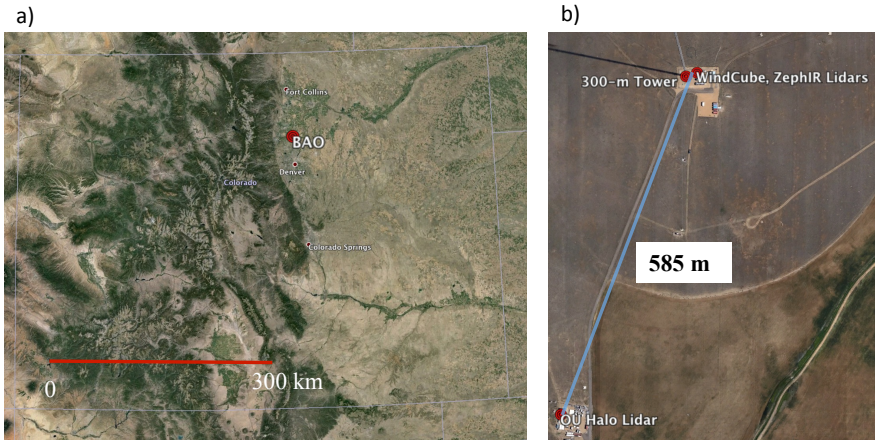

Figure 3.6: a) Google Earth image of the state of Colorado. Location of BAO site is denoted by red marker. b) Google Earth image of the BAO site. Instrument locations are denoted by red markers. Approximate distance between instruments is indicated by blue line and label. Only the initial location of the WindCube lidar is shown.

One of the primary goals of LATTE was to evaluate the accuracy of lidar turbulence measurements. Thus, the 300-m tower at the BAO was instrumented with 3-D sonic anemometers at six different heights. As a result of a collaboration with the National Corporation for Atmospheric Research (NCAR), we were able to mount two sonic anemometers at each measurement height on opposite booms

such that at each height there would be at least one set of 3-D sonic anemometer measurements that were not influenced by the wake of the tower. The OU Halo lidar and LLNL WindCube lidar were deployed at the BAO for LATTE, in addition to a continuous wave ZephIR 300 lidar owned by LLNL and several instruments owned by NCAR (Table 3.1). The OU Halo lidar was located approximately 600 m south-southwest of the 300-m tower so that it could be used to verify wind speeds from a wind profiler. The WindCube was located in the same enclosure as the 300-m tower from 14 to 28 February 2014, then moved to the same location as the OU Halo lidar from 1 March to 28 April 2014. The ZephIR remained in the tower enclosure for the duration of the experiment (Fig. 3.6b).

Wind speed comparisons between identical ZephIR lidars, one located in the tower enclosure and one located just northwest of the OU Halo lidar, indicated that there was no significant flow variability between the OU Halo location and the location of the tower (Fig. 3.7). (Note that in this dissertation, regression lines are calculated with the assumption that the y-intercept is 0, as this is the convention normally followed in wind energy studies.) Despite the uniformity of mean flow across the site, variance values between the lidars and the sonic anemometers differed strongly for westerly wind directions, likely because the lidars in the enclosure were in the wake of the tower for westerly winds and flow was from the direction of the Rocky Mountain foothills (Fig. 3.6). Thus, in statistical analyses of the variance from LATTE, values that were associated with wind directions between 225° and 315° were excluded. This resulted in an exclusion of 30% of the

variance data overall and 10% of the data for the time periods examined in this work.

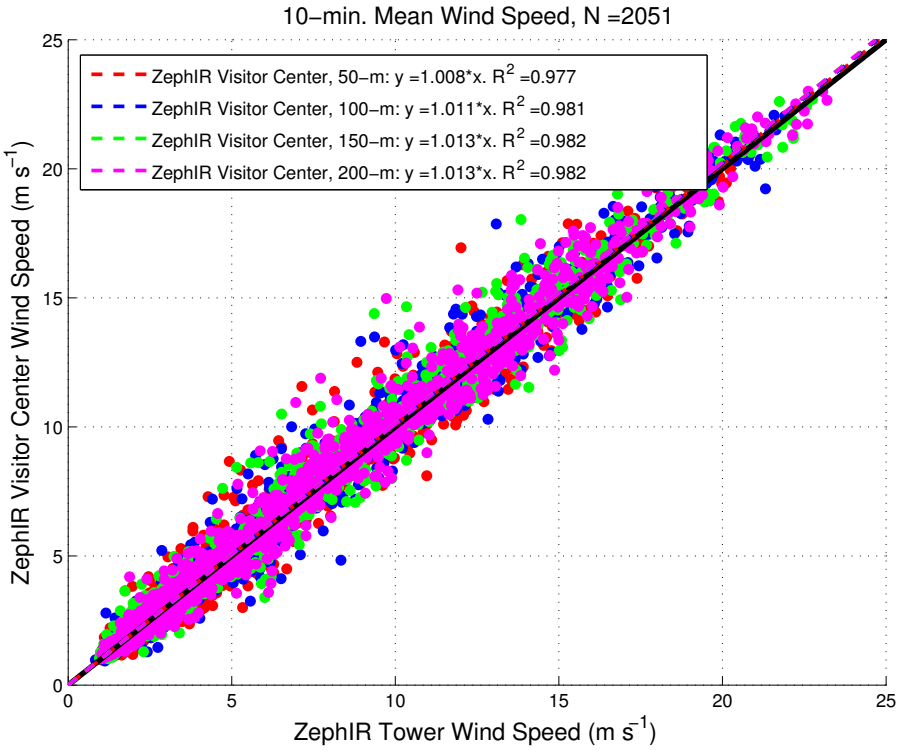

Figure 3.7: Comparison of 10-min mean wind speeds measured by two ZephIR lidars at the BAO from 14 February to 3 March 2014.

3.2.1 Data availability and synoptic-scale features

Data availability for the lidars and sonic anemometers during LATTE is shown in Figs. 3.8 and 3.9 for 100 and 200 m data, respectively. (Availability is shown for both 100 and 200 m, as data availability changed substantially with height.) In contrast to LABLE 2, the WindCube and Halo lidars had significant data availability issues at the BAO. The WindCube had nearly 100% availability at 100 m, but approximately 15% availability at 200 m. This is likely due to the low aerosol

count at the BAO; most aerosols at the site are produced by surface-based anthropogenic activities, and the aerosol concentration thus decreases steadily with height. Westerly flow from the Rocky Mountain foothills also results in cleaner air with a low aerosol concentration (Brown et al. 2013). The Halo lidar also had issues with data availability, particularly at 100 m (Fig. 3.8). The focus height of the Halo lidar was set to 300 m during the experiment, meaning that the SNR was maximized at 300 m. Thus, the measurements made by the Halo lidar at 100 m had lower SNR values than the measurements made at 200 m, which was closer to the focus height, and many 100 m data points were removed as a result. The ZephIR did not appear to have any problems with data availability, although the actual quality of the collected data at 200 m is questionable. The ZephIR lidar does not output the SNR as a parameter in the data files, so an SNR filter could not be applied to the ZephIR velocity data. The north sonics came online on 15 February and the south sonics came online on 1 March and had nearly 100% data availability for the remainder of the experiment (Figs. 3.8, 3.9).

Several frontal passages and rain/snow showers occurred at the BAO during LATTE. A summary of the major synoptic-scale events is given in Table B.1. (Snowfall did not usually register as measureable precipitation at the BAO, so local meteorological reports as well as ceilometer data at the BAO were examined to approximate times of snowfall.) Most of these cold frontal passages were also associated with upper-level troughs and large shifts in wind direction (Fig. 3.10b). In contrast to the ARM site, stability conditions at the BAO were often defined as

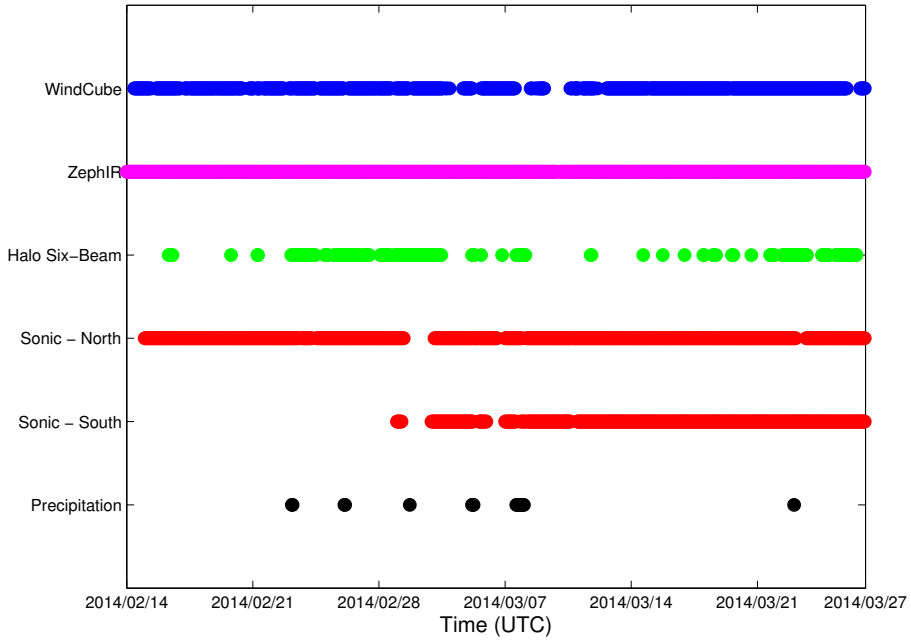

Figure 3.8: Summary of 100-m lidar and sonic data availability during LATTE. Circles indicate hourly periods for which data availability for the vertical wind speed component was greater than 80% after application of the SNR and spike filters described in Sect. 4.2. Black circles indicate hourly periods in which rainfall was measured at the BAO.

stable or neutral, with only 8% of the 30-min averaging periods being defined as unstable (Fig. 3.10). While LABLE 2 took place during the summer, LATTE took place during the winter, when the ground was often snow-covered and convective mixing was limited, particularly at the beginning of the experiment.

3.2.2 Scanning strategies

The scanning strategies used by the lidars during LATTE were largely constant throughout the experiment. The WindCube and ZephIR conducted DBS and VAD scans, respectively. The Halo lidar implemented the six-beam strategy (Sect. 2.4.3.1) for the entire experiment, with the exception of 8–11 and 26–28 March, when it was pointed vertically to obtain high-frequency vertical velocity measurements.

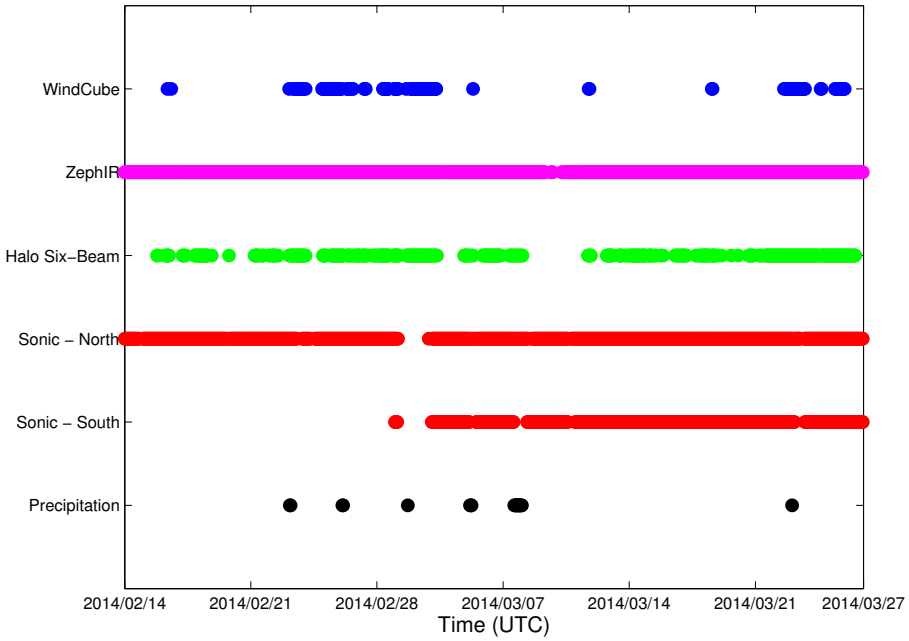

Figure 3.9: As in Fig. 3.8, but for 200 m data.

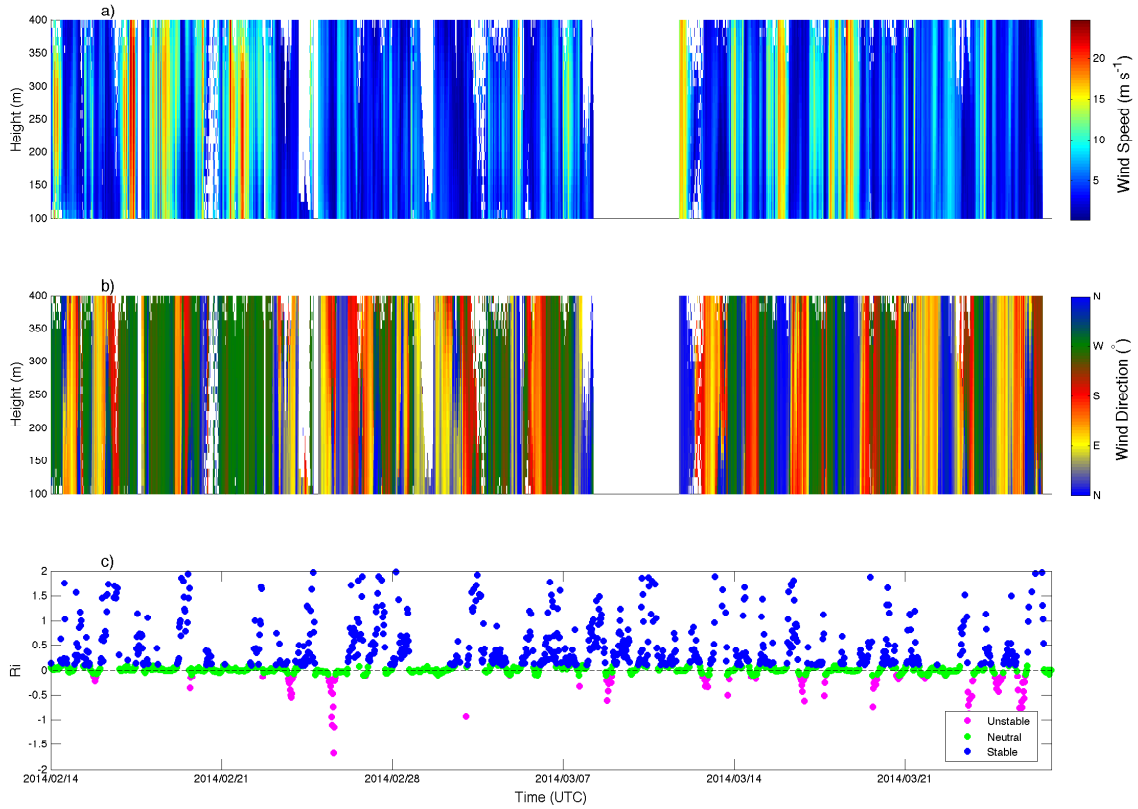

Figure 3.10: Time-height cross-sections of a) 30-min mean wind speed and b) 30-min mean wind direction from Halo lidar data during LATTE. Time series of *Ri* is shown in c), with stability classifications described in Sect. 4.5.

Chapter 4

Data processing methods

Similar data processing techniques were used for both LABLE 2 and LATTE. In this chapter, data processing and stability classification methods for both experiments are discussed.

4.1 Temporal interpolation

The actual sampling frequencies of the sonic anemometers and lidars drifted by approximately 0.5-1 Hz around their prescribed sampling frequencies throughout the measurement campaigns, which is problematic for the calculation of variance. Thus, the raw wind speed data from the different instruments were linearly interpolated onto temporal grids with constant spacing.

As the WindCube lidar moves to a different beam location approximately every 1 s, the u, v, and w WindCube velocities were interpolated to a 1-s grid. The WindCube beam points vertically approximately every 4 s to obtain a direct measurement of the vertical velocity, so the vertical beam data were interpolated to a 4-s grid. Similarly, the ZephIR velocities were interpolated to a 15-s grid. When the OU Halo, Galion, and ARM Halo lidars were used to evaluate the multi-lidar scanning strategies, radial velocities were interpolated to a 1-s grid, identical to

that used for the WindCube lidar. During the six-beam portion of LABLE 2, the Galion u, v, and w velocities were interpolated to a 4-s grid while the Galion vertical beam velocities were interpolated to a 30-s grid. (The scanning lidars take longer to steer the beam to different locations as they use a mechanical pedestal to steer the beam rather than a constantly rotating prism or mirror.) Similarly, the radial velocity data from each beam location of the OU Halo lidar were interpolated to a 30-s grid when the lidar was evaluating the six-beam scanning strategy.

Data from the north (south) sonic anemometers at the BAO were first interpolated to a grid with a frequency resolution of 30 Hz (60 Hz). Next, 10 Hz sonic anemometer data streams were created by averaging three (six) data points at a time. The 10 Hz data streams were used in further calculations, as they served to reduce high-frequency noise in the sonic anemometer data as well as reduce processing time. (Variance calculated from the 10 Hz data streams did not differ significantly from variance calculated from the raw sonic anemometer data streams.) The sonic anemometer data at the ARM site were also interpolated to a 10-Hz grid. No averaging was needed for the ARM sonic data, as the output frequency of the ARM sonic anemometers is already 10 Hz (Table 3.1).

4.2 Quality control

The spike filter developed by Højstrup (1993) and adapted by Vickers and Mahrt (1997) was used to flag outliers in the data. A 10-min window was shifted through the raw lidar and sonic anemometer data, and any point that was more than 3.5

standard deviations from the 10-min block average was flagged as a possible spike and removed from the dataset. This process was repeated until no more spikes were detected. For each pass through the spike filter, the factor of 3.5 standard deviations was increased by 0.1 standard deviations.

By default, WindCube radial velocities that were associated with Signal-to-Noise ratios (SNRs) lower than -23 dB were flagged as missing values. For the scanning lidars, SNR thresholds were set to -23 and -17 dB for the horizontal and vertical beams, respectively. The ZephIR lidar obtains an estimate of the mean noise level by taking measurements with the shutter closed before each full scan. Only signals with power that exceeds a threshold of five standard deviations above this mean noise level are used to estimate the velocity (Slinger and Harris 2012).

Lidar data that were collected when rain gauges at the different field sites recorded precipitation were flagged as erroneous data. As Doppler lidars use the Doppler shift from aerosols to estimate radial velocity, they are adversely affected by the presence of precipitation particles, which can result in beam attenuation and increased vertical velocities (e.g., Huffaker and Hardesty 1996; Pearson et al. 2009). Data were also manually screened for days containing frontal passages or mesoscale weather systems, such as squall lines. These days were excluded from the analysis for two reasons: 1) Lidar data availability tended to be very poor after frontal passages, likely as a result of low aerosol loading and 2) The goal of the field experiments was to evaluate lidar-measured variance that was associated with

atmospheric turbulence, not large shifts in wind speed or wind direction that were associated with synoptic-scale weather systems.

4.3 Coordinate rotation

A coordinate rotation was applied to the sonic anemometer and lidar data to reduce the effects of alignment and tilt errors on the variance and mean wind speed estimates. The data were first rotated such that u was aligned with the 10-min mean wind direction and the mean meridional wind speed, $\overline{v}$, was set to zero. This rotation takes the following form (Kaimal and Finnigan 1994; Wilczak et al. 2001; Foken 2008):

$$u_1 = u_m \cos\alpha + v_m \sin\alpha, \tag{4.1}$$

$$v_1 = -u_m \sin\alpha + v_m \cos\alpha, \tag{4.2}$$

$$w_1 = w_m, \tag{4.3}$$

where the subscript 1 refers to the wind speed components after the first rotation has been applied, the subscript m refers to the original measured components, and $\alpha = \tan^{-1}(\overline{v_m}/\overline{u_m})$. In the next step, the coordinate axes were rotated such that $\overline{w}$ was equal to zero:

$$u_2 = u_1 \cos\beta + w_1 \sin\beta, \tag{4.4}$$

$$v_2 = v_1, \tag{4.5}$$

$$w_2 = -u_1 \sin\beta + w_1 \cos\beta, \tag{4.6}$$

where $\beta = \tan^{-1}(\overline{w_1}/\overline{u_1})$. From this point forward, u will be considered the streamwise velocity component, v the crosswise component, and w the vertical component. In comparisons with the six-beam technique in Ch. 6, only the first coordinate rotation was applied to the lidar and sonic data to be consistent with the coordinate rotation used by Sathe et al. (2015) (Sect. 2.4.3.1).

4.4 Variance estimation

In order to mitigate the effects of random errors on variance calculations, Vickers and Mahrt (1997) recommend averaging turbulent fluxes over a period of time that is longer than the local averaging length, T, which represents the largest scale of turbulent motions that are included in the variance estimates. In practical terms, T is the averaging time that is used to calculate mean values from which the turbulent fluxes are derived. In this work, the variance of each velocity component was defined as the mean value of $u_i'^2$ (calculated using T = 10 min) over a 30-min period, with i = 1, 2, 3 corresponding to the u, v, and w estimates, respectively. The typical averaging period for wind energy studies is 10 min, but a 30-min averaging period was used in this work to reduce the effects of noise on variance estimates, as in Sathe et al. (2015).

Mesoscale motions can also induce errors in variance calculations, as the mean of each variable can change significantly over the averaging period used to calculate variance as a result of a frontal passage or wind direction shift (Vickers and Mahrt 1997). Thus, raw wind speed data were detrended using a linear detrend method for each hour-long record. The detrending method served to reduce high variance values that were associated with large shifts in wind speed or wind direction.

4.5 Stability classification

During LABLE 2, the Monin-Obukhov length, L, was used to define stability (Eq. 2.11). Stability thresholds were defined as follows:

Unstable: $-600 < L < 0$

Neutral: $|L| \geq 600$

Stable: $100 \leq L < 600$

Strongly Stable: $0 \leq L < 100$

(No category for strongly unstable conditions was included, as the majority of the multi-lidar measurements were taken during overnight, stable conditions.) Unfortunately, maintenance work was being performed on the 60-m tower during the experiment, so the only sonic data that were consistently available throughout the evaluation of the multi-lidar techniques were from the 4-m eddy covariance tower (Fig. 3.2) and L was calculated from the 4-m sonic.

During LATTE, sonic anemometer data were consistently available at multiple heights, so L could have also been used as a stability parameter. However, the Obukhov length requires an estimation of surface heat and momentum fluxes, which are small under stable conditions. In addition, the intermittency of turbulence under stable conditions can cause errors in the flux calculations (Mahrt 1985), which can then translate to errors in the Obukhov length calculation. Since the BAO frequently experienced strongly stable conditions, the gradient Richardson number, Ri, was used as a stability parameter for LATTE instead (Eq. 2.22). The bulk approximation was used in Eq. 2.22 to eliminate the extremely large negative Ri values that were often produced at the BAO under unstable conditions as a result of the small difference between u_{z2} and u_{z1}.

Temperatures for the calculation of Ri were obtained from auxiliary instrumentation on the meteorological tower at the BAO, as these instruments measure temperature more directly than a sonic anemometer. Sonic anemometers estimate temperature from the time it takes the acoustic pulses to travel from one probe to another, where this travel time is affected by both water vapor in the atmosphere and wind transverse to the sonic path (Kaimal and Finnigan 1994). The BAO tower contains temperature/relative humidity sensors and RM Young propeller/vane instruments at 10 and 100 m. Stability classes for LATTE were defined as follows:

Unstable: $Ri < -0.1$

Near-Neutral: $-0.1 \leq Ri \leq 0.1$

Stable: $Ri > 0.1$

A critical Richardson number of 0.25 is often used to define the upper limit of stability at which the onset of turbulence can occur; however, experimental evidence suggests that there may be no critical Richardson number and that turbulence can exist in flows with $Ri \geq 1$ (Galperin et al. 2007). Regardless of the definition of the critical Richardson number, turbulence under very stable conditions tends to be intermittent and difficult to quantify with traditional techniques (Mahrt 1985). As quantifying turbulence under very stable conditions requires different techniques (e.g., Howell and Sun 1999), extremely stable cases from LATTE were excluded from statistical analyses for this dissertation and will be analyzed separately in future work. For a field campaign in northwest Colorado, Mahrt and Vickers (2006) noted that the probability distribution of σ_w, the standard deviation of the vertical velocity, became relatively independent of Richardson number when *Ri* exceeded unity, signaling the start of a new stability regime. Sonic anemometer data at the BAO indicates that the magnitude of *w* variance becomes relatively independent of *Ri* once *Ri* exceeds unity, similar to Mahrt and Vickers (2006). Thus, cases with $Ri > 1$ were deemed to be extremely stable and removed from statistical analyses.

Chapter 5

Multi-lidar techniques

5.1 Introduction

Two main research questions are investigated in this chapter: 1) What turbulence and mean wind speed information can be obtained through the use of a multi-lidar scanning strategy? and 2) What research still must be done to determine the ability of multi-lidar scanning strategies to accurately measure turbulence and mean wind speed profiles for wind energy? Research-grade scanning lidars, while prohibitively expensive, are generally required for the implementation of multi-lidar scanning strategies. Thus, multi-lidar scanning strategies must provide accurate mean wind speed and turbulence information at heights spanning a turbine rotor disk in order to offset the cost of purchasing or renting the scanning lidars at a wind farm.

This chapter explores the use of two multi-lidar scanning strategies to measure turbulence and mean wind speed profiles in the lower boundary layer, i.e., the portion of the atmosphere that is most important for wind energy studies. During LABLE 2, the tri-Doppler technique (Sect. 2.4.3.2) and the virtual tower technique (Sect. 2.4.3.3) were evaluated with scanning lidars. The experiment marked the first time the tri-Doppler and virtual tower techniques were evaluated under vastly

different stability conditions at the same site and compared to measurements from a commercially available lidar. The evaluation of both techniques at the same site allows for the comparison of the techniques under similar atmospheric conditions with the same scanning lidars. Comparisons to data obtained from a commercially available lidar are extremely valuable, as they directly indicate the advantage of using a multi-lidar scanning technique as opposed to a single commercially available lidar.

5.2 Scanning strategy evaluation

5.2.1 Tri-Doppler technique

The tri-Doppler technique (Sect. 2.4.3.2) was analyzed from 12 to 16 June 2013. Between approximately 0000 and 1500 UTC (7 pm and 10 am local time) every day, the OU Halo and Galion lidars were set to perform a constant horizontal stare scan at a point approximately 105 m above the ARM Halo lidar (Fig. 3.4). During this time, the ARM Halo lidar performed a constant vertical stare scan directly above the lidar. (For the remainder of the day, the OU Halo and Galion lidars were set to a vertical stare mode for a different experiment.) The range gate length for the OU Halo and Galion lidars was set to 30 m to match the range gates of the ARM Halo lidar. Unfortunately, the lidar alignment was not verified until the next week of the experiment, so there was some uncertainty regarding the true bearing of the scanning lidars to the ARM Halo lidar. However, the corrections made

to the lidar bearings later in the experiment were all less than 5°, resulting in an uncertainty of less than 20 m at the location of the ARM lidar.

First, data from the OU Halo and Galion lidars were combined with a dual-Doppler technique (Sect. 2.4.3.2) to estimate mean wind speed and wind direction profiles. These profiles were compared to similar profiles from the WindCube lidar and the ARM Halo lidar, which conducts a 3-min VAD scan every 15 minutes. Time-height cross-sections of the 1-min mean horizontal wind speed and wind direction from the dual-Doppler technique and the WindCube DBS scans are compared to the 15-min instantaneous wind speed and wind direction from the ARM Halo VAD scans in Figs. 5.1-5.5. The vertical resolutions of the dual-Doppler, WindCube, and ARM VAD wind profiles were 10 m, 20 m, and 26 m, respectively.

LLJs were present on most nights of the experiment and were sometimes associated with wave-like features (perhaps gravity waves) in the horizontal wind speed field. Gravity waves, which can cause periodic fluctuations in wind speed, temperature, and pressure, often occur in the nocturnal boundary layer as a result of stable stratification. Waves form on the interface between air of different densities and can persist for long periods of time if they become ducted, or reflected, by gradients of temperature or wind speed (Markowski and Richardson 2010). One striking example of these waves can be seen in Fig. 5.2. On 13 June 2013, a strong LLJ was evident between the hours of 0300 and 0700 UTC before an approaching cold front impinged on the LLJ and caused a rapid shift in wind direction from

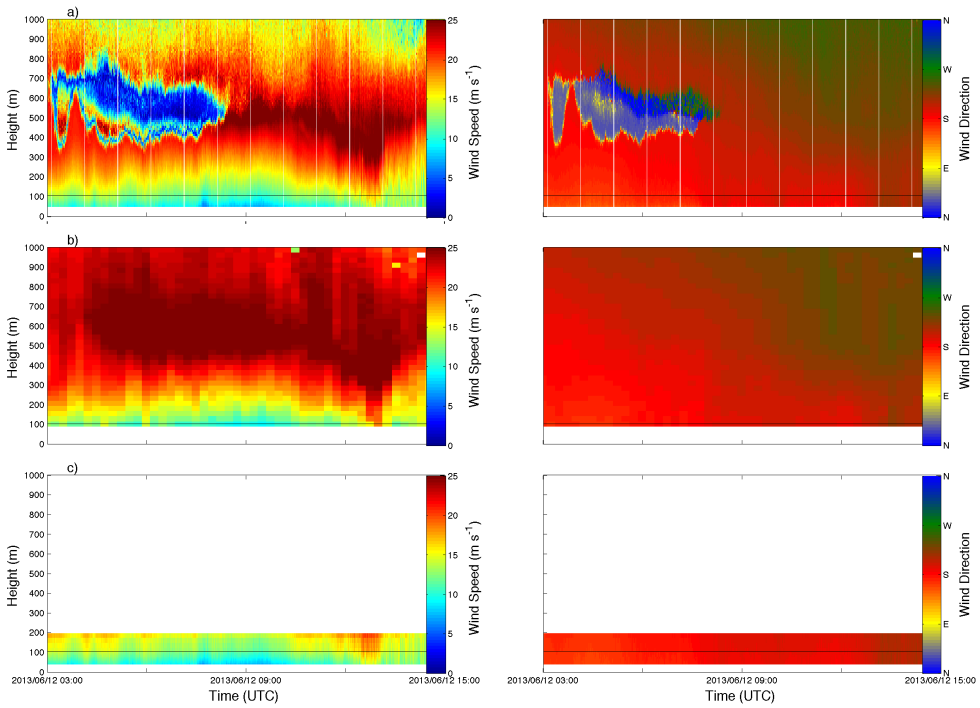

Figure 5.1: Time-height cross-sections of horizontal wind speed (left panels) and wind direction (right panels) derived from a) OU Halo and Galion dual-Doppler technique b) ARM Halo VAD scans and c) WindCube DBS scans on 12 June 2013. One-min means are shown in a) and c) and 15-min instantaneous values are shown in b). Black horizontal lines denote 105 m tri-Doppler analysis height. (Note that maximum WindCube measurement height is 200 m.) Blue shading in a) corresponds with aliased velocity data.

southerly/southwesterly to northerly (Fig. 5.2). Several wave-like features were evident from 0800 to 1000 UTC in the dual-Doppler cross-section at heights spanning from 200 to 1000 m AGL (Fig. 5.2a) and likely indicate the presence of a gravity wave that is associated with the approaching cold front. These waves are not noticeable in time-height cross-sections from the ARM Halo lidar as a result of the lower vertical and temporal resolution (Fig. 5.2b) and are outside the measurement range of the WindCube lidar (Fig. 5.2c). Nocturnal waves are significant, as they transport heat and momentum throughout the boundary layer and can trigger convection or modulate areas of precipitation (Markowski and Richardson 2010). Interactions between LLJs and gravity waves are complex (e.g., Fritts et al. 2003)

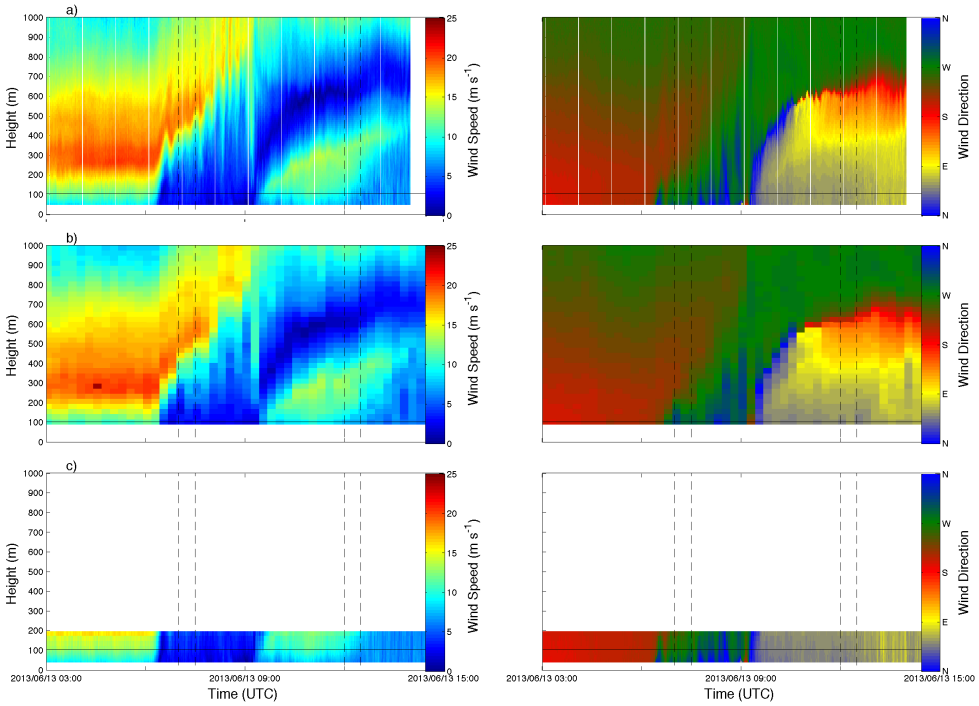

Figure 5.2: As in Fig. 5.1, but for 13 June 2013. Dashed lines indicate averaging periods for profiles shown in Fig. 5.6.

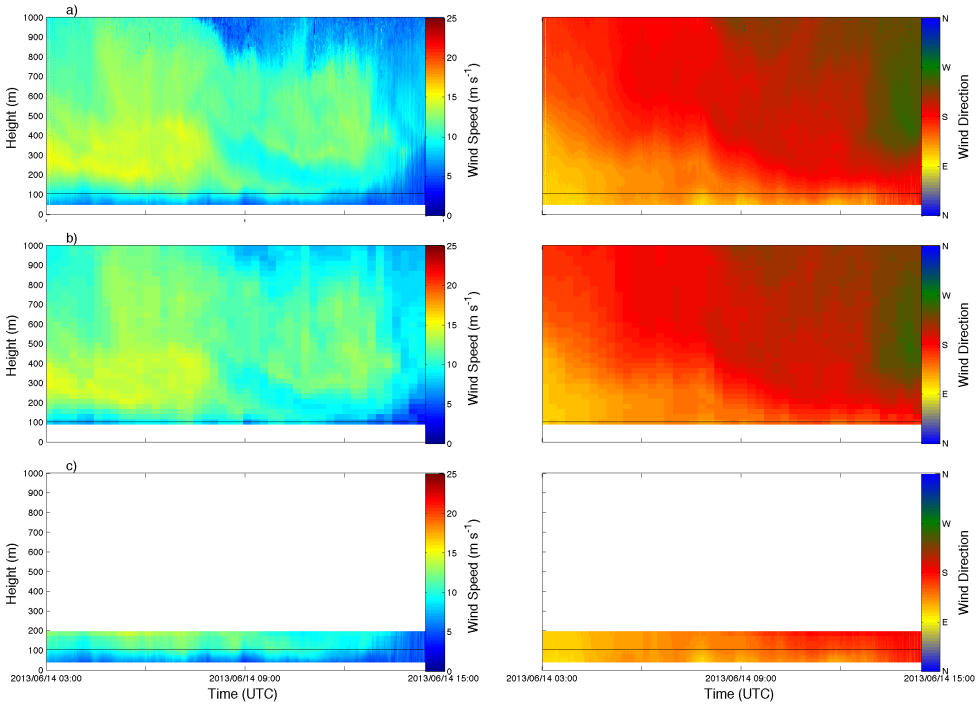

Figure 5.3: As in Fig. 5.1, but for 14 June 2013.

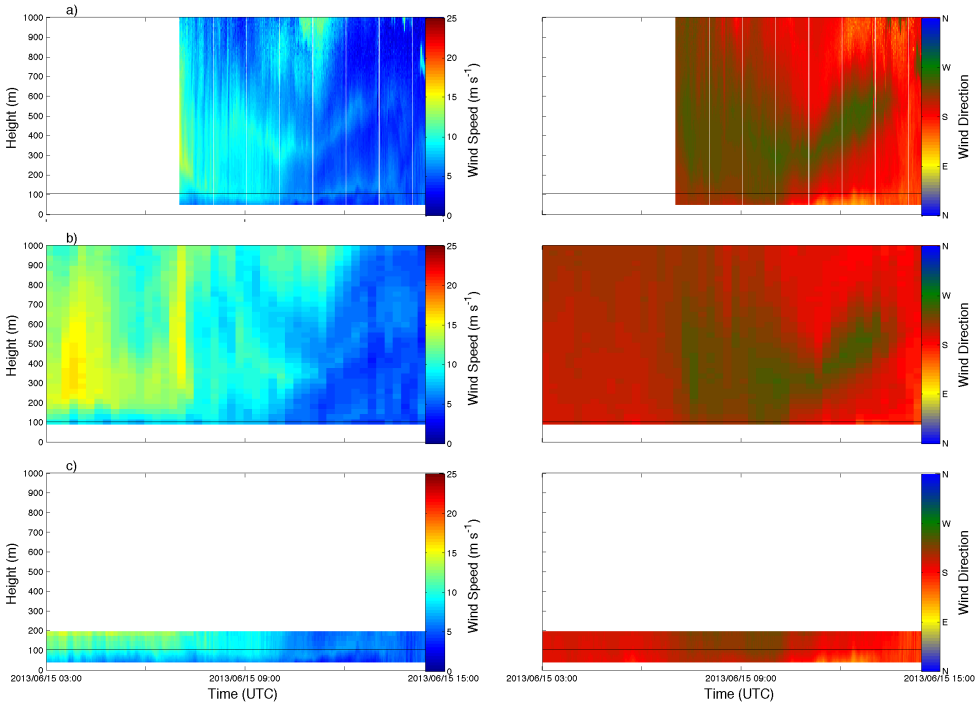

Figure 5.4: As in Fig. 5.1, but for 15 June 2013.

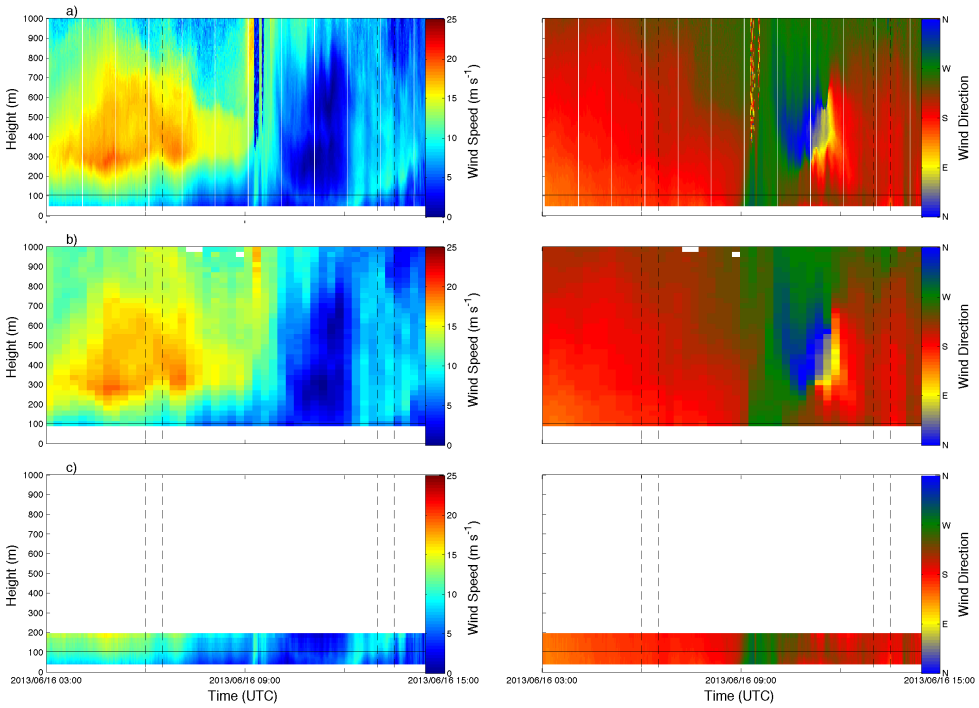

Figure 5.5: As in Fig. 5.1, but for 16 June 2013. Dashed lines indicate averaging periods for profiles shown in Fig. 5.7.

and will likely be a topic of future research with this dataset. A more in-depth analysis of the gravity waves observed during LABLE 2 would require a vertical profile of atmospheric stability and estimation of the Scorer parameter (Scorer 1949), which is outside the scope of this work.

Despite the difference in temporal and vertical resolution in the wind speed and wind direction profiles evident in Figs. 5.1-5.5, profiles of 30-min mean values were quite similar among the different lidars. Examples of 30-min mean profiles of wind speed and wind direction are shown in Figs. 5.6 and 5.7 for time periods during 13 and 16 June 2013, respectively. Even with the presence of wind speed and directional shear, the profiles are quite similar at all heights. (Small differences in the profiles, particularly wind direction, likely resulted from the slight misalignment of the lidars during this week of the experiment and the 15-min time difference between ARM VAD scans.)

Mean wind speeds and wind directions measured at the analysis height of 105 m by the WindCube lidar and the tri-Doppler technique were also in good agreement (Fig. 5.8). The mean wind speeds and wind directions measured by the two different techniques correspond well to one another ($R^2 > 0.98$), despite the fact that the techniques were collecting measurements from different parts of the ARM site, approximately 200 m apart (Fig. 3.4). Thus, horizontal heterogeneity did not appear to be a large factor at the site and was not expected to significantly impact variance values.

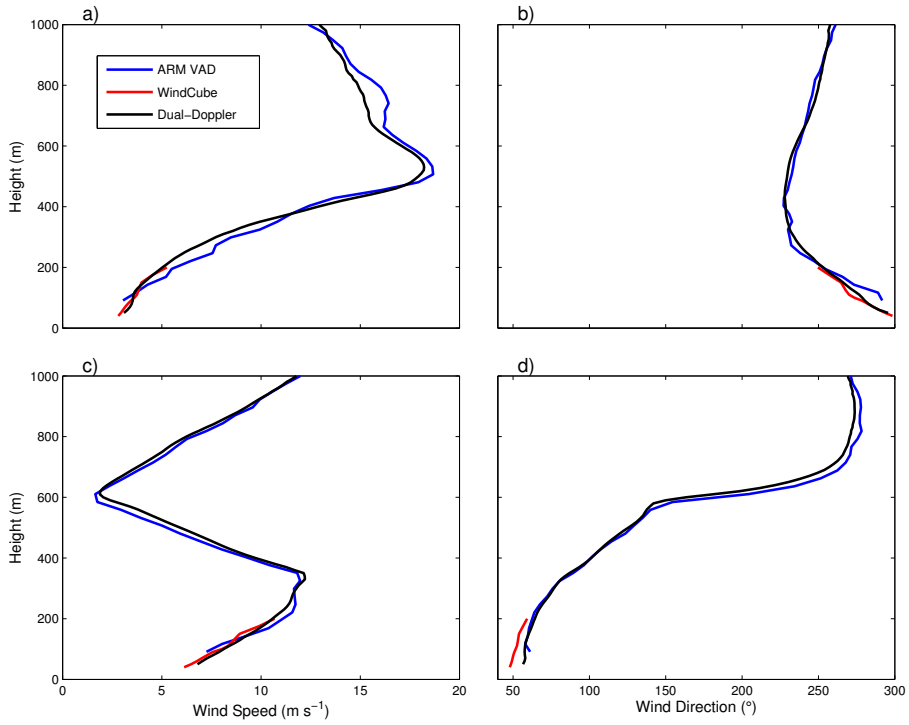

Figure 5.6: 30-min mean wind speed (a, c) and wind direction (b, d) profiles from 0700-0730 UTC (top panels) and 1200-1230 UTC (bottom panels) on 13 June 2013.

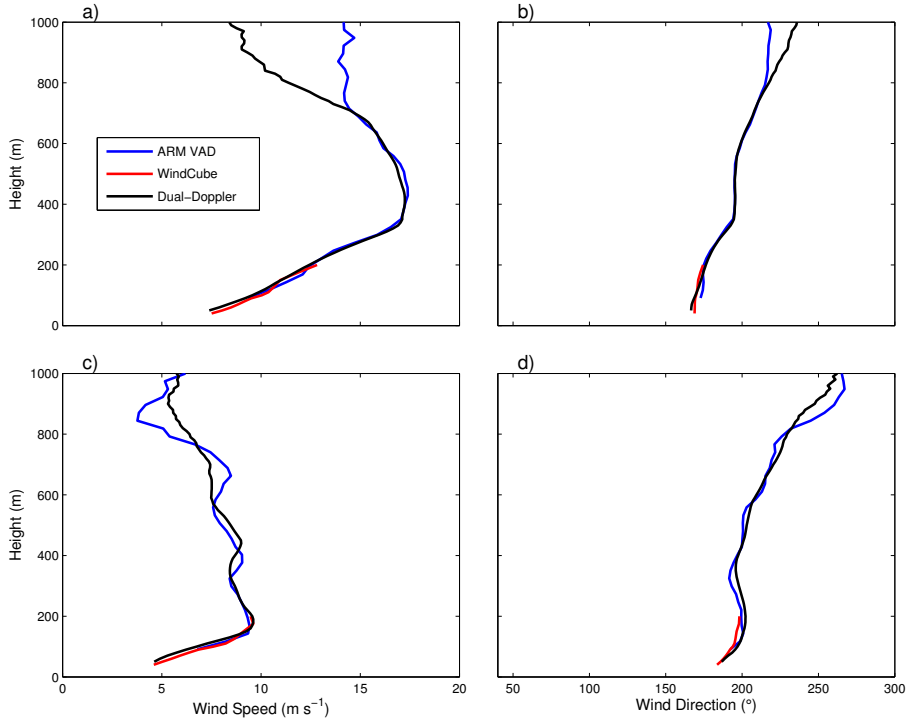

Figure 5.7: 30-min mean wind speed (a, c) and wind direction (b, d) profiles from 0600-0630 UTC (top panels) and 1300-1330 UTC (bottom panels) on 16 June 2013.

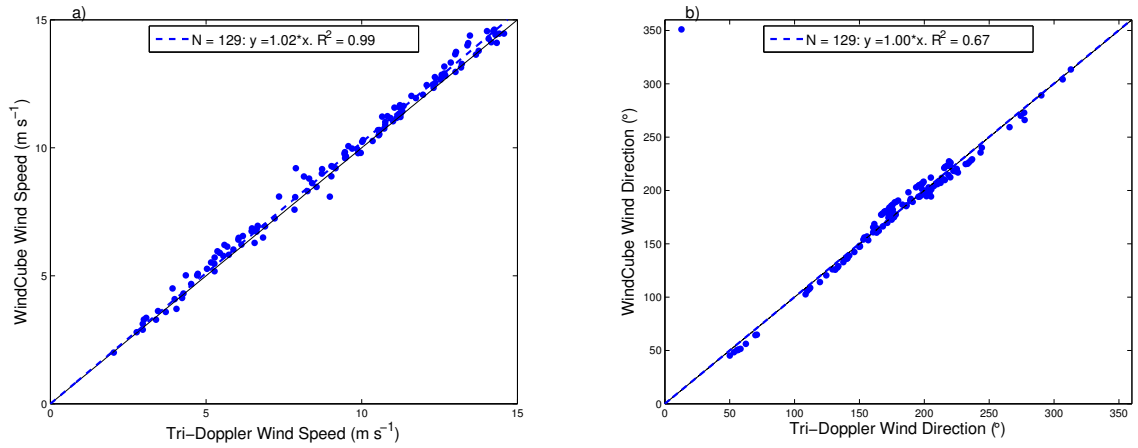

Figure 5.8: Scatter plots of 30-min mean a) wind speed and b) wind direction from WindCube lidar and tri-Doppler technique at 105 m AGL. One-to-one line is shown in black for reference and regression fits are indicated by blue dashed lines. In b), wind direction values that were less than 15° were added to 360° to avoid biasing the regression line for wind directions near northerly.

Scatter plots of the 30-min variance values measured by the different techniques at 105 m are shown in Fig. 5.9. Variance was stratified by atmospheric stability according to Obukhov length, as discussed in Sect. 4.5. For the u variance component, the variance associated with all stability conditions was quite similar for both the tri-Doppler technique and the WindCube lidar, with most points lying close to the one-to-one line. However, there was a tendency for the tri-Doppler technique to measure higher crosswise variances under stable conditions and lower crosswise variances under unstable conditions in comparison to the WindCube lidar (Fig. 5.9b). The WindCube's overestimation of the v variance under unstable conditions is likely related to variance contamination, which is most prevalent during unstable periods (Sathe et al. 2011). This overestimation of variance under unstable conditions is further discussed in Ch. 6.

The tri-Doppler technique measured higher v variance values than the WindCube lidar under stable conditions, although v variance values were comparable

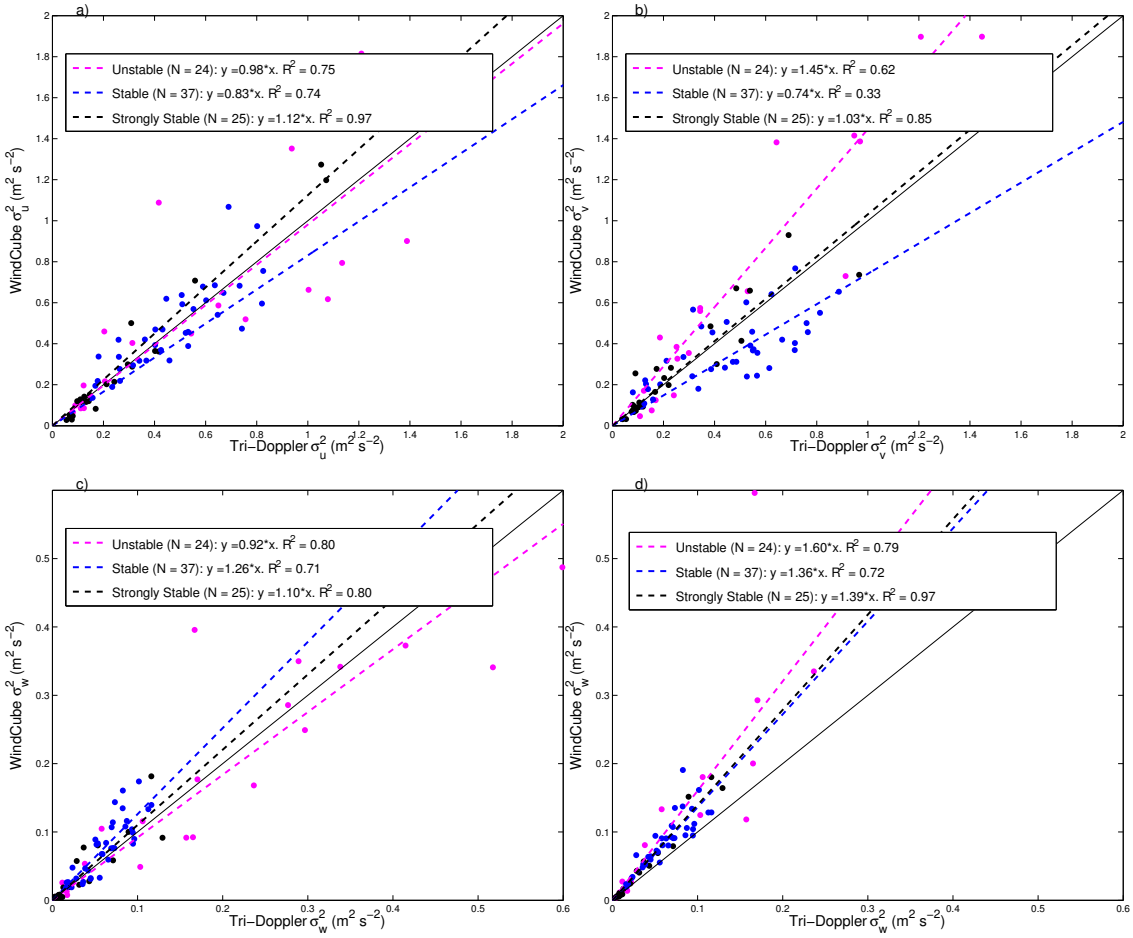

Figure 5.9: Scatter plots of 30-min tri-Doppler variance versus WindCube variance at 105 m AGL stratified by stability (circles) and regression lines for different stability classes (dashed lines). In all figures, one-to-one line is shown in black for reference. Scatter plots for a) u variance, b) v variance and c) and d) w variance are shown. Data from neutral stability cases are not shown due to the small amount of data points in this stability classification. In c), w variance from WindCube lidar is estimated from DBS technique and in d) it is estimated directly from the vertical beam position.

under strongly stable conditions (Fig. 5.9b). One would expect the tri-Doppler technique to measure increasingly higher variance values than the WindCube lidar as stability increases and turbulence scales decrease, since the tri-Doppler technique is not averaging turbulent scales over a scanning circle. However, this is not the case for the collected dataset. There are two main caveats that may have led

to this discrepancy: 1) The 4-m Obukhov length was used as a stability parameter, as this was the only sonic anemometer dataset available during the tri-Doppler portion of the experiment and a temperature and wind profile was not available to calculate *Ri*. The stability classification between weakly stable and strongly stable conditions at 4 m may not be applicable to measurements at 105 m AGL, particularly since 105 m is likely above the surface layer under stable conditions (Arya 2001). In addition, the Obukhov length may not be an entirely reliable parameter under stable conditions, as intermittent turbulence in the stable boundary layer can induce large errors in flux calculations, since the fluxes themselves are very small (Mahrt 1985). 2) The same variance estimation techniques were applied to all stability classes, although it is recommended that different techniques are used to quantify turbulence in strongly stable conditions (e.g., Howell and Sun 1999).

The majority of the periods where the tri-Doppler crosswise variance was much larger than the WindCube variance occurred on 12 and 16 June, when the 4-m Obukhov length indicated weak stability and a strong LLJ was present during the overnight hours (Figs. 5.1, 5.5). Thus, there appears to be a link between weak stability, the presence of a strong LLJ, and the measurement of higher crosswise variance by the tri-Doppler technique. Strong LLJs tend to be associated with weak stability at the ARM site (Bonin et al. 2015), and the effects of these LLJs on variance measurements are briefly discussed later in the section.

As previously discussed, the vertical variance can be estimated from the WindCube lidar in two ways: through the use of the DBS equations or by using data

from the vertically pointed beam position. Vertical variance measured using the DBS technique with the WindCube lidar is quite similar to variance measured by the tri-Doppler technique (Fig. 5.9c). However, the WindCube lidar nearly always measured higher *w* variance values than the tri-Doppler technique when the vertically pointed beam was used to estimate the variance (Fig. 5.9d). Since the latter approximation of vertical variance does not require the use of a scanning circle, the main differences between the WindCube and the tri-Doppler estimations of variance in Fig. 5.9d are the temporal resolution of the scans and the size of the probe volume. The WindCube beam only points vertically every 4 s (compared to the tri-Doppler technique, which collects data from the vertically pointed beam every 1 s), which would serve to decrease the variance estimated by the WindCube lidar in comparison to the variance estimated from the tri-Doppler technique. However, the WindCube's probe volume length is 20 m, while the probe volume length of the scanning lidars was set to 30 m, which would serve to increase the WindCube-estimated variance in comparison to the tri-Doppler variance. Since the WindCube estimates of vertical variance were nearly always larger than the tri-Doppler estimates, the difference in *w* variance when the WindCube used the vertical beam appear to be largely affected by volume averaging. It is likely that the estimates of *u* and *v* variance were also affected by the difference in probe volume between the WindCube lidar and the scanning lidars, as the WindCube's smaller probe volume allows for the measurement of smaller scales of turbulence.

In order to examine the scales of turbulence measured by the two different techniques, average velocity spectra were calculated for each scanning technique. First, the raw velocity data were separated into 30-min blocks. Missing values were filled in using linear regression. The 30-min mean was removed and a Fourier transform was performed on the velocity deviations. Spectra were normalized using the friction velocity, u_*, and the similarity function for the dissipation rate, ϕ_ε, according to the surface-layer scaling described in Kaimal and Finnigan (1994) and discussed in Sect. 2.1.2.3. The friction velocity was estimated from the 4-m sonic anemometer data and ϕ_ε was estimated from the following relations, which are based on data collected by Kaimal et al. (1972):

$$\phi_\varepsilon^{2/3} = \left\{ \begin{array}{ll} 1+0.5\,|z/L|^{2/3}, & z/L \leq 0 \\ (1+5z/L)^{2/3}, & z/L \geq 0 \end{array} \right\}. \tag{5.1}$$

Frequency for the spectra were normalized by the height of the measurements, z, and the mean velocity, $\overline{u}$, where a different value of $\overline{u}$ was determined for each stability condition. Finally, all 30-min spectra for each stability class were averaged to produce average spectra.

Averaged spectra for strongly stable, stable, and unstable conditions are shown in Fig. 5.10. The large dip in the WindCube spectra that occurs at approximately 0.25 Hz corresponds to the time it takes the WindCube lidar to complete a full scan (approximately four seconds). Every four seconds, the WindCube observations of u and v become completely independent again, so the variance for the four-second time period is greatly reduced. This frequency cut-off is indicated with a

dashed line in Fig. 5.10, and WindCube spectral energy to the right of this line is inaccurate. However, since the WindCube velocity algorithm updates the velocity vector every 1 s, there is still spectral energy shown for frequencies above 0.25 Hz. The large dip in the *u* and *v* spectra is not observed in the *w* spectra, as only data from the WindCube's vertical beam were used to calculate the spectra, and thus only independent data were used. However, the WindCube *w* spectra cut off at the Nyquist frequency of 0.125 Hz as a result of the 4-s temporal resolution of the vertical beam data.

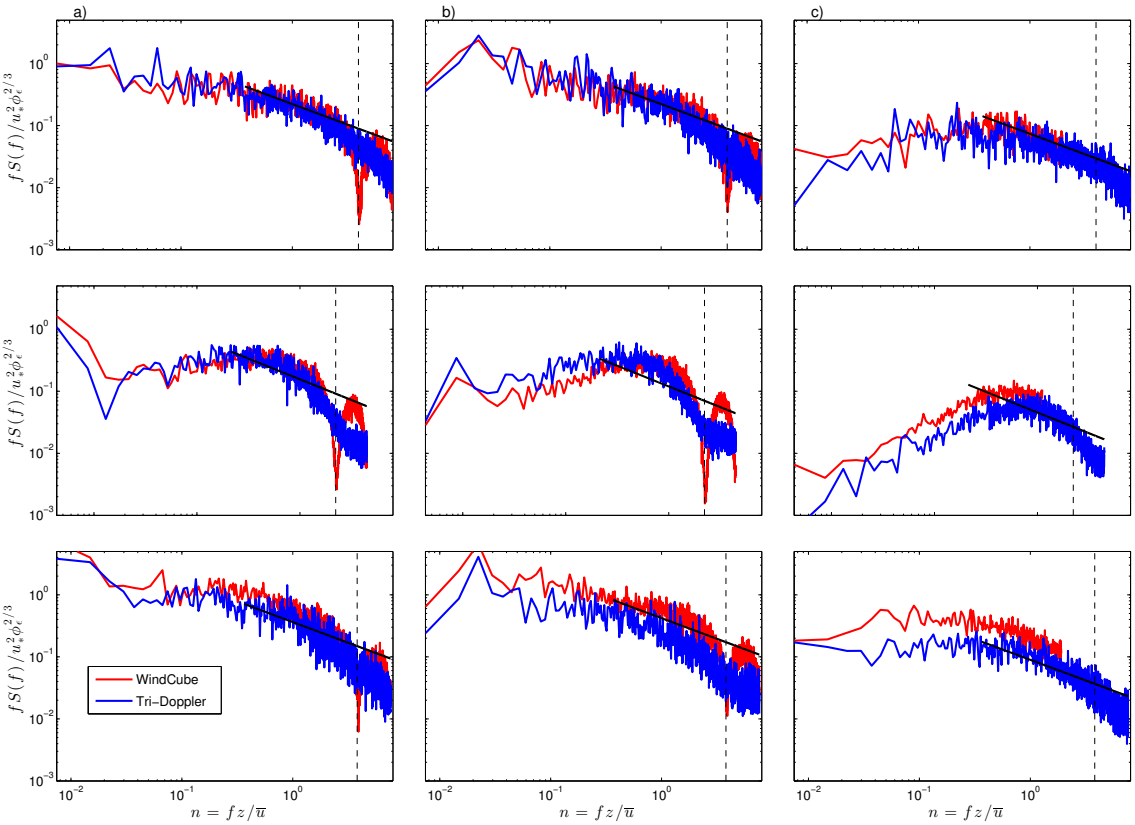

Figure 5.10: Normalized average a) *u* velocity b) *v* velocity and c) *w* velocity spectra from tri-Doppler technique and WindCube lidar at 105 m AGL from 12 to 16 June 2013. Spectra from strongly stable (top), stable (middle), and unstable (bottom) atmospheric conditions are shown. Black solid line indicates -2/3 slope (inertial subrange). Vertical black dashed line indicates 0.25 Hz WindCube frequency cut-off. In c), WindCube spectra were calculated using only data from the vertical beam.

The WindCube and tri-Doppler u and v spectra under strongly stable conditions agree quite well up until just before 0.25 Hz, when the WindCube spectra drop off rapidly due to the 4-s scan time. In contrast, under stable conditions, the tri-Doppler v spectra show higher spectral energy than the WindCube spectra up until approximately $n = 0.4$. This higher spectral energy is reflected in the larger v variance values that were often measured by the tri-Doppler technique under stable conditions (Fig. 5.9b). It is possible that the waves that were evident during several nights of the experiment (Figs. 5.1-5.5), which would be associated with large spatial scales, are responsible for the increased spectral energy in the tri-Doppler v spectra at low frequencies (middle panel in Fig. 5.10b) and higher crosswise variance values (Fig. 5.9b) under stable conditions. However, further research is needed to determine the spectral characteristics of these waves and their influence on the turbulence field and the results from the stable spectra shown here are not entirely clear.

Under unstable conditions, the WindCube u and v spectra have slightly higher energy than the tri-Doppler spectra for frequencies before the cut-off at 0.25 Hz (bottom panels in Fig. 5.10). Cañadillas et al. (2011) found similar results when comparing averaged WindCube spectra to sonic anemometer spectra and attribute the increase in spectral energy to variance contamination. Indeed, Cañadillas et al. (2011) showed that this energy increase was not present when the spectra were calculated with the radial velocity rather than the u and v velocities from the DBS technique. In summary, the differing shapes of the WindCube u and v spectra in

comparison to the tri-Doppler spectra can be largely attributed to two effects: the 4-s scan time, which causes the dip in the spectra at 0.25 Hz and the combination of data from different beam positions, which causes variance contamination and an increase in the spectral energy that is particularly noticeable under unstable conditions.

For all three stability classes, the WindCube *w* spectra show higher spectral energy than the tri-Doppler spectra for nearly all frequencies (Fig. 5.10c). Since the raw *w* wind speed was measured in the same way by both the WindCube lidar and the tri-Doppler technique, the difference in the *w* spectra is largely due to the difference in probe volume between the lidars. Although the WindCube lidar only obtains a direct measurement of the *w* component every 4 s and thus cannot measure turbulent fluctuations with frequencies higher than 0.125 Hz, the resultant *w* variance values measured by the WindCube's vertical beam are nearly always higher than those measured by the tri-Doppler technique (Fig. 5.9d). This suggests that the probe volume size has a larger effect on the measurement of vertical variance than the temporal resolution of the measurements, although it is difficult to assess the impact of other factors, such as instrument noise and sensitivity.

In summary, the tri-Doppler technique can be used to measure mean wind speed profiles (Figs. 5.6, 5.7), sample small-scale features in the horizontal wind speed profile (Figs. 5.1-5.5) and measure high-frequency turbulence at the height where the lidar beams intersect (Fig. 5.9). At an operational wind farm, three scanning lidars could be pointed at a height corresponding to turbine hub height

to collect high-frequency turbulence data while simultaneously measuring a mean horizontal wind speed and wind direction profile that spans across heights corresponding to the turbine rotor disk.

For this dataset, the tri-Doppler technique tended to measure higher crosswise variance values than the WindCube lidar under stable conditions, possibly due to the presence of atmospheric waves. This appeared to be the main advantage of using a tri-Doppler technique over a standard DBS or VAD technique. However, a more in-depth study should be conducted that compares tri-Doppler measurements to measurements from an identical scanning lidar using a standard DBS or VAD technique under a variety of other stability conditions. For example, the largest discrepancies between WindCube variance and variance measured by sonic anemometers on a tower in Boulder, Colorado occurred under unstable conditions, and this appears to be one of the sets of conditions under which significant improvements must be made for lidar scanning strategies, as will be discussed in Sect. 6.2.1. Unfortunately, our study at the ARM site did not include a substantial amount of tri-Doppler data under unstable conditions, as the lidars used a different scanning strategy during the daytime hours, so it is difficult to determine if improvements can be made over the WindCube DBS technique under unstable conditions by using a tri-Doppler scanning technique.

5.2.2 Virtual tower technique

The virtual tower technique was evaluated at the ARM site from 28 June to 3 July. Although the use of a virtual tower allows for the measurement of turbulence at multiple heights, unlike the tri-Doppler technique, these turbulence measurements are spaced apart in time and will not capture the full temporal evolution of the turbulence profile.

Ideally, the beams of the scanning lidars would be rapidly moved from one height to another so that velocity measurements with high temporal resolution could be obtained at all measurement heights. However, although the scanning lidars only collect measurements for one second, it takes several additional seconds to move the lidar beam to a different position and begin collecting measurements again. Thus, a 10-min stare period was selected for each height to ensure that all three scanning lidars had time to adjust to the new measurement height and start collecting measurements. Additionally, although each full virtual tower scan took 60 min, the software installed on all three of the scanning lidars did not restart each scan immediately and instead calculated an approximate scan time for a complete virtual tower scan and waited until this full time had elapsed before restarting the scan. Thus, measurements at each height were actually taken approximately 1.75 hours apart. It is likely that this issue with the scanning software will not be present in later versions, leading to faster virtual tower scan times.

In order to investigate the usefulness of the virtual tower turbulence measurements, turbulence measured from the virtual tower technique was compared to

10-min variance values measured by the WindCube lidar for each hour. (Unfortunately, there were issues with the 60-m sonic data stream during this week of the experiment, so only sonic data from 4 and 25 m are shown to help depict the full variance profile.) A sample time series of the 10-min variance measured by the WindCube lidar at 100 m AGL is shown in Fig. 5.11. (In this section, the 10-min, rather than the 30-min variance is investigated, as the virtual tower technique only involved scanning at each height for 10 min.) Two hour-long time periods were selected for further analysis: 0800 to 0900 UTC, which occurred under strongly stable conditions, and 1700 to 1800 UTC, which occurred under unstable conditions. These time periods are highlighted in Fig. 5.11 and indicate the vastly different magnitudes of variance measured by the WindCube lidar under different stability conditions.

Variance and wind speed profiles measured by the various techniques from 0800 to 0900 UTC on 3 July 2013 (3:00 to 4:00 am local time) are shown in Fig. 5.12. Not surprisingly, velocity variances measured during this stable period were quite small, with u and v variances on the order of 0.1 $m^2\ s^{-2}$ and w variances on the order of 0.01 $m^2\ s^{-2}$. Profiles measured by the WindCube lidar show the variance decreasing to a height of approximately 100 m before remaining relatively constant with height, then increasing from 120 to 200 m (Figs. 5.12a–c). The mean wind speed increases from 4 to 100 m before decreasing slightly, which could indicate an LLJ nose at 100 m (Fig. 5.12d). These profiles are similar to

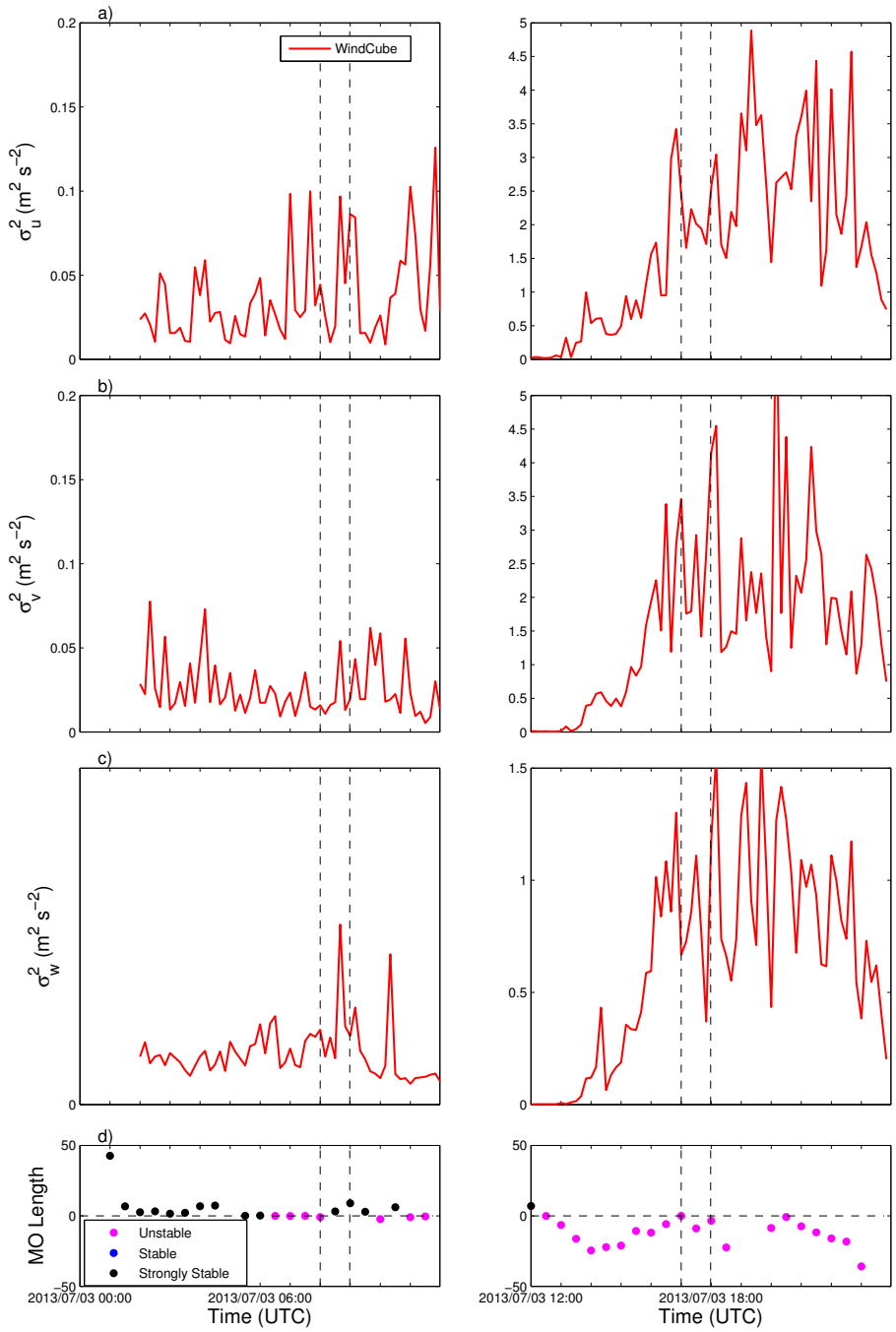

Figure 5.11: Time series of 10-min a) *u* b) *v* and c) *w* variance from WindCube lidar at 100 m AGL and d) Monin-Obukhov length from 4-m sonic anemometer on 3 July 2013. Left panels show data from 0000 to 1200 UTC and right panels show data from 1200 to 2359 UTC (time series was split into two panels to better depict variance of different magnitudes). Vertical dashed lines in each figure enclose hour-long periods discussed later in the text. Vertical variance values shown in c) are derived from WindCube vertical beam.

the composite LLJ profiles presented by Banta et al. (2006), where the approximate minimum in the WindCube-measured variance is located at the height of the

wind speed maximum. This variance profile occurs because shear-induced turbulence is maximized near the ground and minimized at the height of the wind speed maximum, where the vertical wind shear goes to zero. Large values of turbulence above the wind speed maximum may have been associated with waves, as large-scale fluctuations were noted in the WindCube vertical velocity time series (not shown).

Variance values measured by the virtual tower technique and the WindCube DBS technique were quite similar at 60 and 100 m AGL, with little variation indicated in the 10-min WindCube variance values throughout the hour-long period (Figs. 5.12a–c). The horizontal variance values measured by the WindCube lidar were larger than those measured by the virtual tower technique at 200 m, possibly because 200 m is the maximum measurement height of the WindCube lidar, and the SNR of WindCube measurements is typically maximized at approximately 100 m AGL. Thus, lower SNR values at 200 m AGL would indicate large amounts of noise in the radial velocity values measured by the WindCube lidar, which would artificially increase the variance. Although the WindCube data were filtered by SNR and passed through a spike filter, the 200-m WindCube radial velocity data did often appear noisy (not shown). In general, however, the variance values measured by the virtual tower technique were similar to those measured by the WindCube lidar and were nearly always located within one standard deviation of the mean 10-min variance value measured by the WindCube lidar during the hour-long period. This indicates that the virtual tower variance measurements,

which were collected approximately once per hour at each measurement height, are indicative of the variance experienced throughout the hour-long time period under stable conditions. Mean wind speed profiles measured by the virtual tower technique were very close to those measured by the WindCube lidar (Fig. 5.12d).

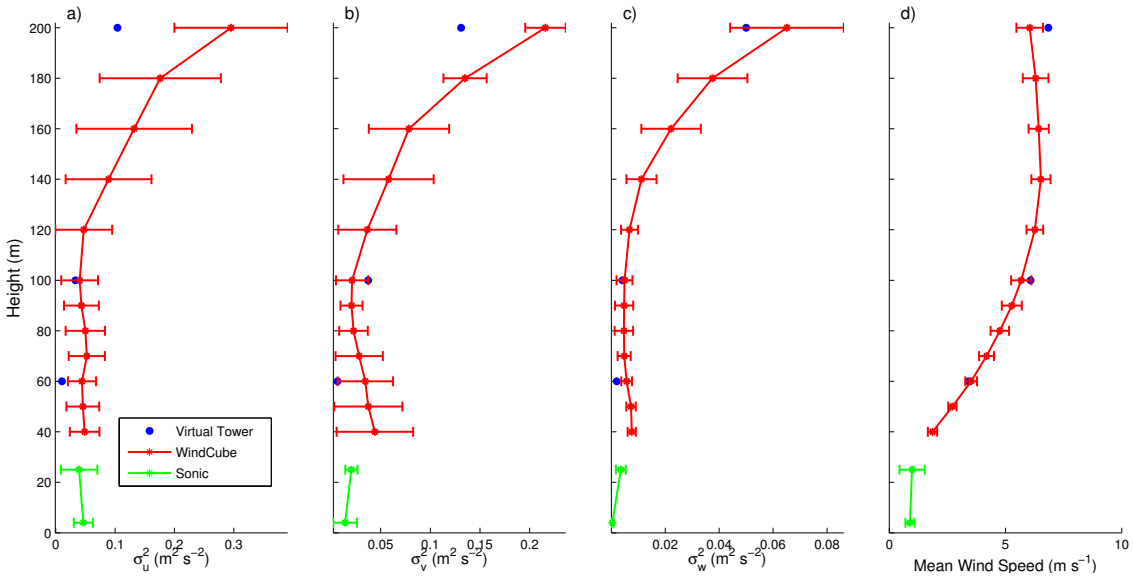

Figure 5.12: Profiles of a) *u* b) *v* and c) *w* variance and d) mean wind speed measured by virtual tower technique, WindCube lidar, and sonic anemometers at the ARM site on 3 July 2013 from 0800 to 0900 UTC. Tri-Doppler markers show variance and mean wind speed calculated from the 10-min subsets of velocity data collected at each height, while WindCube and sonic anemometer circles and error bars indicate the mean and standard deviation of the 10-min variance values and mean wind speeds measured throughout the hour-long time period.

A similar profile is shown in Fig. 5.13 for 1700 to 1800 UTC on 3 July 2013 (12:00 to 1:00 pm local time), which corresponded to unstable atmospheric conditions. Variance values measured during this time period were much larger than those measured during the stable period in Fig. 5.12. In addition, the 10-min variance values changed fairly significantly over the course of the hour as the convective boundary layer developed (Figs. 5.11, 5.13). However, the mean variance profile did not change significantly with height, which is to be expected in the

surface layer or "constant flux layer" according to similarity theory (e.g., Arya 2001). The wind speed profile is also uniform, in accordance with a well-mixed convective boundary layer (Fig. 5.13d).

During this period, the WindCube lidar nearly always measured larger horizontal variance values than the virtual tower technique. The larger u and v variance estimates are likely related to variance contamination, as discussed in Sathe et al. (2011) and in Sect. 6.2.1. During the LATTE campaign, as will be discussed in Ch. 6, the WindCube v2 lidar measured u and v variance values that were often over twice as large as those measured by sonic anemometers on the BAO tower under unstable conditions, with the overestimation due in part to the contamination of the u and v velocity components associated with spatial heterogeneity in the w component across the lidar scanning circle (Sect. 6.2.1). It is difficult to determine how much variance contamination occurred at the ARM site, as the 60-m sonic anemometer had data quality issues for the majority of the experiment and the 25-m sonic anemometer did not correspond with any lidar measurement heights. Both the sonic anemometer and the WindCube lidar measured a large variation in 10-min variance values throughout this hour-long time period, which was not captured by the virtual tower technique, as the virtual tower technique involves moving the lidars to a different measurement height every 10 min.

Although it is difficult to assess the accuracy of the virtual tower technique without corresponding sonic anemometer measurements at several heights, the virtual tower technique compared favorably to WindCube lidar measurements at 60

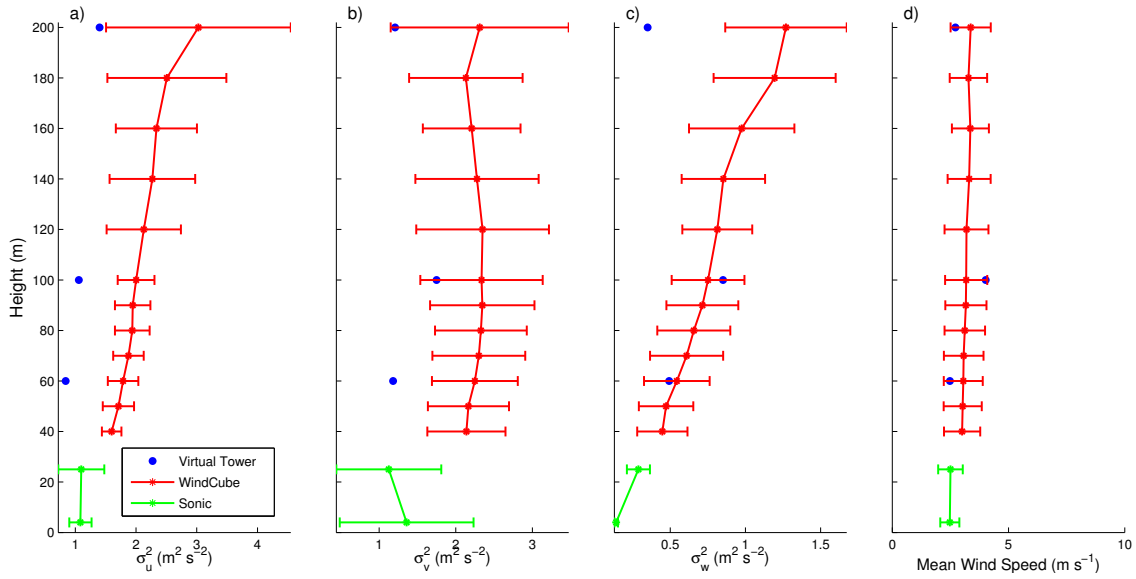

Figure 5.13: As in Fig. 5.12, but for 1700 to 1800 UTC.

and 100 m under stable conditions. When the atmosphere was stable at the ARM site, the 10-min variance values did not change significantly throughout the hour-long time period it took the scanning lidars to complete a full virtual tower scan. Thus, by taking measurements for 10 min at each height, the virtual tower technique was able to accurately depict the turbulence profiles measured throughout the hour. However, the virtual tower scans missed a significant amount of variability in the variance profiles during unstable conditions. In the case shown here, the variation in the variance profiles was due to the developing convective boundary layer, but changes in variance profiles could also occur as the result of a ramp event or approaching frontal boundary, which would have a significant impact on power production at a wind farm. Thus, the virtual tower technique as evaluated at the ARM site does not appear to be an accurate method for measuring variance profiles under unstable conditions. If the scan time were reduced significantly, either by removing measurement heights or by scanning for shorter time periods at

each height, greater variability in the variance profiles could be captured. Future work could examine the length of time needed to collect velocity measurements at a particular measurement height in order to obtain accurate variance estimates.

5.3 Summary and conclusions

In this chapter, two different multi-lidar scanning strategies, the tri-Doppler technique and the virtual tower technique, were evaluated for their ability to measure mean wind profiles and turbulence in the lower boundary layer. These scanning strategies attempt to mitigate the systematic errors induced by DBS and VAD scans, techniques utilized by vertically-profiling lidars, for example, including averaging over a scanning circle and contamination caused by cross-components of the Reynolds stress tensor. Wind speeds and turbulence measured by these techniques were compared to similar measurements made by a commercially available WindCube lidar that uses a DBS technique.

The tri-Doppler technique involved pointing three scanning lidars at the same point in space and solving a set of equations to calculate u, v, and w every one second. Because the velocity data were not averaged over a scanning circle, the tri-Doppler technique measured higher values of crosswise variance under stable conditions in comparison to the WindCube lidar, which used a DBS technique. However, this appeared to be the main advantage to using the tri-Doppler technique to measure turbulence. The WindCube lidar produced larger estimates of

the crosswise variance under unstable conditions, likely due to variance contamination. Thus, it is possible that the tri-Doppler technique can provide more accurate crosswise variance estimates under unstable conditions as well, although it is difficult to make this assessment without the availability of in-situ point measurements from a sonic anemometer.

With the tri-Doppler technique, turbulence information was only available at the single height where the lidars were pointed. However, velocity data collected at other points along the two horizontal lidar beams can still be used to calculate the average wind speed profile. On an operational wind farm, this strategy could be designed to collect high-frequency turbulence measurements at the turbine hub height and collect average wind speed measurements at other heights across the rotor-disk area. It is likely that using three scanning lidars for a scanning strategy is mainly only feasible in a research setting, but a single scanning lidar could be pointed into the mean wind direction to measure line-of-sight turbulence and wind speed.

In order to take turbulence measurements at multiple heights, a virtual tower technique was also implemented at the ARM site. The three scanning lidars pointed at several measurement heights directly above the WindCube lidar to estimate a variance profile. The lidars were pointed at each measurement height for 10 min and a full scan took approximately 60 min, such that only 10 min of observations were available each hour at each height for the calculation of variance. Under stable conditions, when variance was small and did not vary significantly

with time, the virtual tower technique measured similar variance profiles to the WindCube lidar. However, under unstable conditions, the variance values changed significantly over the course of an hour and the virtual tower variance profiles did not fully represent the variance values experienced throughout the hour. Thus, the virtual tower technique appears to be most well-suited for measuring turbulence profiles under stable conditions, although full verification with a sonic anemometer profile is still needed.

With current lidar technology and scanning software, two main multi-lidar scanning techniques are available for the measurement of turbulence: the tri-Doppler technique, where 3-D high-frequency data can be collected constantly at one height, or the virtual tower technique, where short time periods of 3-D data can be collected at multiple heights. While the tri-Doppler technique optimizes temporal resolution and the virtual tower technique optimizes spatial resolution, neither of these techniques is ideal for the measurement of turbulence, as turbulence values can vary significantly in both time and space. However, more research is needed to determine which atmospheric measurements are most important for wind energy applications. Results from a recent power curve modeling study demonstrated that the measurement of mean wind speeds across the turbine rotor disk improved power prediction, while the measurement of wind speed standard deviations across the entire rotor disk by a WindCube lidar did not provide significant improvements in power prediction over just using the hub-height value

(Bulaevskaya et al. 2015). These results were only presented for one unwaked turbine in complex terrain in California, although a similar study is currently being conducted at a wind farm in flat terrain. The results suggest that the tri-Doppler technique, which only measures turbulence at one height, could provide sufficient inflow data for turbine power prediction and for a deeper understanding of reasons for turbine underperformance. The tri-Doppler technique allows for a constant estimation of turbulence parameters at one height as well as estimation of mean wind speeds at several heights spanning a typical turbine rotor disk. In addition to turbine inflow conditions, the tri-Doppler technique could be used to study turbine wakes, as the technique does not require the assumption of horizontal flow homogeneity across a scanning circle.

In general, the tri-Doppler technique is much easier to implement than a virtual tower technique, as it does not require the exact temporal synchronization of scan angles from multiple lidars. Research on the performance of the tri-Doppler technique at a site with multiple sonic anemometers is currently ongoing (Fuertes et al. 2014) and should be supplemented by further research on the performance of the technique under different stability conditions and at sites in both flat and complex terrain.

Chapter 6

Single-lidar techniques

6.1 Introduction

Three main research questions are addressed in this chapter: 1) How well do the two most commonly used scanning strategies (the DBS and VAD techniques) measure turbulence under different stability conditions? 2) How well does the new six-beam technique measure turbulence under different stability conditions? and 3) How do the temporal resolution for all three techniques affect the accuracy of measured turbulence? To address these questions, turbulence measured with the various lidar techniques is compared to turbulence measured by 3-D sonic anemometers on tall towers at sites in Oklahoma and Colorado during LABLE 2 and LATTE. Turbulence measurement errors that occur as a result of the lidar temporal resolution are evaluated using information from the sonic anemometer data and recommendations are made for the operational use of the different scanning strategies.

The DBS and six-beam strategies were evaluated at the ARM site during LABLE 2, while all three scanning strategies were evaluated during LATTE. As the BAO featured a large amount of 3-D sonic anemometer verification data, this

site will be primarily used to draw conclusions about the accuracy of lidar turbulence measurements. These results will be corroborated by data collected during LABLE 2.

To the author's knowledge, this work represents the first time the six-beam technique has been experimentally validated with high-frequency sonic anemometers and commercially available lidars. The use of commercially available lidars allows for an evaluation of turbulence measured with lidar technologies and scanning strategies that are commonly employed in the wind energy industry. Results from this research provide valuable information for refinement of the six-beam technique and for future avenues of research for lidar turbulence scanning strategies.

6.2 Scanning strategy evaluation

In this section, all three scanning strategies will be evaluated in comparison to the available 3-D sonic measurements at each site.

6.2.1 Comparison of turbulence parameters: LATTE

Figure 6.1 demonstrates the typical diurnal cycle of turbulence (σ_u^2, σ_v^2, and σ_w^2) at the BAO, with low values of turbulence occurring during the evening and overnight hours (approximately 0000–1200 UTC) and high values of turbulence occurring during daytime, convective conditions (approximately 1200–0000 UTC). (Note that for all LATTE plots, data from the NCAR sonics are shown, unless the mean

wind direction corresponded to the NCAR sonic wake sector, in which case the OU sonics were used. Local time is UTC-7.) During this period, the wind direction generally shifted between easterly/southeasterly and northerly (Fig. 6.1e). However, from the late night hours of 23 March into the early morning hours of 24 March, winds were primarily from the west/northwest, which is the direction of the Rocky Mountains. Flow from the mountains was associated with higher mean wind speeds and variances of the u and v velocity components in comparison to the rest of the period (Fig. 6.1). Thus, variance values measured when the mean wind direction was between 225 and 315° were excluded from scatter plots and statistical analyses shown later in this chapter, as discussed in Sect. 3.2.

The following sections will focus on measurements from 25 March 2014, which was a calm, clear day with no precipitation when all three lidars had good data availability. Variance estimates from each lidar and scanning strategy will be compared to similar measurements made by the sonic anemometers and the other lidars. For most comparison plots, variance estimates from the measurement height where the lidar data availability was greatest are shown. For the WindCube and ZephIR lidars, which only take measurements up to 200 m AGL, data from 100 m AGL are shown. For the Halo lidar, which has a minimum range gate of 105 m, data from 200 m AGL are shown.

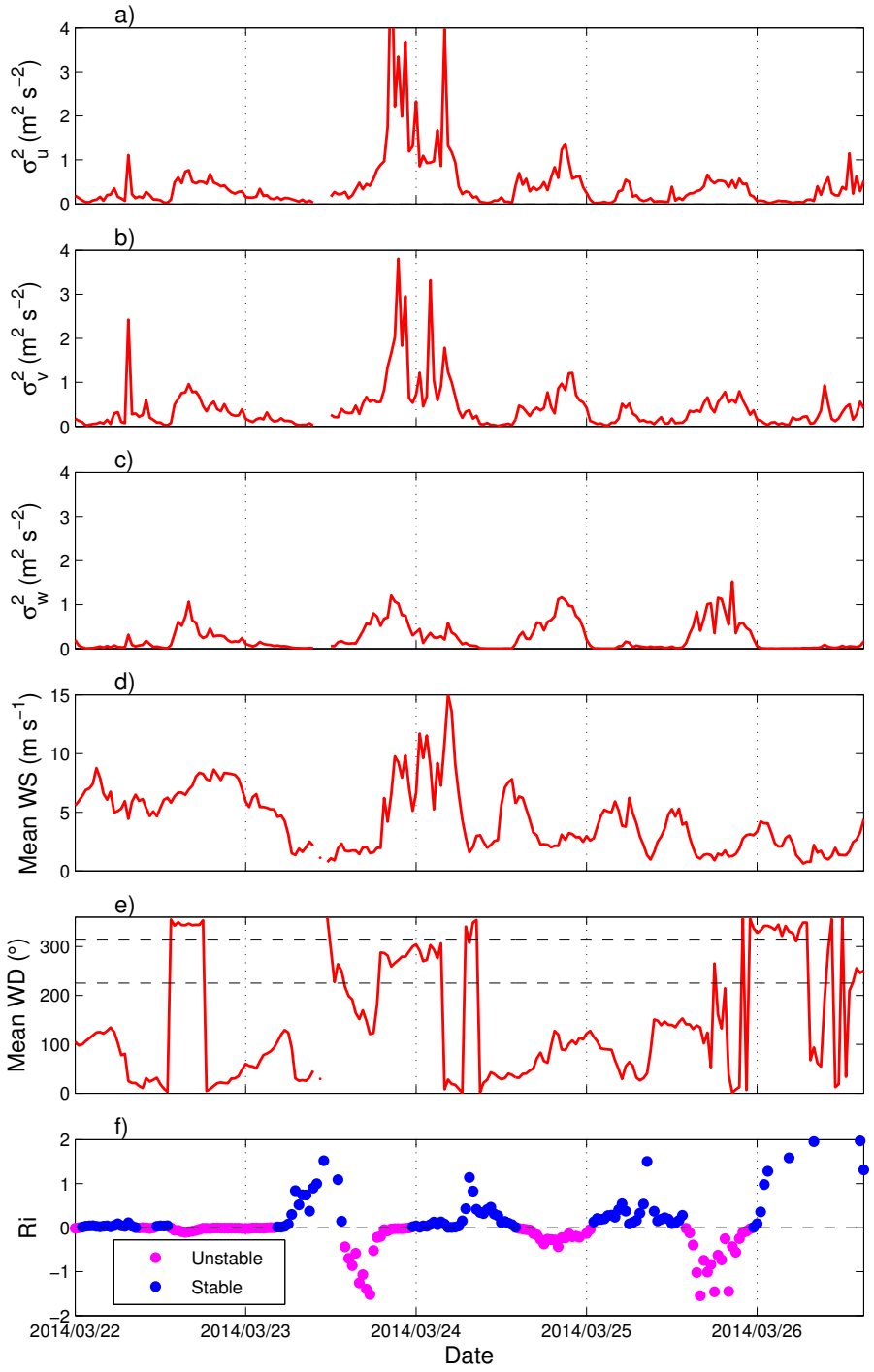

Figure 6.1: 30-min a) *u* variance b) *v* variance c) *w* variance d) mean wind speed and e) mean wind direction at 100 m from sonic anemometers at BAO and f) Richardson number calculated from tower data. Data are shown from 22 to 26 March 2014, and tick marks for each date correspond to 0000 UTC on that day. Horizontal dashed lines in e) indicate range of wind directions excluded in statistical analyses (225–315°).

6.2.1.1 DBS technique: WindCube

During the overnight hours on 25 March, the WindCube DBS technique measured variance values that were approximately equal to or slightly larger than the variance values measured by the sonic anemometers. However, in the latter part of the time series, between 1500 and 2100 UTC, the WindCube substantially overestimated the u and v variance (Figs. 6.2a, b). Sathe et al. (2011) attribute this overestimation of variance to variance contamination, which artificially increases the lidar-measured variance and is most prominent under unstable conditions, when the effects of volume averaging are minimized due to the relatively large turbulent eddy sizes. Turbulence errors can also be induced by horizontal heterogeneity across the lidar scanning circle, as discussed in the following paragraph.

In the DBS technique, the radial wind speeds measured by the four off-vertical beams (north, east, south, and west) are assumed to contain a contribution from the vertical velocity equivalent to the term $w \sin \phi$, where ϕ is the elevation angle measured from ground level. However, when the radial velocity measured by the east and west beams is combined to estimate the value of u, the $w \sin \phi$ terms cancel out, and there is no vertical velocity term in the calculation of u (Eq. 2.28), and likewise for the estimation of v (Eq. 2.29). These terms will only cancel out if the value of w is uniform across the scanning circle, and is thus approximately equal at either side of the scanning circle. This assumption is generally not true under convective conditions, when buoyant turbulent eddies cause alternating fields of updrafts and downdrafts within the scanning circle (e.g., Wainwright et al. 2014).

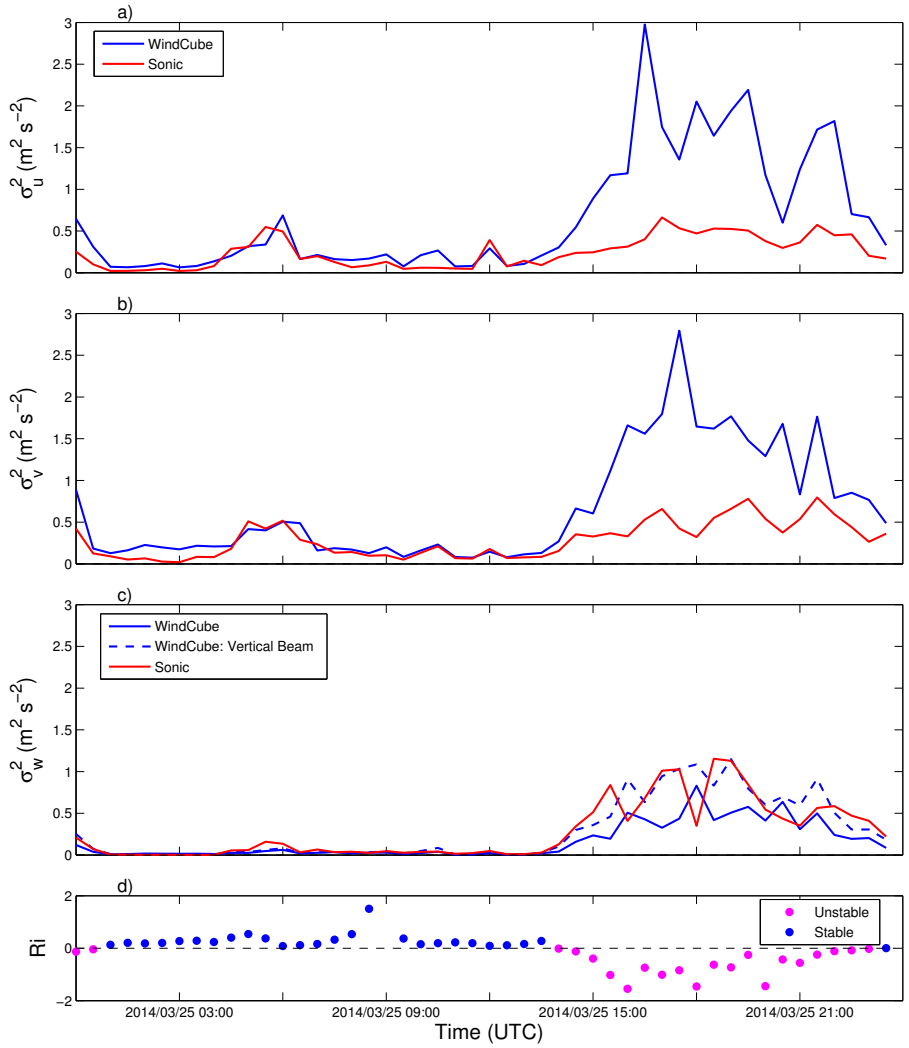

Figure 6.2: 30-min a) *u* variance b) *v* variance, and c) *w* variance at 100 m from sonic anemometers and WindCube DBS technique at BAO and d) Richardson number calculated from tower data. Data are shown from 25 March 2014. In c), solid blue line indicates DBS-calculated *w* variance and dashed blue line indicates *w* variance calculated from vertically pointing beam.

Wainwright et al. (2014) used a sodar simulator to show that the instantaneous DBS-calculated *u* and *v* had root-mean square (RMS) errors as high as 2 m s^{-1} during convective conditions, which was due in part to the horizontal homogeneity assumption. Although the size of the scanning circle increases with height, and one would thus expect that the horizontal homogeneity assumption would become

less valid with increasing height, Wainwright et al. (2014) found that RMS velocity errors decreased with height because the atmosphere was more heterogeneous closer to the surface and turbulent length scales increased with height. The simulated sodar in Wainwright et al. (2014) used an elevation angle of 72.5°, which is similar to the WindCube's elevation angle of 62°.

For large elevation angles, the $w \sin \phi$ term can be quite large and contribute significantly to the radial velocity measured by the off-vertical beams. Indeed, between 1500 and 0000 UTC, the fluctuations in the raw WindCube u and v wind speeds appear to be larger than the fluctuations measured by the sonic anemometers (Figs. 6.3a, b). This time period corresponds to large fluctuations in the sonic and lidar vertical velocity time series as well (Fig. 6.3c), where the sonic and the WindCube lidar measure fluctuations of approximately the same magnitude. These large vertical velocity fluctuations appear to be impacting the u and v velocities measured by the WindCube lidar and artificially increasing the u and v variance (Figs. 6.2a, b). Variance contamination and instrument noise have likely increased the lidar-measured variance as well, although it is difficult to determine which of these effects is most prominent.

The WindCube also overestimated the u and v variance from approximately 0000 to 0500 UTC (Figs. 6.2a, b), although to a much lesser extent than the overestimation that occurred during the afternoon hours. This time period also corresponded to large fluctuations in the WindCube velocity time series that were not

measured by the sonic anemometer (Fig. 6.3). In this case, the large velocity fluctuations were likely due to the low aerosol count of the air at the BAO from 0000 to 0500 UTC, as evidenced by lower SNR values that were measured by the Halo lidar at the beginning of the time series (not shown).

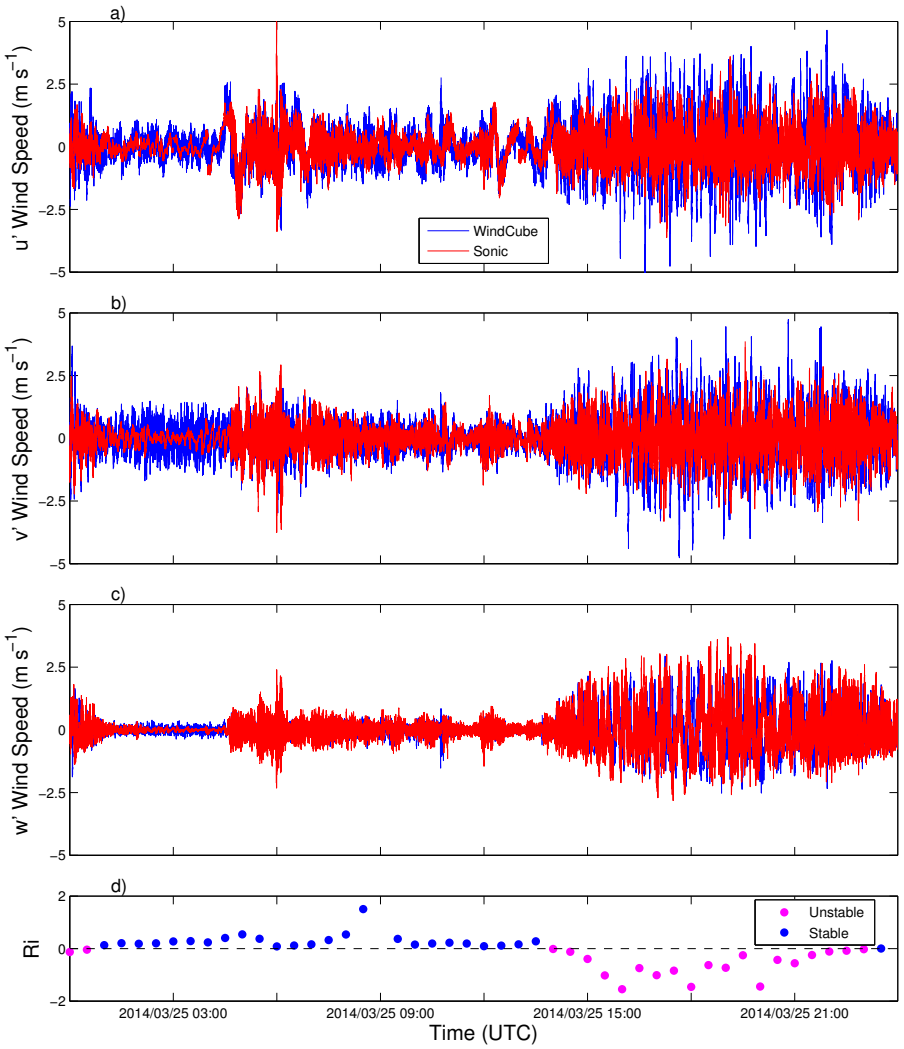

Figure 6.3: a) Raw u wind speed fluctuations from 30-min mean and raw b) v and c) w wind speed at 100 m from sonic anemometers and WindCube lidar at BAO and d) Richardson number calculated from tower data. Data are shown from 25 March 2014. Vertical wind speeds from the WindCube lidar were derived directly from the vertical beam.

For the WindCube v2 lidar, the w variance can be calculated in two ways: 1 Hz values of w can be calculated using Eq. 2.30 and then used to estimate the variance,

or data from the vertically pointed beam position can be used to obtain direct measurements of the *w* variance. As in Ch. 5, both methods were investigated in this chapter to determine the advantage of having a vertically pointed beam position to measure *w* variance. At the BAO, the *w* variance measured by the WindCube lidar's vertical beam was much higher and more accurate than the *w* variance calculated from the DBS equations, particularly under convective conditions (Fig. 6.2c). This discrepancy between the vertical variance values is not surprising, as the vertical beam variance is a measure of the variance directly above the lidar, while the DBS-estimated variance is an average across the scanning circle. In addition, the vertical beam variance is not affected by variance contamination, as it does not require measurements from multiple beam locations. Thus, in all further plots, *w* variance from the WindCube lidar is calculated from the vertical beam. Similar results were found for the WindCube vertical variance estimates during LABLE 2 (Sect. 5.2.1).

6.2.1.2 VAD technique: ZephIR, Halo

During post-processing, a VAD technique (Browning and Wexler 1968) was used to calculate variance from the six-beam Halo data. The five off-vertical beams were fit to a sine curve to estimate the horizontal wind speed, wind direction, and vertical wind speed from each scan (Eqs. 2.32-2.34). This information was then used to create a time series for the *u*, *v*, and *w* components from which the variance could be calculated using a 30-min averaging time. Variance from the Halo VAD

technique was compared to the variance estimated by the ZephIR lidar, which employs a 50-point VAD at each height as part of its scanning strategy, as well as variance measured by the sonic anemometers.

While the ZephIR-estimated u variance values were quite close to those measured by the sonic anemometers and the Halo lidar (Fig. 6.4a), the ZephIR overestimated the v variance under unstable conditions during some half-hourly periods (Fig. 6.4b). The overestimation of the v variance could indicate that the ZephIR lidar VAD technique is affected by contributions from the vertical velocity, similar to the WindCube lidar. Although the WindCube and ZephIR lidars use similar elevation angles (Table 3.1), the overestimation of v variance by the ZephIR lidar was not nearly as large as it was for the WindCube lidar. The ZephIR has variable range gate sizes and takes nearly four times as long to complete a full scan from 10 to 200 m as the WindCube lidar, so the lower temporal resolution of the ZephIR scans may have caused it to measure lower variance values than the WindCube lidar. The Halo lidar produced the most accurate VAD-estimated u and v variance values throughout the day (Figs. 6.4a, b), suggesting that a VAD technique with a lower elevation angle can measure horizontal variance values more accurately. The Halo lidar used an elevation angle of 45° while the WindCube and ZephIR lidars used elevation angles of 62° and 60°, respectively; thus, the contribution of vertical velocity to the Halo radial velocity measurements was much smaller than it was for the other two lidars.

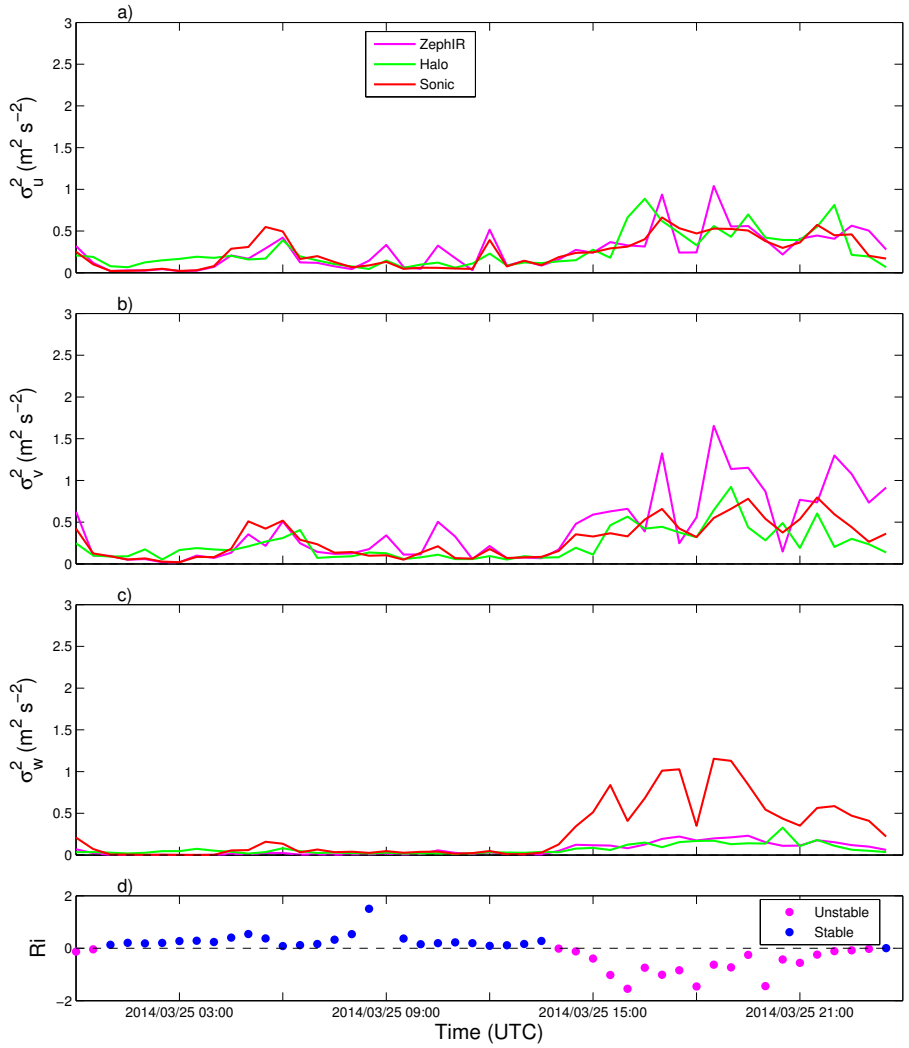

Figure 6.4: 30-min a) *u* variance b) *v* variance, and c) *w* variance at 100 m from sonic anemometers and lidar VAD techniques at BAO and d) Richardson number calculated from tower data. Data are shown from 25 March 2014.

The ZephIR and Halo lidars measured similar *w* variance values with the VAD technique, which were underestimates in comparison to the sonic anemometer values for nearly all stability conditions throughout the day (Fig. 6.4c). As previously mentioned, the most accurate lidar method for measuring the *w* variance appears to be the use of a vertical beam position to obtain a direct measurement of the vertical wind speed (Fig. 6.2c).

6.2.1.3 Halo: Six-beam technique

The WindCube and ZephIR lidars are commercially available lidars with scanning strategies that cannot be changed by the user. However, the Halo lidar is a research-grade scanning lidar that can be used to implement user-defined scanning strategies. Thus, the Halo lidar was used to evaluate the six-beam technique at the BAO.

The six-beam technique is different than the variance measurement methods used by the sonics and WindCube and ZephIR lidars. The other techniques involve finding values of u, v, and w, rotating these values into the coordinate system where u is aligned with the mean wind direction (Eqs. 4.1-4.3), and then calculating the variance values from these rotated wind speed components. In contrast, the six-beam technique involves first determining the original variance components from the variances of the radial velocities, then rotating these variance components into the new coordinate system (Eqs. 2.40-2.42). Thus, it is possible that discrepancies could result from the different methods of estimating variance.

Sonic anemometer data were first used to test the ability of the six-beam technique to accurately measure the variance values σ_u^2, σ_v^2, and σ_w^2. The variance was calculated from the sonic anemometer data in two ways: 1) The raw sonic data were rotated such that u was aligned with the mean wind direction and $\overline{v} = 0$ (Eqs. 4.1-4.3). Next, the variance was calculated using standard Reynolds averaging. 2) The raw sonic data were projected into the six beam positions used

in the six-beam technique and the variances of these radial velocities were calculated. Equations 2.37-2.39 were then used to calculate the variance components in the unrotated coordinate system. Finally, the variance components were rotated into the new coordinate system using Eqs. 2.40-2.42. Method 1 is the method used by the sonics, WindCube lidar, and ZephIR lidar, while Method 2 mimics the technique that would be used by the Halo lidar.

The resulting variance time series plots are shown in Fig. 6.5. The variance values produced from the different methods are nearly always the same, although some small discrepancies occur in the u and v variance values between 1500 and 0000 UTC (Figs. 6.5a, b). These discrepancies likely occurred because the six-beam technique uses the 30-min mean wind direction for the coordinate rotation while the standard technique used with the sonic data uses the 10-min mean wind direction (Sect. 4.3) and the wind direction was variable on the afternoon of 25 March (Fig. 6.1e). However, in general, both methods produce very similar variance values.

Next, variance measured using the six-beam technique with the Halo lidar was compared to variance measured by the sonic anemometers with the standard technique (Fig. 6.6). Similar to the WindCube lidar, the six-beam technique includes a vertically pointed beam to obtain a direct measurement of the vertical velocity. Vertical variance estimated by the Halo six-beam technique was much higher and more accurate than the vertical variance measured by the Halo VAD technique (Figs. 6.4c, 6.6c). However, larger discrepancies occurred in the u and v variance

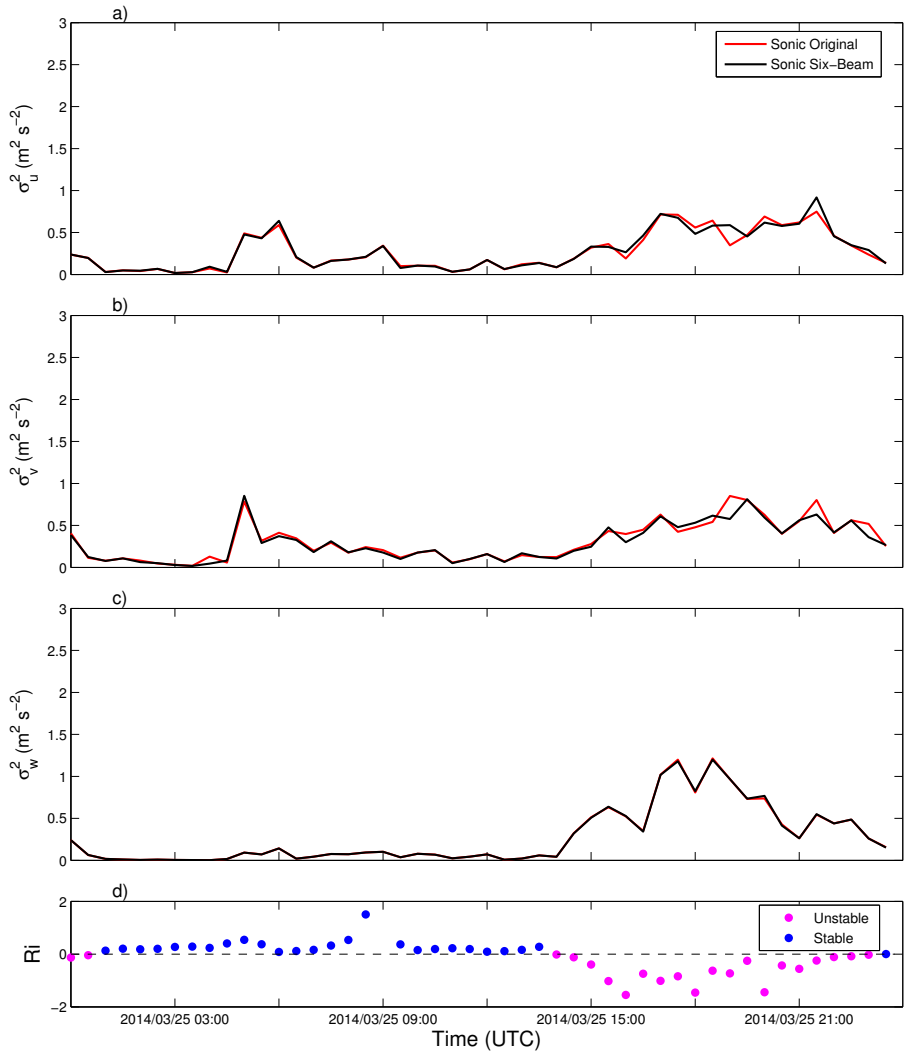

Figure 6.5: 30-min a) u variance b) v variance, and c) w variance at 200 m from sonic anemometers at BAO and d) Richardson number calculated from tower data. Data are shown from 25 March 2014. Red line denotes original sonic variance calculation and black line denotes variance calculated using projected sonic velocity values with six-beam technique.

values. During strongly unstable conditions from 1700 to 2100 UTC, the Halo six-beam technique often underestimated the u and v variance in comparison to the sonic anemometers (Figs. 6.6a, b). In some extreme cases, the u and v variance values became negative, which should be mathematically impossible given the definition of variance ($\sigma_{u_i}^2 = \overline{(u_i - \overline{u_i})^2}$).

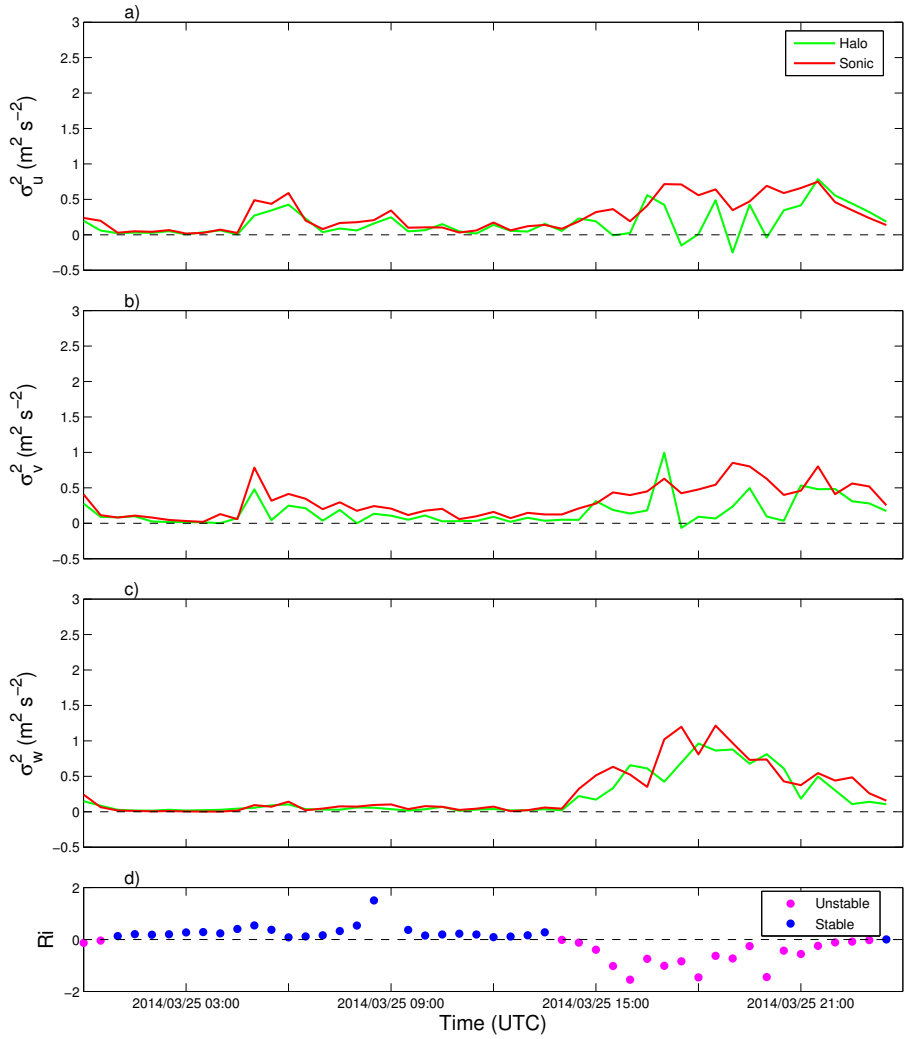

Figure 6.6: 30-min a) *u* variance b) *v* variance, and c) *w* variance at 200 m from sonic anemometers and Halo lidar six-beam technique at BAO and d) Richardson number calculated from tower data. Data are shown from 25 March 2014.

In order to determine the cause of this horizontal variance underestimation and the negative variance values, it is instructive to examine the equations used to calculate the variance components with the six-beam technique (Eqs. 2.37–2.39). Equations 2.37 and 2.38 for the *u* and *v* variance, respectively, both include the term $-\overline{v_{r6}'^2}$, meaning that the variance calculated from the vertical beam radial velocity is subtracted from the combination of the other terms. Thus, when $\overline{v_{r6}'^2}$ is large, as is often the case under convective conditions (Fig. 6.6c), or overestimated

due to instrument noise, a large value is subtracted in Eqs. 2.37 and 2.38, and the u and v variance can become negative if the other radial variances are not measured accurately. The other negative terms in Eqs. 2.37 and 2.38 could also decrease the horizontal variance components and cause them to become negative. Similarly, if the positive terms in Eqs. 2.37 and 2.38 are underestimated, the variance values would also likely be underestimated. Although negative values of σ_u^2 and σ_v^2 only comprised approximately 5% of the horizontal variance values at 200 m during the 5-day analysis period, the underestimation of the horizontal variance components by the Halo six-beam technique is a significant issue that warrants further investigation.

The projected sonic anemometer data were next used to assess the accuracy of the Halo lidar measurements from each beam position. Scatter plots of 30-min mean radial wind speeds are shown in Fig. 6.7 and scatter plots of 30-min variance are shown in Fig. 6.8. Mean radial wind speeds measured by the different Halo beam positions were generally in agreement, although there is some scatter about 0 m s^{-1} for the v_{r6} component, possibly indicating that the lidar was not completely level (Fig. 6.7). The Halo lidar generally underestimated the variance for each beam position, with larger underestimations occurring for stable conditions, as expected (Fig. 6.8).

Time series plots of the 30-min mean radial wind speeds and radial variance values measured by the sonics and Halo lidar on 25 March 2014 are shown in Figs. 6.9 and 6.10. During the afternoon of 25 March, mean wind speeds were very

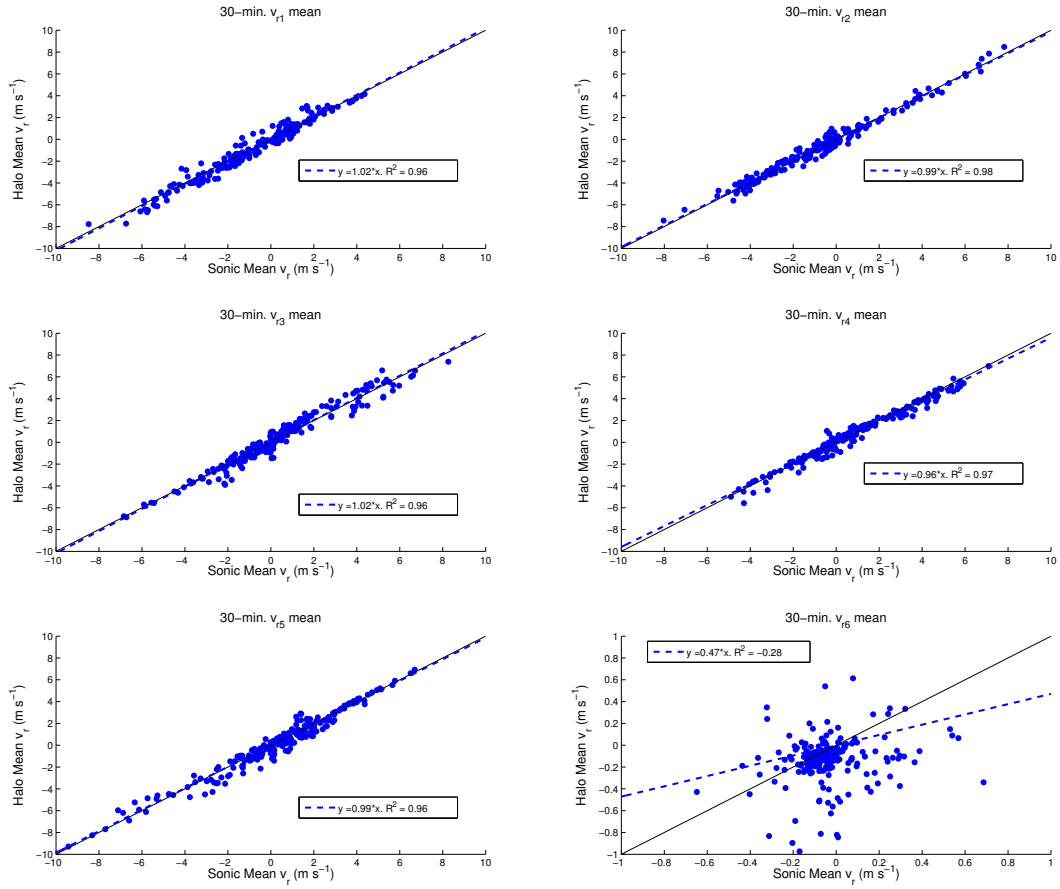

Figure 6.7: 30-min mean radial wind speeds at 200 m from different beam positions measured by Halo lidar and estimated from sonic anemometer projections at BAO. Beam positions 1–5 have an elevation angle of 45° and azimuth angles ranging from 0 to 288° in increments of 72° and beam position 6 is the vertically pointing beam. Data are shown from 22 to 26 March 2014. Linear regression fits are indicated by dashed lines and equations are shown in figure legends.

low (Fig. 6.1d), which is reflected by the low radial wind speeds measured by the Halo lidar and calculated from the projected sonic data (Figs. 6.9a-f). Some minor differences in the radial wind speeds measured by the Halo and sonic anemometer were evident in the late afternoon, as well as strongly underestimated and negative Halo u and v variance values (Figs. 6.9g, h). The largest discrepancies between the radial variance values also occurred in the late afternoon, when the Halo strongly underestimated the variance of the radial velocity at the third, fourth, and fifth beam positions (Figs. 6.10c-e). In the initial six-beam equations, terms $\overline{v_{r3}'^2}$, $\overline{v_{r4}'^2}$,

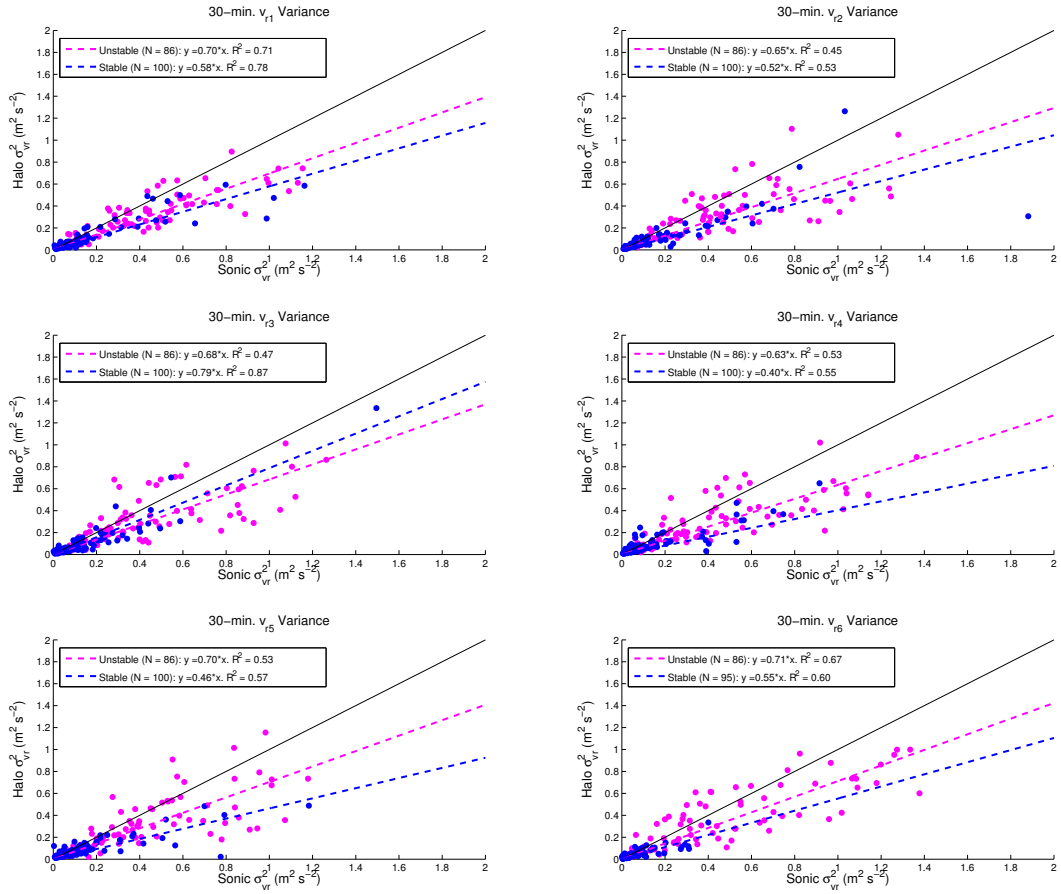

Figure 6.8: 30-min variance at 200 m from different beam positions measured by Halo lidar and estimated from sonic anemometer projections at BAO. Beam positions 1–5 have an elevation angle of 45° and azimuth angles ranging from 0 to 288° in increments of 72° and beam position 6 is the vertically pointing beam. Data are shown from 22 to 26 March 2014 and stratified by stability. Linear regression fits are indicated by dashed lines and equations are shown in figure legends.

$\overline{v'^2_{r5}}$ have positive coefficients in the u variance equation (Eq. 2.37), and terms $\overline{v'^2_{r3}}$ and $\overline{v'^2_{r4}}$ have positive coefficients in the v variance equation while the $\overline{v'^2_{r5}}$ term has a negative coefficient (Eq. 2.38). The actual coefficients of the radial beam variances will change once the coordinate rotation is applied, but for the most part, weighted values of $\overline{v'^2_{r3}}$, $\overline{v'^2_{r4}}$, and $\overline{v'^2_{r5}}$ are added to the weighted values of the other radial beam variances to obtain values for the u and v variance. Thus, if the variance measured at beam positions 3, 4, and 5 is underestimated, the u and v variance will also be underestimated. Similar trends were also observed on 24 March 2014 (not shown).

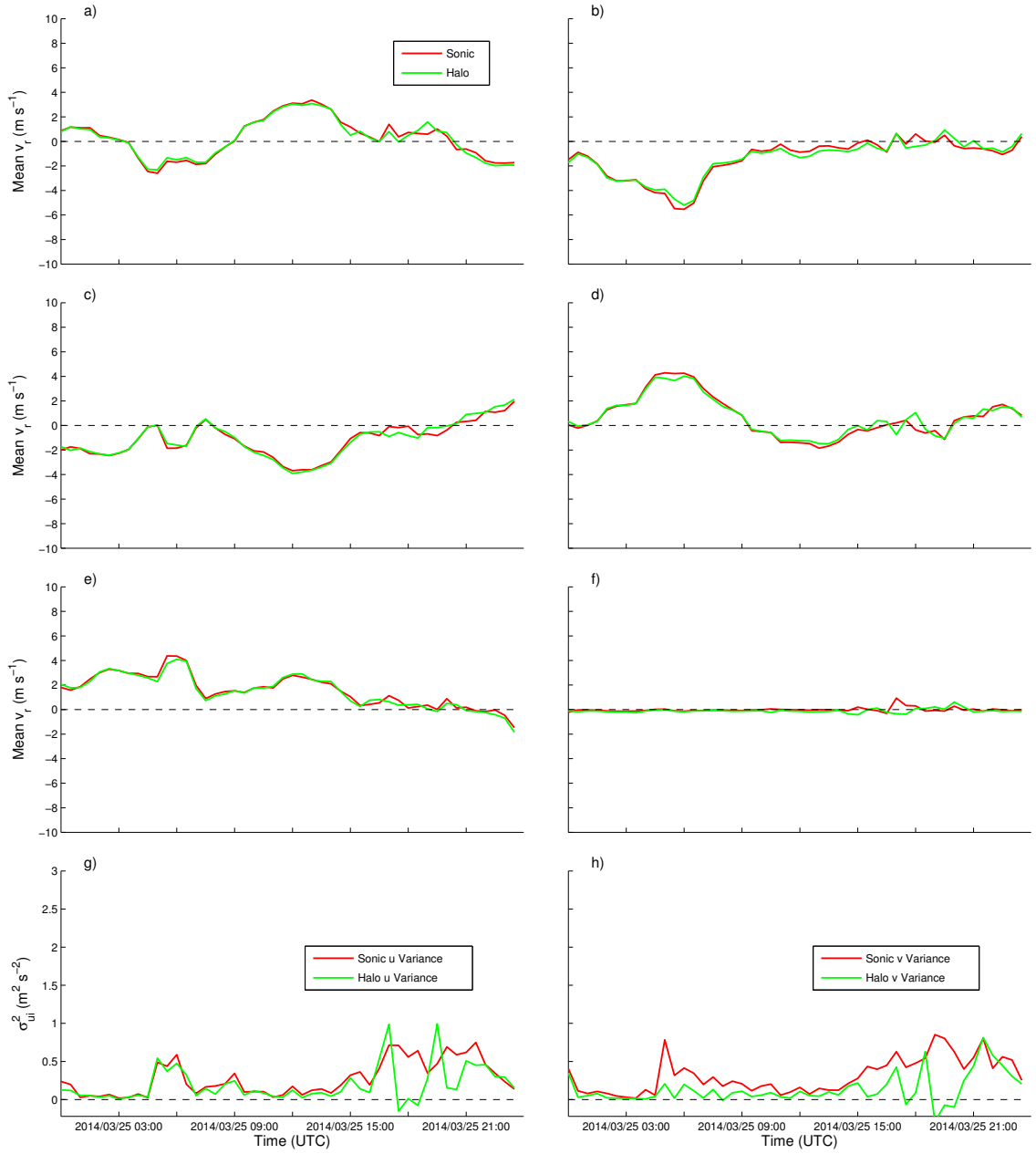

Figure 6.9: 30-min a) v_{r1} b) v_{r2} c) v_{r3} d) v_{r4} e) v_{r5} and f) v_{r6} mean velocity values measured by Halo lidar and calculated from projected sonic data. Values of g) u variance and h) v variance are also shown for reference, where sonic values are from standard variance calculation and Halo values are from six-beam calculation. Data are shown from 25 March 2014 at 200 m AGL.

It is not completely clear why the Halo lidar underestimates the variance at certain beam positions more strongly than at other beam positions, although this discrepancy could be associated with horizontal heterogeneity across the lidar scanning circle. The six-beam technique makes the assumption that the flow is

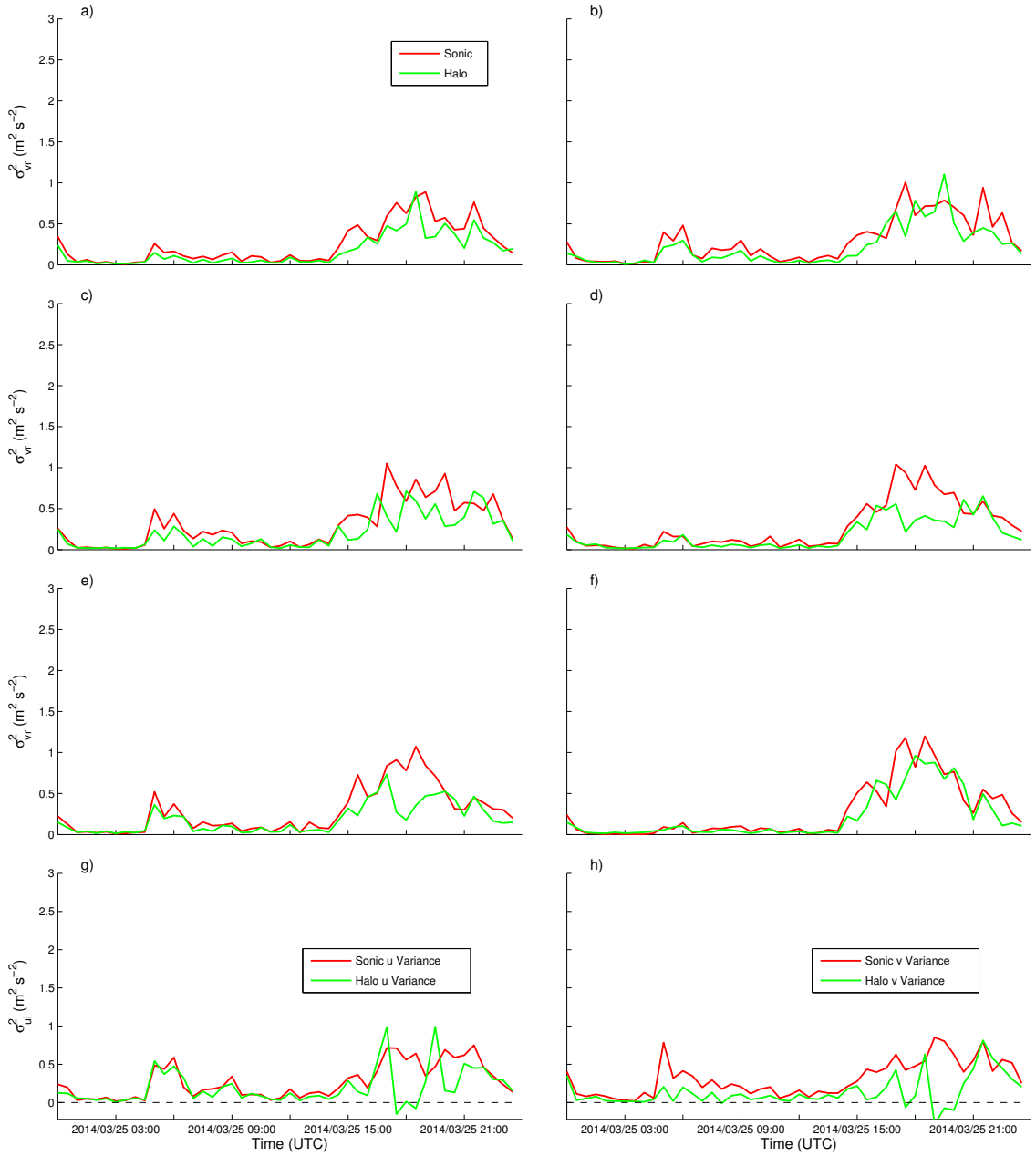

Figure 6.10: 30-min a) v_{r1} b) v_{r2} c) v_{r3} d) v_{r4} e) v_{r5} and f) v_{r6} variance values measured by Halo lidar and calculated from projected sonic data. Values of g) u variance and h) v variance are also shown for reference, where sonic values are from standard variance calculation and Halo values are from six-beam calculation. Data are shown from 25 March 2014 at 200 m AGL.

homogeneous in the scanning circle encompassed by the five off-vertical beams, and this assumption appears to be invalid under unstable conditions (Sect. 6.2.1.1). Horizontal heterogeneity and high values of variance could cause large amounts of scatter about the VAD sine curve (Weitkamp 2005). The differences between

the instantaneous radial velocities and the fit VAD sine curve (Eq. 2.31) were examined for 25 March, but no noticeable differences were evident for the different beam positions, although residuals were much larger under unstable conditions. A modeled flow field and lidar simulator would likely be needed to definitively quantify the effect of horizontal heterogeneity on the variances measured by the different lidar beam positions.

Relative intensity noise (RIN) also may have affected the variance values measured by the Halo lidar on 25 March. RIN results from spontaneous radiation emissions from the laser, which cause intensity fluctuations in the laser oscillator (Chang 2005). In a coherent heterodyne lidar, RIN appears as pink noise; i.e., it is mainly present in the low-frequency part of the Doppler spectrum (Courtney et al. 2008). Since low wind speeds would also be detected in the low frequency part of the spectrum, RIN can impact the accuracy of Doppler velocity measurements under low wind speeds. Peña et al. (2009) found that a ZephIR lidar most strongly underestimated the turbulence intensity measured by cup anemometers when weak wind speeds were measured.

As several of the Halo radial beams measured radial wind speeds that were close to 0 m s^{-1} during the afternoon of 25 March (Figs. 6.9a-f), it is possible that RIN caused the Halo lidar to underestimate the variance at certain beam positions. To further investigate this possibility, mean radial velocity and variance values were calculated for 6 March 2014, a date from the campaign when atmospheric conditions were less strongly convective and wind speeds were higher during the

late afternoon (Figs. 6.11 and 6.12). Although there were some small biases in the radial wind speed measurements from the Halo lidar (Figs. 6.11a-f), there were no large discrepancies in the radial variance measurements on 6 March (Figs. 6.12a-f) and no strongly underestimated or negative u and v variance values (Figs. 6.12g-h). (Note that the variance values measured under unstable conditions on 6 March were smaller than those measured on 25 March, likely because the atmosphere was less strongly convective.) The six-beam technique thus appears to be more accurate when wind speeds are higher (Figs. 6.9-6.12), as radial variance estimates are more accurate under higher wind speed conditions and more accurate horizontal variance estimates are produced as a result. In the future, the relation between Halo variance underestimation and radial wind speed should be investigated to determine if a threshold radial wind speed can be derived for the calculation of variance with the six-beam technique.

Finally, it is possible that the temporal resolution of the Halo observations affects the accuracy of the variance measured at each of the beam positions. This factor is investigated in Sect. 6.3.

6.2.1.4 Turbulence under different stability conditions

Variance values from 22 to 26 March 2014 were stratified by stability class, with $Ri > 0.1$ indicating stable conditions, $Ri < -0.1$ indicating unstable conditions, and $-0.1 \leq Ri \leq 0.1$ indicating near-neutral conditions, as discussed in Sect. 4.5. The 22 to 26 March data period was selected because the lidars had good data

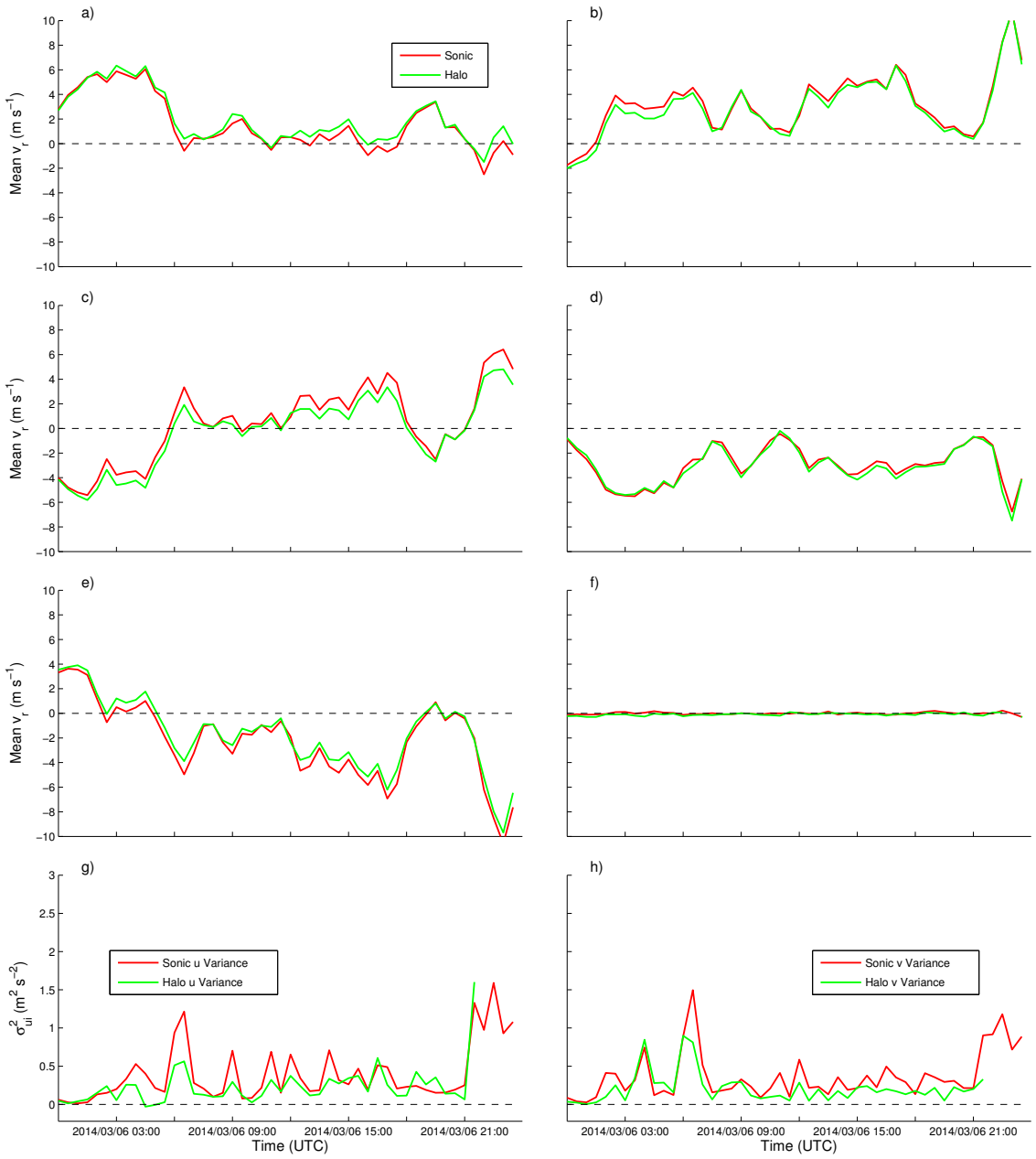

Figure 6.11: As in Fig. 6.9, but for 6 March 2014.

availability and conditions at the BAO were clear and calm with little precipitation (Figs. 3.8 and 3.9). Figure 6.13 shows scatter plots of the variance measured by the different lidar scanning techniques and the sonic anemometers on the tower during this 5-day period, with data only shown for heights with good data availability (100

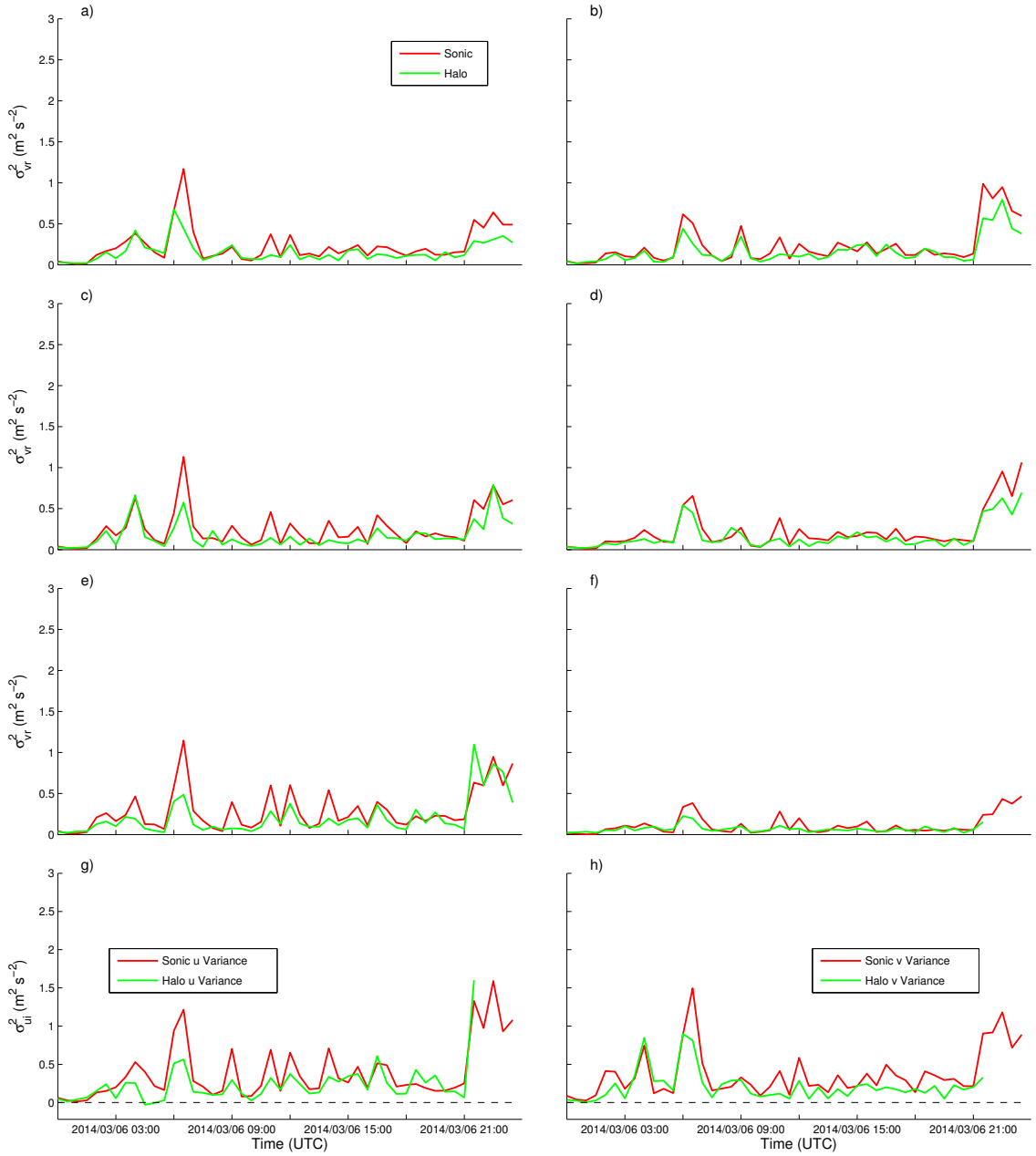

Figure 6.12: As in Fig. 6.10, but for 6 March 2014.

m for the WindCube and ZephIR lidars and 200 m for the Halo lidar). Regression line fits for the lidar variance values are summarized in Table 6.1.

The WindCube DBS technique nearly always overestimated the *u* and *v* variance, particularly under unstable conditions (Fig. 6.13a). On average, the WindCube lidar measured *u* and *v* variance values that were over twice as large than the

Instrument: Scanning Strategy	**Slope US**	**Slope N**	**Slope S**	R^2 **US**	R^2 **N**	R^2 **S**
u Variance						
WindCube: DBS	2.3	1.1	0.89	0.27	0.89	0.66
ZephIR: VAD	1.1	0.29	0.69	0.62	-0.24	0.4
Halo: Six-Beam	0.51	0.34	0.82	0.084	0.3	0.88
Halo: VAD	0.74	0.29	0.55	0.07	0.21	0.73
v Variance						
WindCube: DBS	2.5	1.2	1.2	0.33	0.94	0.6
ZephIR: VAD	2	0.26	1	-0.075	-0.66	0.22
Halo: Six-Beam	0.51	0.79	0.69	0.14	0.48	0.87
Halo: VAD	0.65	0.87	0.78	0.62	0.5	0.95
w Variance						
WindCube: DBS	0.92	0.8	0.65	0.45	0.9	0.08
ZephIR: VAD	0.23	0.48	0.41	0.25	0.6	0.46
Halo: Six-Beam	0.73	0.66	0.75	0.46	0.75	0.82
Halo: VAD	0.18	0.22	0.29	0.052	0.76	0.57

Table 6.1: Regression line slopes and coefficient of determination (R^2) values for lidar variance for different stability classes shown in Fig. 6.13. Negative R^2 values indicate that a linear fit is not appropriate for the dataset. Results are shown for unstable (US), near-neutral (N), and stable (S) conditions, as defined in the text.

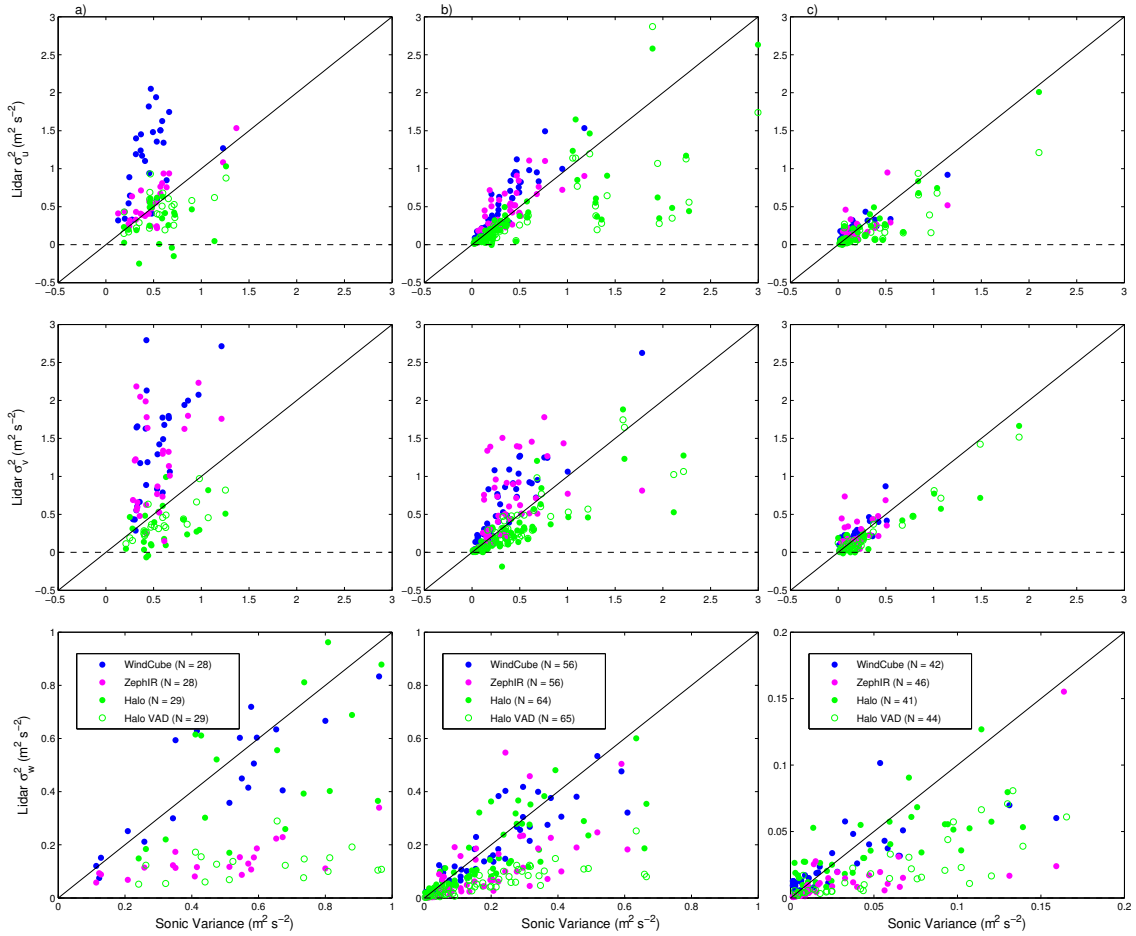

Figure 6.13: Scatter plots of sonic variance versus lidar variance under a) unstable b) neutral and c) stable conditions at BAO from 22 to 26 March 2014. Top, middle, and bottom rows show u, v, and w variance, respectively.

values measured by the sonic anemometers under unstable conditions, although there was quite a bit of scatter ($R^2 = 0.27$ and 0.33 for the u and v variance, respectively) . The overestimation of the u and v variance by the WindCube lidar is larger than that found by Sathe et al. (2011), who found mean slopes between 1 and 1.6 under unstable conditions. However, Sathe et al. (2011) had a much larger dataset available and were able to classify the variance values into seven stability classes rather than the three used here. In addition, Sathe et al. (2011) defined -50 m as the 10-m Obukhov length cut-off for very unstable conditions, which corresponds

to a value of $\zeta = z/L = -0.2$, or approximately, $Ri = z/L = -0.2$, where z/L and *Ri* are approximately equivalent under unstable conditions (Businger et al. 1971). For the data shown in Fig. 6.13a for unstable conditions at the BAO, over 85% of the values of *Ri* were smaller than -0.2. Thus, most of the variance values shown in Fig. 6.13a occurred in more strongly unstable conditions than in Sathe et al. (2011), which is likely the cause for the discrepancy.

Like the WindCube lidar, the ZephIR VAD technique often overestimated the *u* and *v* variance for unstable conditions (Fig. 6.13a), with larger overestimates occurring for the *v* component, similar to results found in Sathe et al. (2011), although the overestimation was not as strong for the Denmark study. Sathe and Mann (2012) noted increased spectral energy in modeled and measured WindCube *v* spectra in comparison to sonic anemometers on a tower, which would serve to increase estimates of σ_v^2, although it is not clear why this occurs. In contrast to the WindCube and ZephIR lidars, the Halo VAD technique measured lower *u* and *v* variance values under unstable conditions that were generally closer to the variance measured by the sonic anemometers.

The Halo six-beam technique tended to underestimate the *u* and *v* variance values, especially for unstable conditions when horizontal heterogeneity or RIN may have affected the variance values measured at different points around the scanning circle (Sect. 6.2.1.3). In fact, nearly all of the negative *u* and *v* variance values were associated with unstable conditions (Fig. 6.13a).

Most *w* variance values measured by the Halo six-beam technique, however, were close to the variance measured by the sonic anemometers, with regression line slopes exceeding 0.6 for all stability classes (Table 6.1). The use of this vertical beam to directly measure the vertical velocity appears to be a necessity in accurately estimating the vertical variance. The *w* variance values measured by the VAD techniques were large underestimates; for example, the ZephIR-estimated *w* variance had regression line slopes of 0.23, 0.48, and 0.41 for unstable, neutral, and stable conditions, respectively (Table 6.1). This indicates that the VAD technique is not an accurate technique for measuring the vertical variance under most stability conditions, in accordance with the findings of Sathe et al. (2011).

6.2.2 Comparison of turbulence parameters: LABLE 2

Time series of 30-min variance values measured at several heights during LABLE 2 on 21 June 2013 are shown in Fig. 6.14. (Note that sonic anemometer data were only available at 60 m and could thus only be compared to WindCube data.) Similar to the procedure implemented during LATTE, the OU Halo lidar was used to evaluate the six-beam technique while the WindCube lidar operated in normal DBS mode. The Galion lidar mimicked the DBS technique used by the WindCube lidar but employed an elevation angle of 45° to match the elevation angle of the OU Halo lidar and to maximize overlapping measurement heights among the different lidars.

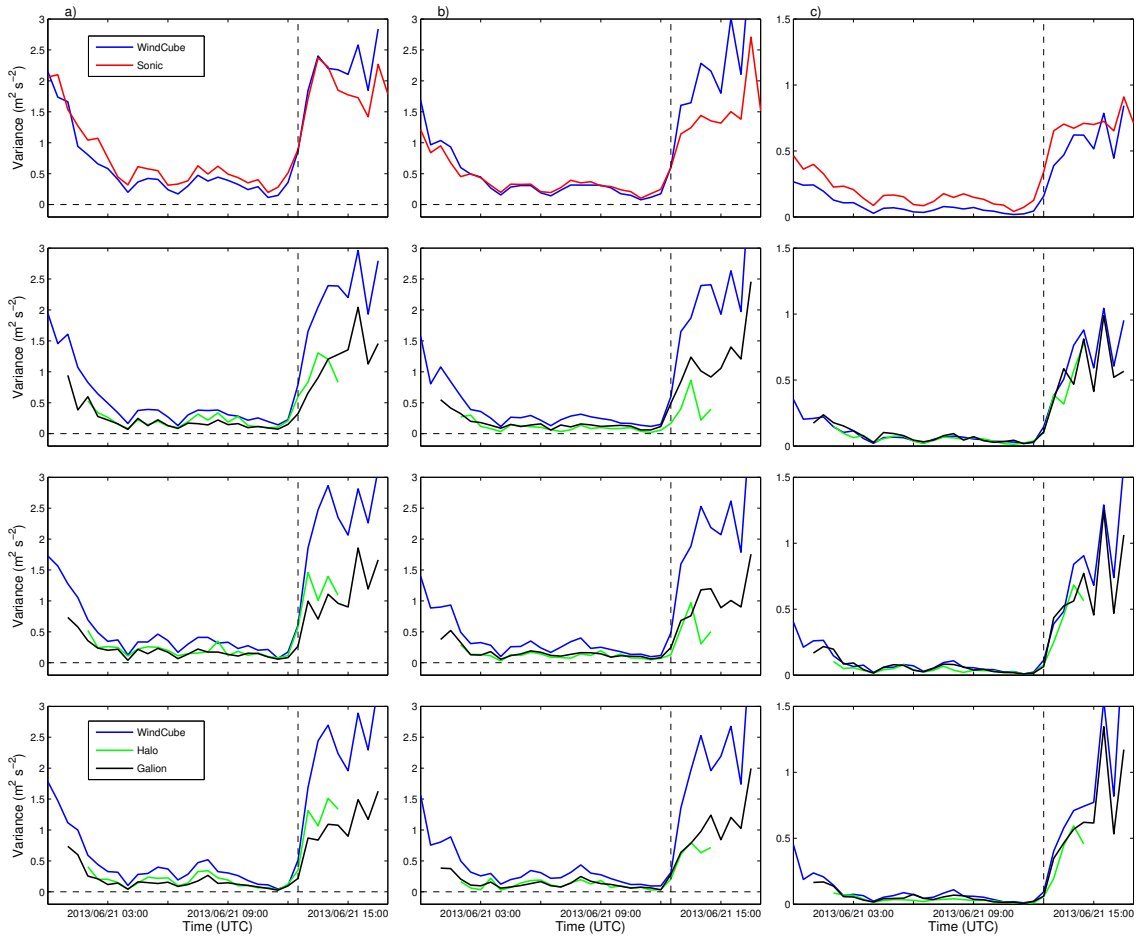

Figure 6.14: Time series of 30-min a) *u* variance b) *v* variance and c) *w* variance at ARM site on 21 June 2013. Variance from 60 m (top row), 95 m (second row), 159 m (third row), and 200 m (last row) is shown. Dashed vertical line marks approximate transition from stable to unstable conditions. Results from WindCube DBS technique, Halo six-beam technique, Galion DBS technique, and 60-m sonic anemometer are shown.

Diurnal trends in the LABLE 2 turbulence parameters are similar to those seen in the LATTE data: turbulence is fairly low overnight (stable conditions) before increasing during daytime, convective conditions. However, variance values experienced under stable conditions on 21 June 2013 at the ARM site are generally larger than those experienced under stable conditions at the BAO, particularly for the *u* and *v* variance (Figs. 6.1, 6.14). Mean wind speeds were also much larger at 95 m than they were at 100 m at the BAO. These differences are likely due

to the prominence of the nocturnal LLJ in the Southern Plains during the spring and summer months (Song et al. 2005), which was a primary focus of LABLE 2 (Klein et al. 2015). Although the LLJ core was several hundred meters above the highest WindCube lidar measurement height on this night, there was still a significant amount of wind speed and direction shear in the lowest 100 m AGL (not shown), which would significantly affect wind power production and loads on turbine blades at a wind farm. Wind shear associated with the LLJ can often induce mechanically generated turbulence below the LLJ core (e.g., Mahrt et al. 1979; Banta et al. 2006), which is likely the cause for the small spikes in the u variance between 0500 and 0900 UTC. At 60 m AGL, these variance spikes are underestimated by the WindCube lidar in comparison to the 60-m sonic anemometer, suggesting that the majority of the turbulent scales of motion under stable conditions were too small to be measured by the lidars (Fig. 6.14).

Above 60 m, the WindCube u and v variance values were generally larger than the variance measured by the scanning lidars, particularly for unstable conditions (Figs. 6.14a, b). This increased variance could be, in part, the result of a difference in range gate size; while the WindCube lidar uses 20-m range gates, the scanning lidars generally use 30-m range gates, which would lead to more volume averaging and lower variance values measured by the scanning lidars, as discussed in Ch. 5. However, the vertical variance measured by all three lidars is nearly identical (Fig. 6.14c). Thus, it appears likely that the difference in elevation angle played a role in the WindCube's overestimation of the horizontal velocity variance

components; as previously discussed, contributions from the vertical velocity will increase the u and v values calculated from the WindCube data, increasing the perceived horizontal turbulent fluctuations. The WindCube also often measured higher u and v variance values than the 60-m sonic anemometer under unstable conditions, further suggesting that the horizontal velocity fluctuations are affected by both variance contamination and horizontal heterogeneity across the scanning circle (Figs. 6.14a, b).

The Galion lidar, which also used a DBS technique, measured smaller u and v variance values than the WindCube lidar. This further suggests that by choosing a different elevation angle with the DBS technique, the contribution of the vertical velocity to the horizontal velocity components can be reduced. However, it is difficult to independently determine the effect of the scanning angle on variance overestimation, as the Galion lidar had larger range gates and a longer scan time than the WindCube lidar (Table 3.1).

In contrast to the LATTE data (Fig. 6.6), the u and v variances calculated using the six-beam technique were close to the variance values measured by the other lidars, and very few Halo variance values were negative during the six-beam part of the experiment (Figs. 6.14a, b). In order to compare the variance values experienced at the different sites, histograms of the square root of the variance components normalized by the mean horizontal wind speed are shown in Figs. 6.15 and 6.16 for the BAO and ARM site, respectively. Variance ratios in Figs. 6.15 and 6.16 are color-coded by stability, with $Ri > 0$ and $L > 0$ corresponding to

stable conditions and $Ri < 0$ and $L < 0$ corresponding to unstable conditions. A Wilcoxon rank sum test (Wilks 2006) was used to test the null hypothesis that the stable and unstable ratios for each variance component were drawn from samples with the same median and continuous distributions. This null hypothesis was rejected for all variance ratios at the 5% level, implying that the stable and unstable variance ratio distributions are statistically different. The Wilcoxon rank test was also used to compare the variance ratios from the ARM site and the BAO, with the null hypothesis that the variance ratios from the two sites were drawn from a distribution with the same sample median again being rejected at the 5% level.

The ratios of all three variance components, particularly σ_w, are strongly skewed toward lower values at the ARM site. SNR values were generally much higher at the ARM site than at the BAO as a result of the higher aerosol content, so these higher SNR values likely led to less noisy vertical variance estimates and smaller values of $\sigma_w/\overline{u}$ in Fig. 6.16c. However, it is difficult to determine if higher vertical variance values were measured during the late afternoon period, as the six-beam lidar measurements were only available until approximately 1600 UTC every day when the scanning strategies were switched for a different experiment.

6.3 Effects of temporal resolution

The temporal resolution between the sonic anemometers and the lidars at the BAO is different; while the NCAR and OU sonics collect data at frequencies of 60 and

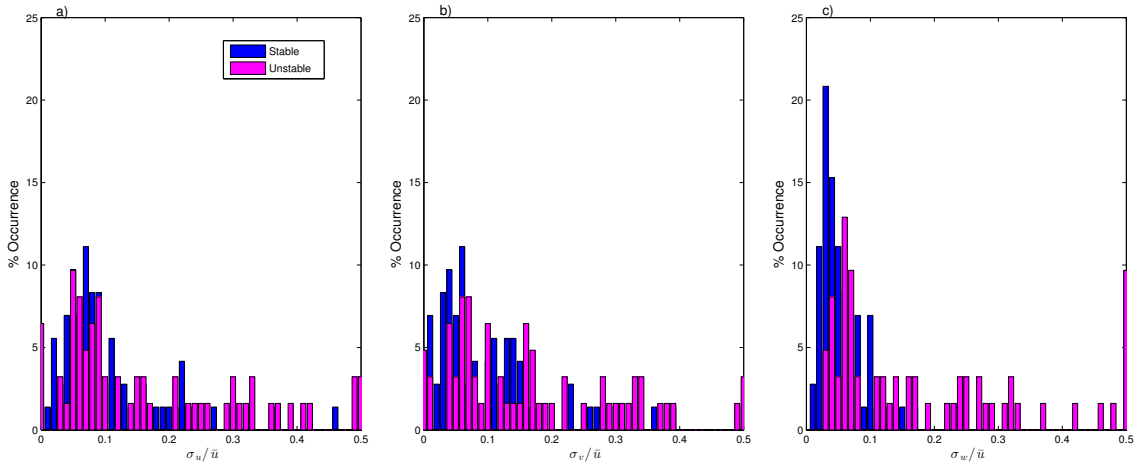

Figure 6.15: Histograms of the 30-min a) *u* standard deviation b) *v* standard deviation and c) *w* standard deviation at 200 m normalized by the 30-min mean wind speed from Halo six-beam data at the BAO. Data are shown from 22 to 26 March 2014.

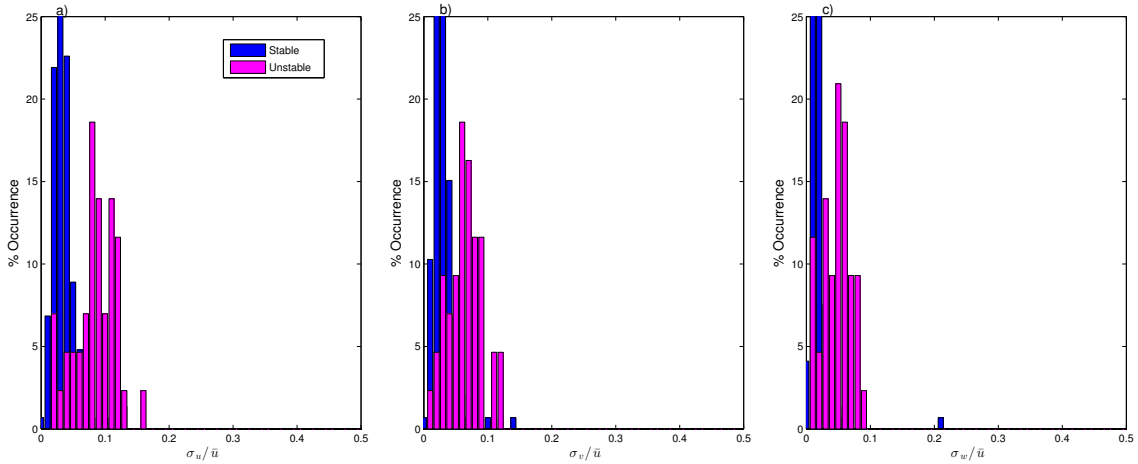

Figure 6.16: As in Fig. 6.15, but for 21 to 26 June 2013 at the ARM site.

30 Hz, respectively, the lidars collect data at a frequency of 1 Hz, with most scanning strategies taking much longer than one second. In order to approximate the temporal resolution needed to accurately measure turbulence at the BAO, the integral time scale, τ, was calculated from the NCAR sonic anemometer at 100 m AGL for the period from 22 to 26 March 2014. The integral time scale represents the temporal scale over which turbulence in the different directions remains correlated and can be described by the following equation: (Kaimal and Finnigan 1994).

$$\tau_{u_i} = \int_0^\infty \rho_{u_i}(\xi)d\xi = \int_0^\infty \frac{\overline{u_i'(t)u_i'(t+\xi)}}{\sigma_{u_i}^2}d\xi, \tag{6.1}$$

where τ_{u_i} (s) is the integral time scale corresponding to velocity components u_i (m s^{-1}) for i = 1, 2, 3, ρ is the autocorrelation function (unitless), ξ is the time lag from time t (s), and $\sigma_{u_i}^2$ is the velocity variance (m^2 s^{-2}). The mean estimated integral length scales for different stability classes are shown in Table 6.2. As expected, the time scales for the u and v components are larger than those for the w components. The mean integral time scales for u and v are approximately 50–55 s under unstable and neutral conditions while the mean integral time scale for w is 40 s under unstable conditions and 14 s under neutral conditions. The stable integral time scales for all three components appear to be much too large, particularly for the u and v components. These larger values likely occurred because variance values were small under stable conditions (e.g., Fig. 6.1) and these low values of variance in the denominator of Eq. 6.1 resulted in unrealistically large values of the integral time scale. However, large values of τ for the u and v components under stable conditions may have been due to nocturnal wave activity.

Based on models and experimental data, Lenschow et al. (1994) determined that large errors in flux estimates occur when the temporal resolution of the samples is approximately equal to or larger than the integral time scale. Thus, it is likely that the 30-s temporal resolution of the Halo six-beam scans causes some errors in flux estimates, particularly for the w component. The 15-s resolution of the ZephIR scans could induce errors as well.

Integral Time Scale (s)			
Velocity Component	**Unstable**	**Neutral Time Scale**	**Stable Time Scale**
u	48	55	74
v	52	57	88
w	40	14	28

Table 6.2: Mean integral time scales estimated from 100 m NCAR sonic at BAO from 22 to 26 March 2014. Time scales are shown in seconds for different stability classifications.

In order to examine the effect of temporal resolution on variance estimates, the sonic data streams were artificially degraded in temporal resolution and then used to calculate the three-dimensional variance components. First, the 60- and 30-Hz sonic anemometer data streams were averaged to produce 10-Hz data streams, as previously discussed. The 10-Hz sonic anemometer data streams were further averaged to produce 1-Hz data streams. All three lidar systems used in LATTE collected measurements over a period of one second in order to produce an average Doppler spectrum from which the radial velocity can be derived. Thus, radial velocity measurements from the lidar systems are effectively 1-s averages of the actual radial velocity at each range gate. Next, data points from the averaged 1-Hz sonic data streams were selected to represent the scan times of the individual lidars (e.g., every fourth data point was selected to form a data stream with a temporal resolution of 4 s). These data streams with degraded temporal resolution were then used to calculate the *u*, *v*, and *w* variance on 25 March 2014, as well as the percent error in variance in comparison to the 10-Hz variance values (Fig. 6.17). Temporal

resolutions of 1 s, 4 s, 15 s, and 30 s were selected to represent the time it takes the WindCube to update the wind vector, the time for a full WindCube scan, the time for a full ZephIR scan, and the time for a full Halo six-beam scan, respectively.

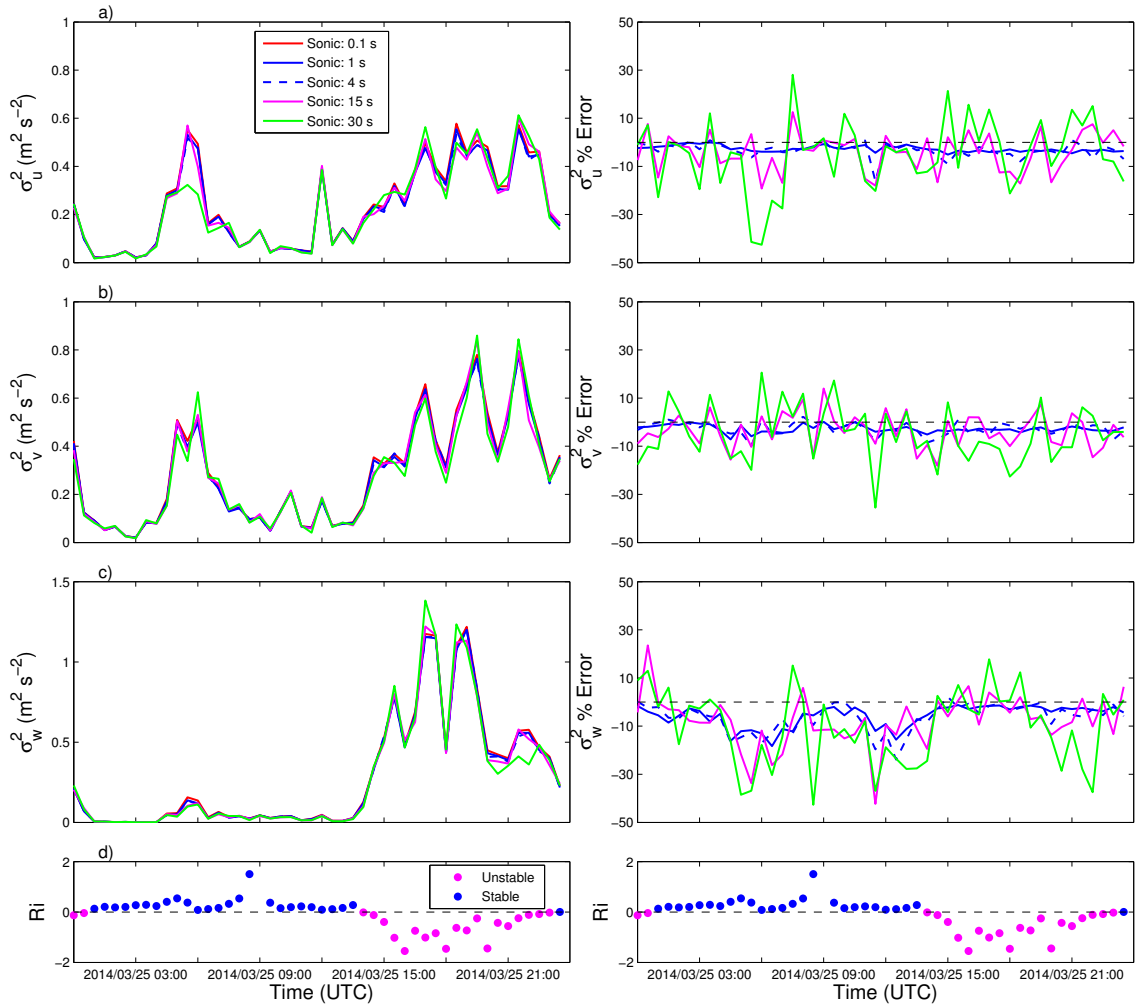

Figure 6.17: Left panel: 30-min a) *u* variance b) *v* variance, and c) *w* variance at 100 m from sonic anemometer data with different temporal resolutions at BAO and d) Richardson number calculated from tower data. Right panel shows percent error in variance (compared to 10 Hz values) obtained by using different temporal resolutions. Data are shown from 25 March 2014.

For the majority of the time series, the variance calculations from the different sonic data streams appear to be quite similar. One exception is the *u* variance at approximately 0600 UTC; while the 1-s and 4-s sonic variance calculations are nearly the same as the variance calculations from the original 10-Hz data stream,

the variance is underestimated by approximately 20% by the 15-s data stream and by nearly 50% by the 30-s data stream (Fig. 6.17a). It is not surprising that this discrepancy occurred during overnight stable conditions, as this is when turbulent motions are expected to occur on much smaller spatial and temporal scales. At times (e.g., approximately 1700 UTC in Fig. 6.17c), the 30-s variance values are higher than the other variance values. These variance overestimates occur because of the random selection of data points that form the 30-s time series. For sampling times of 0.1, 1, 4, 15, and 30 s, the number of data points used to calculate the variance for a 30-min period are 18,000, 1800, 450, 120, and 60, respectively. Thus, significantly fewer data points are available to calculate the variance when the temporal resolution is 30 s. If a single large fluctuation in velocity is selected for the 30-s time series while the remainder of the velocity fluctuations are much smaller, the overall variance will be increased. The distribution of variance values obtained from different selections of data points was also examined. While the variance calculated from the datasets with temporal resolutions of 0.1, 1, and 4 s did not change significantly depending on the selected data points, the variance calculated from the 15- and 30-s time series changed significantly depending on which data points were selected.

In general, the use of either 1-s or 4-s temporal resolution results in percent errors around 5% for u and v and 10% for w. However, the use of either 15-s or 30-s resolution results in large errors in the variance estimates (Fig. 6.17). These

large errors suggest that the scanning strategy and probe volume of the WindCube lidar are likely primarily responsible for the discrepancies between sonic- and lidar-measured variance, not the temporal resolution. However, the 15-s temporal resolution of the ZephIR scans and 30-s temporal resolution of the Halo six-beam strategy could lead to large variance errors, especially under stable conditions, as expected from the calculated integral time scales (Table 6.2) and results of Lenschow et al. (1994).

The sonic data with degraded temporal resolution were also used to investigate the discrepancies between the radial variances measured by the Halo lidar and those calculated from the projected sonic anemometer data (Fig. 6.10). In Fig. 6.18, the radial variances and u and v variances measured by the Halo lidar with the six-beam technique are compared to variances calculated from the 30-s sonic data stream. The circles and error bars indicate the mean and twice the standard deviation of the possible variance values that were calculated when different combinations of sonic data were used to create the 30-s time series. The variance values of the projected sonic radial velocity data differ a fair amount during the late afternoon hours, when several of the Halo beam positions show variance underestimates, but these underestimates are still much lower than the range of variance values calculated from the 30-s sonic anemometer data streams. Thus, it is likely that horizontal heterogeneity and measurement errors due to low wind speeds were primarily responsible for the discrepancies in radial variance values between the Halo and sonic anemometer.

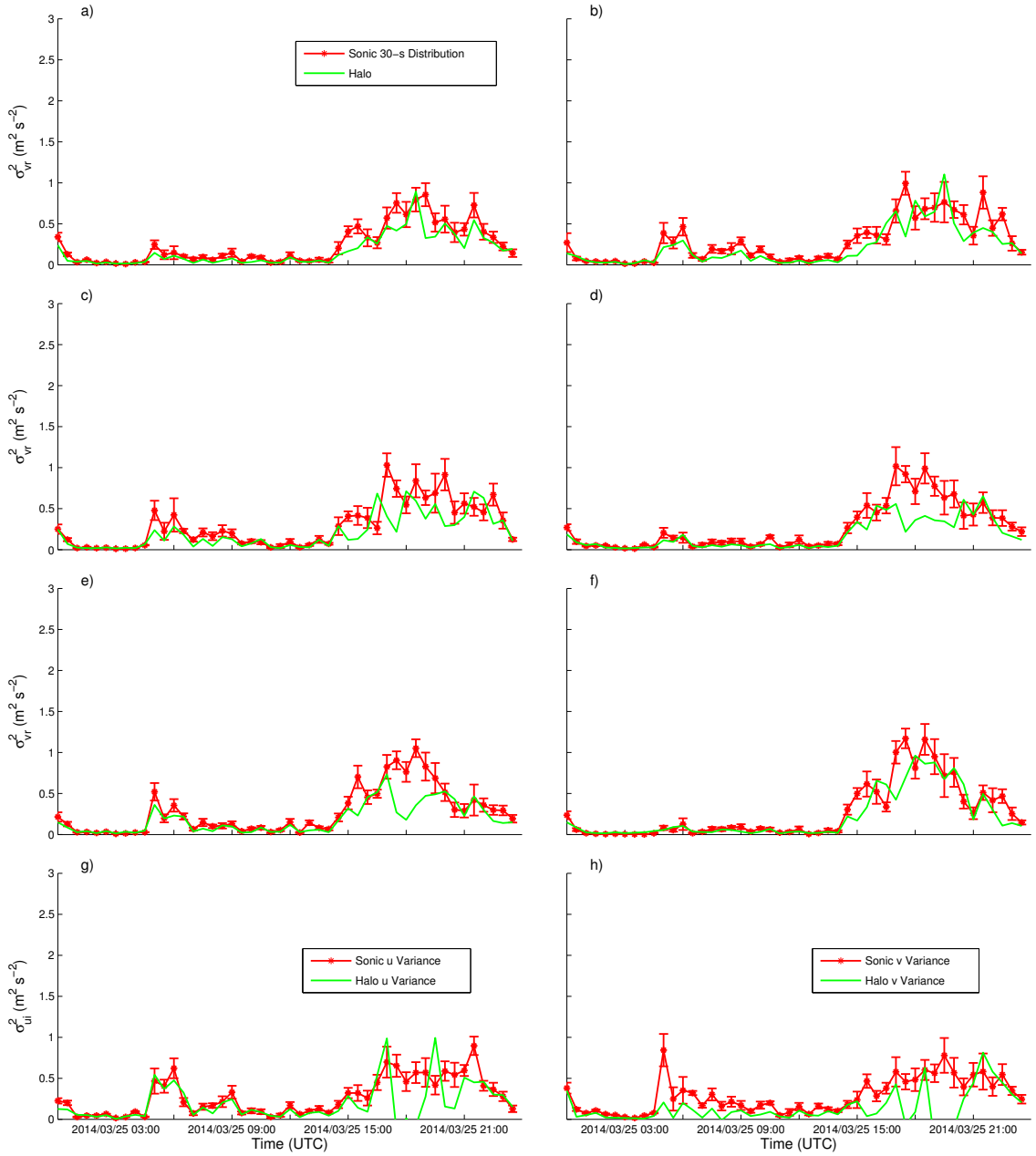

Figure 6.18: As in Fig. 6.10, but variance values are shown for sonic data with 30-s temporal resolution. Circles show mean values from all possible selections of data points to form 30-s data streams and error bars indicate twice the standard deviation.

Similar plots for 6 March 2014 are shown in Fig. 6.19. In comparison to 25 March, the radial variance values measured on 6 March during unstable conditions did not strongly depend on the selected dataset, with most Halo variance estimates from the late afternoon located within two standard deviations of the

mean 30-s sonic values. Thus, the temporal resolution of velocity measurements does not substantially affect variance estimates under higher wind speed conditions. However, other factors, such as volume averaging, will still have an effect on the variance estimates.

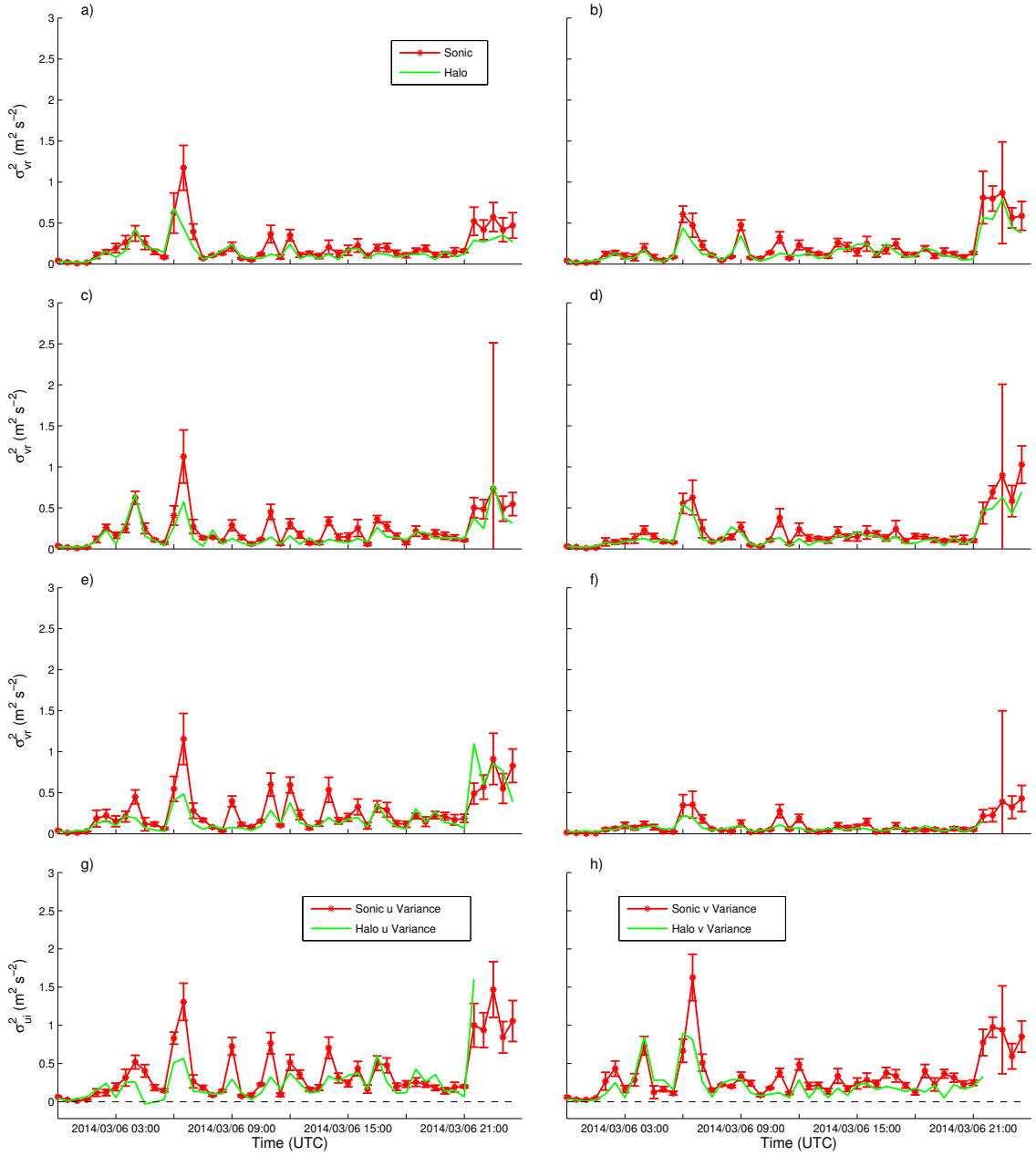

Figure 6.19: As in Fig. 6.12, but variance values are shown for sonic data with 30-s temporal resolution. Circles show mean values from all possible selections of data points to form 30-s data streams and error bars indicate twice the standard deviation.

6.4 Summary and conclusions

The VAD and DBS scanning strategies, along with the six-beam lidar scanning strategy developed by Sathe (2012) were evaluated at two different measurement sites: the Southern Great Plains ARM site and the Boulder Atmospheric Observatory. As a 300-m tower with several sonic anemometers was located at the BAO, the evaluation primarily focused on data collected there. A Halo scanning lidar was deployed at the BAO to test the ability of the six-beam scanning strategy to measure turbulence. In addition, a WindCube pulsed Doppler lidar and a ZephIR continuous wave lidar were deployed at the BAO. These lidars are commercially available and are commonly used in wind energy studies, so the accuracy of their turbulence measurements is of paramount importance to researchers and wind energy developers.

One of the primary disadvantages of using a VAD or DBS technique with a high scanning elevation angle is the vertical velocity contamination that can occur, along with contamination by the other horizontal components. Although using a smaller scanning cone mitigates the effects of horizontal heterogeneity on wind speed estimates, it also increases the contribution of vertical velocity to the radial wind speed estimates. When the vertical velocity field varies across the scanning circle, as is often the case under convective conditions, contributions of the vertical velocity can cause large fluctuations in the horizontal wind speed estimates (e.g., Koscielny et al. 1984; Strauch et al. 1987; Cheong et al. 2008; Wainwright et al. 2014), which, along with variance contamination, leads to overestimates of the u

and v variance (Figs. 6.2, 6.4). Methods for reducing this variance contamination are discussed in Ch. 7.

Horizontal variance estimated from the VAD technique with the Halo lidar was much smaller and more accurate than the estimates from the WindCube and ZephIR lidars, likely because the Halo lidar uses a 45° scanning angle, as opposed to the ≈60° elevation angles used by the other two lidars. For all lidar scanning techniques, the beam should be pointed vertically at least once per scan in order to provide accurate vertical variance estimates, as estimating the vertical variance from a VAD scan typically produces an underestimate (Figs. 6.2, 6.4). Results from this chapter also suggest that a scanning temporal resolution of at least 4 s is needed to accurately measure turbulence under different stability conditions (Fig. 6.17).

The six-beam technique developed by Sathe (2012) did not provide any significant advantages over a normal VAD or DBS scan in this work, with the exception of the measurement of vertical variance by a vertically pointing beam. In fact, the calculation of the u and v variance with the six-beam equations often led to variance underestimates and even negative u and v variance values (Fig. 6.6). The technique appears to be strongly affected by inaccurate variance measurements from one or more beam positions, which could be due to horizontal heterogeneity across the scanning circle and low wind speeds. Future work should use identical lidars with similar scanning elevation angles to estimate the reduction of variance contamination that is obtained through the use of the six-beam technique.

This study demonstrated that several factors affect lidar variance estimates, and that verification data from sonic anemometers is invaluable in assessing the accuracy of lidar turbulence measurements. One of the most important factors affecting turbulence is the scanning elevation angle of the lidar, which cannot be changed on commercially available lidars. Future work could involve the use of scanning lidars and/or lidar models to explicitly examine the effect of scanning elevation angle on horizontal variance estimates. An optimal elevation angle could then be used in the design of future commercially available lidars.

Chapter 7

Variance correction techniques

The largest discrepancies between sonic-measured variance and variance measured by a WindCube lidar appear to occur under unstable conditions. These discrepancies can be largely attributed to two factors that are inherent to the DBS technique: 1) variance contamination caused by combining measurements from different beam locations and 2) contributions of the vertical velocity to the horizontal variance components caused by the violation of the horizontal homogeneity assumption across the lidar scanning circle, as discussed in Ch. 6. In this chapter, two methods are proposed and evaluated for improving WindCube-measured variance under unstable conditions.

First, similarity theory is used to relate the ratio of variance components to the gradient Richardson number such that the values of the u and v variance can be estimated by obtaining an accurate measurement of the w variance from the WindCube lidar. Next, Taylor's frozen turbulence hypothesis is used with data from the vertical beam to estimate the value of the w velocity at opposite sides of the lidar scanning circle. Although a training dataset with sonic anemometers is needed for the development of the techniques, both techniques are designed to be implemented with a single lidar. The fact that the correction methods can be

used without data from sonic anemometers is significant, as most operational wind farms do not have towers with sonic anemometers and lidars are often deployed in sites without any meteorological towers.

7.1 Similarity theory

The similarity theory method relies on the fact that the measurements from the WindCube's vertical beam are not affected by horizontal heterogeneity or variance contamination. Although the beam is only pointed vertically every four seconds, variance calculated from the vertical beam data is quite accurate as compared to a sonic anemometer ($R^2 = 0.96$ for unstable conditions; Table 6.1). If stability information is available in addition to accurate vertical variance estimates, similarity theory can be used to estimate values of the u and v variance.

In this section, data from 50, 60 and 100 m AGL are used and the assumption is made that these heights are located within the surface layer under convective conditions. This assumption is based on the fact that typical convective boundary layer heights are approximately 1 km while the surface layer height is $\approx 10\%$ of the boundary layer height (Stull 1988) and that surface-layer similarity theory is usually valid under unstable conditions (e.g., Hicks 1976; Holtslag 1984; Newman and Klein 2014).

7.1.1 Background

According to Monin-Obukhov similarity theory (Monin and Obukhov 1954), the velocity variances normalized by the surface-layer velocity scale, the friction velocity u_*, should be universal functions of z/L. This leads to the following set of equations:

$$\left(\frac{\sigma_u^2}{u_*^2}\right) = \phi_{11}(\zeta), \tag{7.1}$$

$$\left(\frac{\sigma_v^2}{u_*^2}\right) = \phi_{22}(\zeta), \tag{7.2}$$

$$\left(\frac{\sigma_w^2}{u_*^2}\right) = \phi_{33}(\zeta), \tag{7.3}$$

where $\zeta = z/L$.

In the near-neutral surface layer, the variance ratios follow approximately constant values (Panofsky and Dutton 1984):

$$\frac{\sigma_u}{u_*} \approx 2.4, \tag{7.4}$$

$$\frac{\sigma_v}{u_*} \approx 1.9, \tag{7.5}$$

$$\frac{\sigma_w}{u_*} \approx 1.3. \tag{7.6}$$

However, the similarity theory functions in the stratified surface layer take more complex forms. While the similarity theory functions for heat and momentum, ϕ_h and ϕ_m, are almost universally accepted to follow the forms described by Businger et al. (1971) in the non-neutral surface layer, the variance similarity functions can take drastically different forms with different constants. As the lidar variance correction is needed for unstable conditions, the focus here will be on similarity function fits for convective regimes.

Sorbjan (1989) lists several empirical forms of Eqs. 7.1-7.3 in his Table 4.2. In the free convection regime, ϕ_{11}, ϕ_{22}, and ϕ_{33} are expected to be proportional to $(-\zeta)^{2/3}$ through dimensional analysis. Bradley and Antonia (1979) investigated this relation for data collected during several field campaigns. Based on 4-m data from the 1972 Minnesota surface layer experiment, Bradley and Antonia (1979) found the following relation:

$$\phi_{11}(\zeta) = 62.5(-\zeta)^{2/3}; -2 < \zeta < -0.1. \tag{7.7}$$

Using 5-m data from the International Turbulence Comparison Experiment, conducted in 1976 in New South Wales, Bradley and Antonia (1979) found the following regression line fits for the similarity functions:

$$\phi_{11}(\zeta) = [0.003 + 0.020(-\zeta)^{-2/3}]^{-1}; -2 < \zeta < -0.1. \tag{7.8}$$

$$\phi_{22}(\zeta) = [-0.002 + 0.021(-\zeta)^{-2/3}]^{-1}; -2 < \zeta < -0.1. \tag{7.9}$$

$$\phi_{33}(\zeta) = [0.089 + 0.171(-\zeta)^{-2/3}]^{-1}; -2 < \zeta < -0.1. \tag{7.10}$$

It can also be assumed under convective conditions that σ_u and σ_v scale with the convective velocity scale, w_*, rather than u_*. The following relation between w_* and u_* is given by Panofsky et al. (1977):

$$w_* = \left(\frac{gH_0 z_i}{c_p \rho \theta_0}\right)^{1/3} = u_* k^{-1/3} \left(-\frac{z_i}{L}\right)^{1/3}, \tag{7.11}$$

where z_i is the boundary layer height (m) and all other parameters are as before. Thus, instead of expressing the similarity functions as a function of z/L, they can be expressed as a function of $(-z_i/L)^{1/3}$, which implies that the variance ratios are dependent on the boundary layer height. For 4- and 32-m data from the Minnesota experiment, Panofsky et al. (1977) found that the following function accurately fit observations for ϕ_{11} and ϕ_{22}:

$$\phi_{11}(z_i/L) = \phi_{22}(z_i/L) = (12 - 0.5 z_i/L)^{1/3}; -400 < z_i/L < 0. \tag{7.12}$$

Similarly, Panofsky et al. (1977) found the following relation for ϕ_{33}, but as a function of z/L, not z_i/L:

$$\phi_{33}(z/L) = 1.3(1 - 3z/L)^{1/3}; -7 < \zeta < 0. \tag{7.13}$$

The differences in these similarity function fits suggest that the fits are highly site-dependent. Fortunately, both the BAO and the ARM site have towers instrumented

with sonic anemometers such that site-specific fits can be developed for Eqs. 7.1-7.3.

7.1.2 Application to lidar-measured variance

The similarity theory functions for variance (Eqs. 7.1-7.3) involve normalization by the friction velocity, u_*, the calculation of which requires sonic anemometer measurements of the momentum flux. As most lidars are deployed in locations without sonic anemometer measurements, it is advantageous to have a correction method that can be applied using only data from the lidar.

The friction velocity can be eliminated by taking the ratio of Eq. 7.1 to Eq. 7.3. This new function represents the ratio of the u variance to the w variance, which should also be a function of z/L or, equivalently, Ri, under unstable conditions (Businger et al. 1971):

$$\frac{\phi_{11}(\zeta)}{\phi_{33}(\zeta)} = \frac{\sigma_u^2}{\sigma_w^2} = \phi_{u,w}^*(Ri) \tag{7.14}$$

and similarly,

$$\frac{\phi_{22}(\zeta)}{\phi_{33}(\zeta)} = \frac{\sigma_v^2}{\sigma_w^2} = \phi_{v,w}^*(Ri). \tag{7.15}$$

Thus, if an accurate value of σ_w^2 can be obtained from the WindCube's vertical beam and the functions $\phi_{u,w}^*(Ri)$ and $\phi_{v,w}^*(Ri)$ are known, along with the value of Ri, the approximate values of σ_u^2 and σ_v^2 can be found through the following equations:

$$\sigma_{u,WC}^2 = \phi_{u,w}^* \sigma_{w,WC}^2. \tag{7.16}$$

$$\sigma_{v,WC}^2 = \phi_{v,w}^* \sigma_{w,WC}^2. \tag{7.17}$$

From Eqs. 7.4-7.6, the approximate neutral values of $\phi_{u,w}^*$ and $\phi_{v,w}^*$ are given by the following equations:

$$\phi_{u,w,n}^* = \frac{\sigma_u^2}{\sigma_w^2} = \frac{(2.4)^2}{(1.3)^2} = 3.4. \tag{7.18}$$

$$\phi_{v,w,n}^* = \frac{\sigma_u^2}{\sigma_w^2} = \frac{(1.9)^2}{(1.3)^2} = 2.1. \tag{7.19}$$

Following the procedure described in Newman and Klein (2014), functions for $\phi_{u,w}^*$ and $\phi_{v,w}^*$ were assumed to have the following general form:

$$\phi^* = a(1 - bRi)^c, \tag{7.20}$$

where b and c are constants found through a least-square fitting function in MATLAB and a was taken as the neutral value of ϕ^* (Eqs. 7.18-7.19). This form of the function was used as it follows the form of the similarity function for momentum used by Businger et al. (1971), which was derived from mixing-length theory (Fleagle and Businger 1980). Although the form in Eq. 7.20 is technically only valid for the similarity functions for mean wind speed and temperature profiles, it is commonly used in the literature to fit the similarity functions for variance as well

(Sorbjan 1989). Equation 7.20 involves multiplying the neutral value of the variance ratios by a stability correction, similar to the equation for the diabatic wind profile (Panofsky and Dutton 1984). Fits to the function are shown in Sect. 7.1.3.

The similarity theory correction method was applied to 60-m WindCube data at the ARM site and 50- and 100-m WindCube data at the BAO. At both locations, functions for $\phi^*_{u,w}$ and $\phi^*_{v,w}$ were found using data for σ^2_u and σ^2_v measured with sonic anemometers at corresponding heights. The values of *Ri* were determined from auxiliary instrumentation on the towers at the different sites. To estimate the horizontal variances $\sigma^2_{u,WC}$ and $\sigma^2_{v,WC}$, 30-min values of *Ri* were then used to calculate the values of the functions $\phi^*_{u,w}$ and $\phi^*_{v,w}$ for each 30-min period and inserted into Eqs. 7.16 and 7.17, along with WindCube measurements of $\sigma^2_{w,WC}$. At each site, 60% of the available sonic data were used to develop the similarity theory fits with the remaining 40% of the data reserved for testing.

7.1.3 Results

7.1.3.1 Boulder Atmospheric Observatory

At the BAO, 50- and 100-m sonic and lidar data were used from 14 February to 26 March 2014 to develop and test fits for the similarity functions with different fits developed for each height. (Wind directions between 225° and 315° were once again excluded to avoid influences from the Rocky Mountains, as discussed in Sect. 3.2.) A cross-validation procedure (e.g., Wilks 2006) was used to estimate the mean and standard deviation of the parameters *b* and *c* for different sets

of randomly selected data, as well as to assess the performance of the correction technique for different sets of data. This procedure was used to ensure that the results of the similarity theory correction technique are not dependent on the dataset used to produce the similarity function fit. The means and standard deviations of the various fit parameters from 100 sets of randomly selected data are shown in Tables 7.1 and 7.2 for the 50- and 100-m fits, respectively. Comparisons between the fitted similarity functions $\phi^*_{u,w}$ and $\phi^*_{v,w}$ and the sonic variance ratios are shown in Figs. 7.1 and 7.2. The similarity functions were only fit for unstable conditions ($Ri \leq 0$), as there was a large amount of scatter in the variance ratios for stable conditions and the variance correction is primarily needed for unstable conditions.

Values of the parameters b and c that were fit to the similarity function (Eq. 7.20) did not vary significantly depending on the dataset used, as evidenced by the small standard deviations in Tables 7.1 and 7.2. One exception is parameter b for the 100-m σ_v^2 fit, which had a standard deviation of 15.93, amounting to over 40% of the mean value of 38.85 (Table 7.2). Thus, the variability between data samples for $\phi^*_{v,w}$ appears to be mainly captured in parameter b. However, the RMSE of the similarity function fits did not change significantly between the training and testing sets, suggesting that the accuracy of the fits is not dependent on the data used to find the fit parameters. The RMSE values for the similarity function fits were generally lower for the 50-m data in comparison to the 100-m data. This may have resulted because 50 m is closer to the surface and variance relations are thus more likely to follow similarity theory.

Training: σ_u^2						
b	**c**	**RMSE**	**Slope: Orig.**	**R^2: Orig.**	**Slope: Corrected**	**R^2: Corrected**
15.78 (5.53)	-0.54 (0.17)	1.68 (0.22)	1.05 (0.03)	0.78 (0.04)	0.80 (0.04)	0.64 (0.05)
Testing: σ_u^2						
-	-	1.71 (0.15)	1.05 (0.02)	0.79 (0.02)	0.80 (0.03)	0.65 (0.03)
Training: σ_v^2						
7.40 (2.19)	-0.19 (0.08)	1.31 (0.09)	1.24 (0.06)	0.68 (0.08)	0.75 (0.05)	0.47 (0.07)
Testing: σ_v^2						
-	-	1.29 (0.05)	1.25 (0.04)	0.69 (0.05)	0.76 (0.03)	0.48 (0.05)

Table 7.1: Results from 100 cross-validation procedures at the BAO from 50-m data, with 60% of available data used for training and 40% of data used for testing. Values for the fit parameters b and c for unstable conditions are shown, along with root mean-squared error (RMSE) of the similarity function fit, the slope and correlation coefficient (R^2) of the regression line for the original WindCube variance compared to the sonic variance, and the slope and correlation coefficient of the regression line for the corrected WindCube variance. Mean values are listed with standard deviations shown in parentheses.

Training: σ_u^2						
b	**c**	**RMSE**	**Slope: Orig.**	**R^2: Orig.**	**Slope: Corrected**	**R^2: Corrected**
17.73 (6.95)	-0.60 (0.22)	2.33 (0.28)	1.12 (0.05)	0.69 (0.05)	0.93 (0.04)	0.67 (0.06)
Testing: σ_u^2						
-	-	2.25 (0.19)	1.12 (0.03)	0.68 (0.03)	0.94 (0.03)	0.68 (0.04)
Training: σ_v^2						
38.85 (15.93)	-0.11 (0.05)	1.39 (0.14)	1.54 (0.10)	0.66 (0.06)	1.05 (0.07)	0.59 (0.05)
Testing: σ_v^2						
-	-	1.38 (0.10)	1.54 (0.07)	0.66 (0.04)	1.06 (0.05)	0.60 (0.03)

Table 7.2: As in Table 7.1, but for 100-m values.

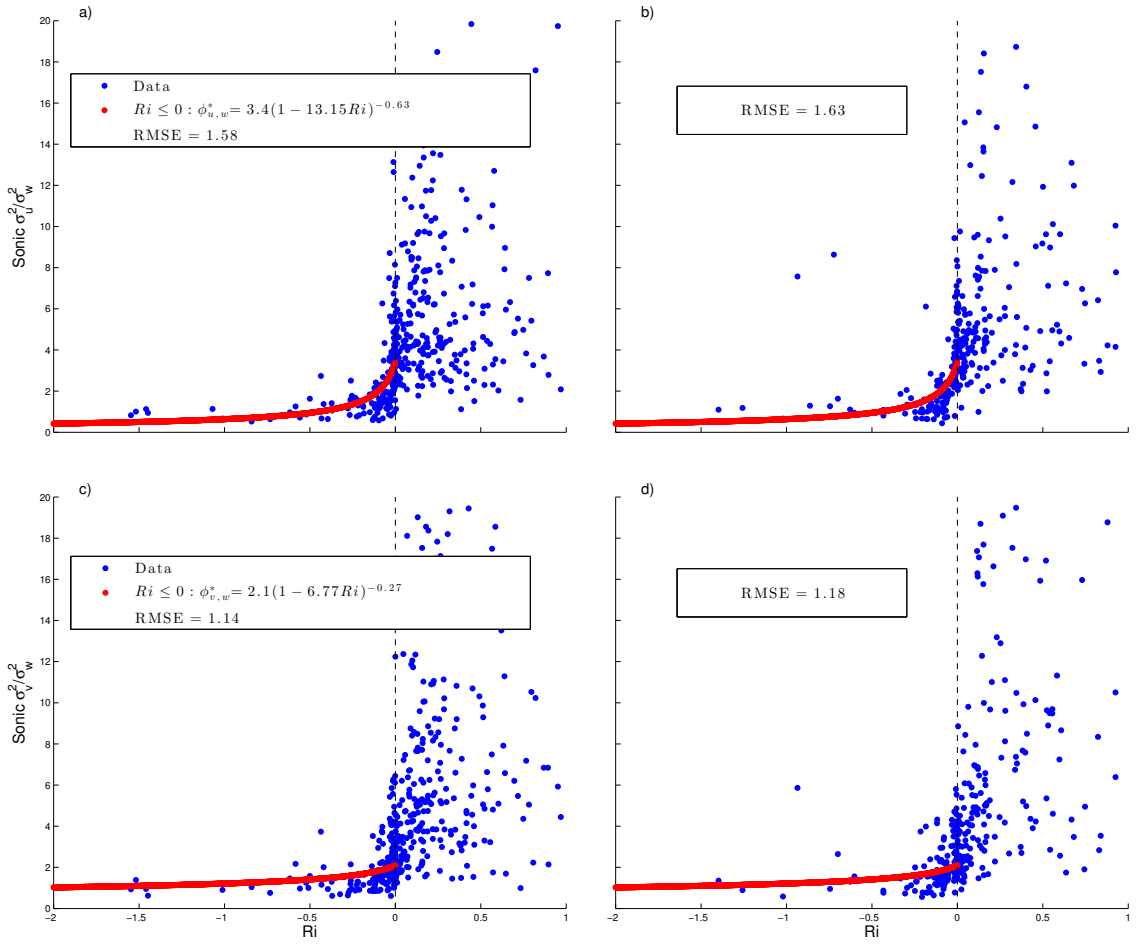

Figure 7.1: Scatter plots of sonic variance ratios at 50 m at BAO as a function of *Ri*. Similarity theory function fits are denoted by red circles with equations and RMSE values listed in figure legends. Results are shown for a) σ_u^2 training set b) σ_u^2 testing set c) σ_v^2 training set and d) σ_v^2 testing set. Dashed vertical line denotes transition from unstable to stable conditions.

For all training and testing sets, the WindCube lidar generally overestimated the variance in comparison to the sonic anemometer (Figs. 7.3, 7.4), with larger overestimates occurring for σ_v^2, as previously observed for variance estimates at the BAO (Sect. 6.2.1) and at other sites (e.g., Sathe et al. 2011). This overestimation is evidenced by the regression line slopes for the original WindCube variance values, which all exceed one (Tables 7.1 and 7.2). Larger overestimation of σ_u^2 and σ_v^2 occurred at 100 m, likely because the effects of volume averaging decrease with height as turbulent scales increase (Sathe et al. 2011). The similarity theory

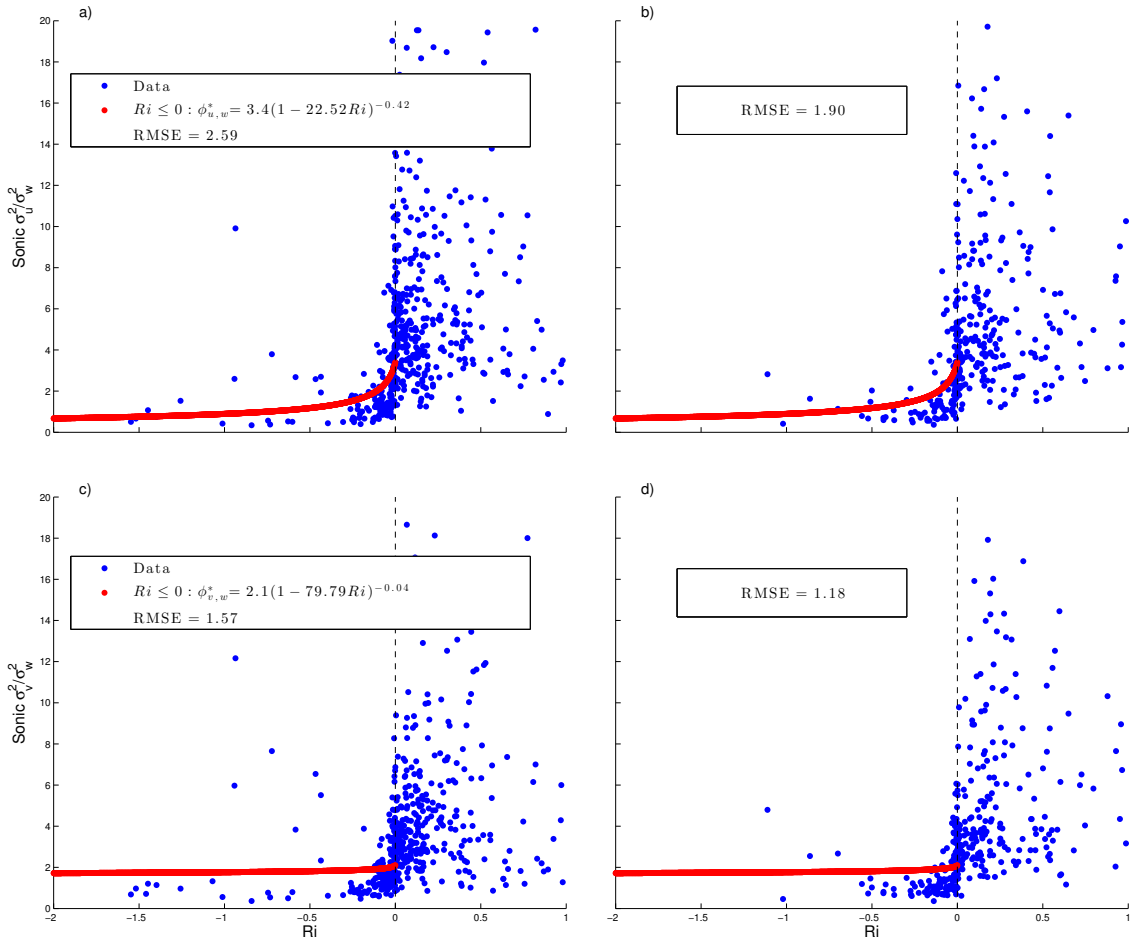

Figure 7.2: As in Fig. 7.1 but for 100-m data.

correction reduced the overestimation of the horizontal velocity variances by the WindCube lidar for both the training and testing datasets, as shown in Figs. 7.3 and 7.4.

7.1.3.2 Atmospheric Radiation Measurement Site

The similarity theory correction technique was also tested on data at the Southern Great Plains ARM site. Data were used from the 60-m sonic anemometer on the tower at the ARM site and from the WindCube v2 lidar from 14 November 2012 to 31 January 2013. (Ideally, the correction technique would be tested on 50-

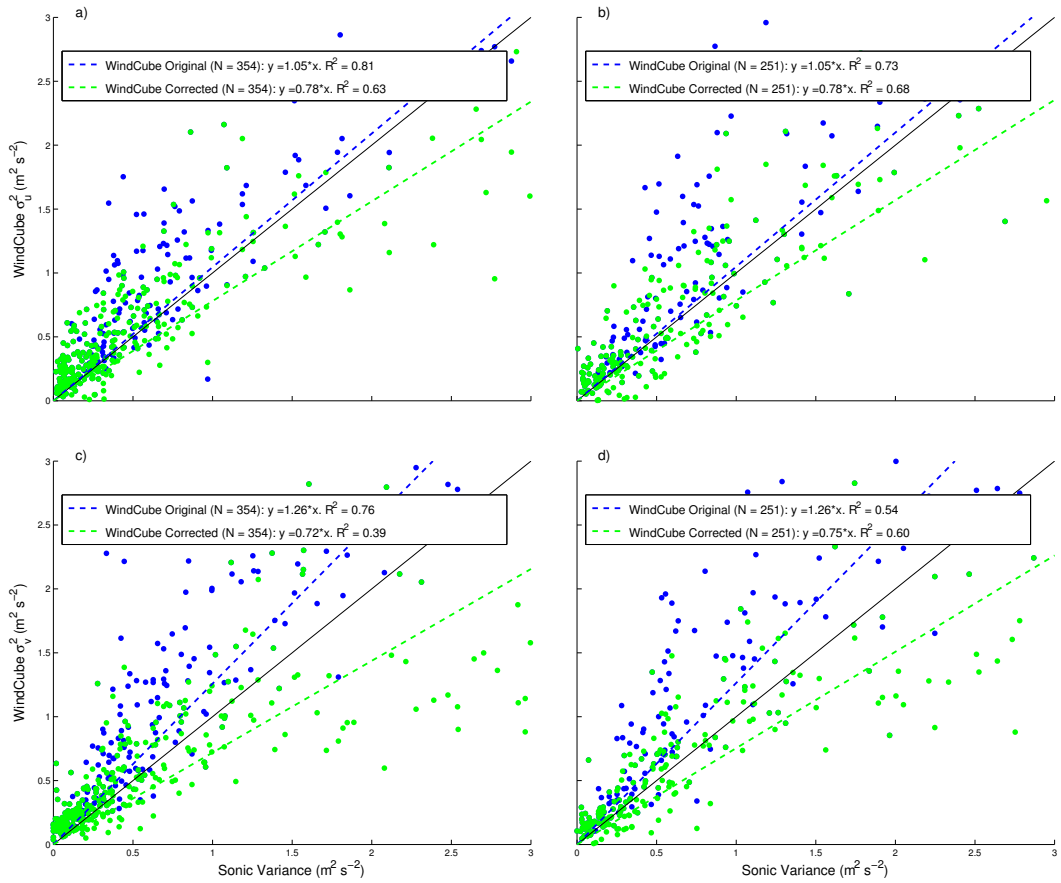

Figure 7.3: Scatter plots of sonic variance versus original and corrected WindCube variance at 50 m at the BAO. Regression fits are denoted by dashed lines with equations and R^2 values shown in figure legends. Results are shown for a) σ_u^2 training set b) σ_u^2 testing set c) σ_v^2 training set and d) σ_v^2 testing set. Black line denotes one-to-one line for reference.

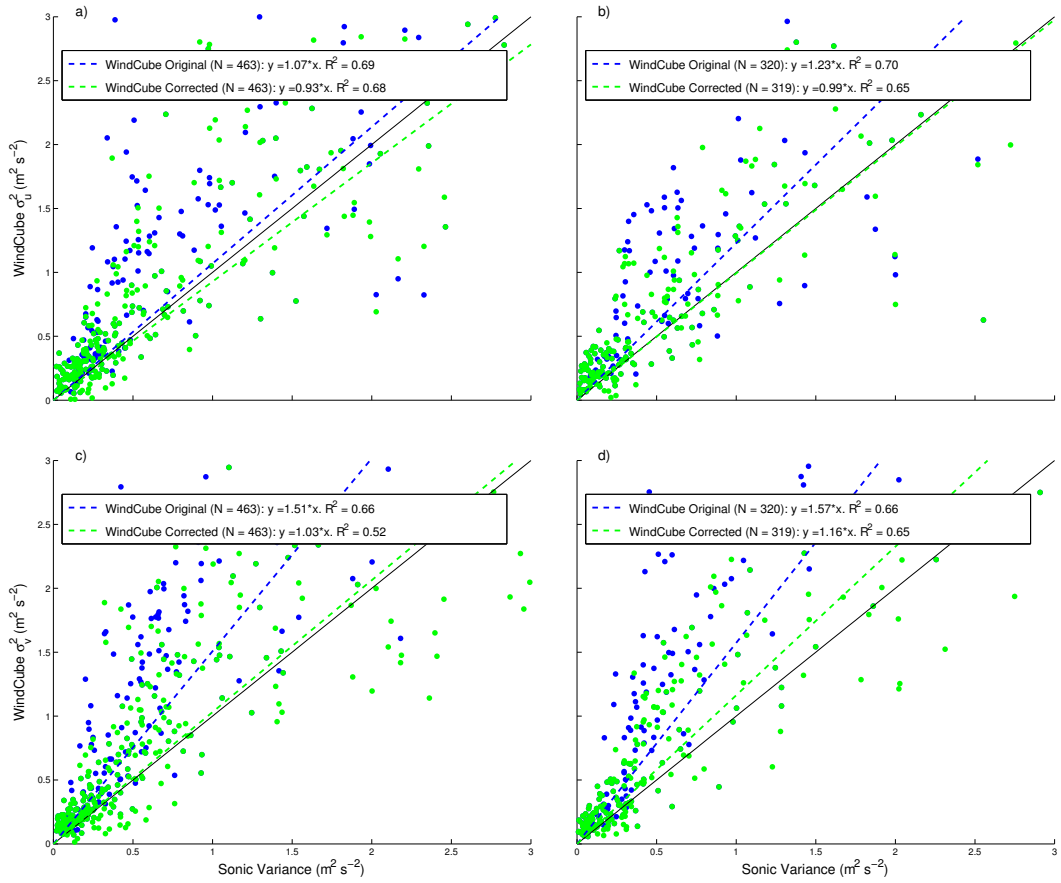

Figure 7.4: As in Fig. 7.3, but for 100-m data.

or 100-m data at the ARM site to match the analysis from the BAO, but sonic data are only available at 4, 25, and 60 m at the ARM site.) Results from the similarity theory correction technique for the ARM site are shown in Table 7.3. A comparison between the fitted similarity functions $\phi^*_{u,w}$ and $\phi^*_{v,w}$ and the sonic variance ratios is shown in Fig. 7.5.

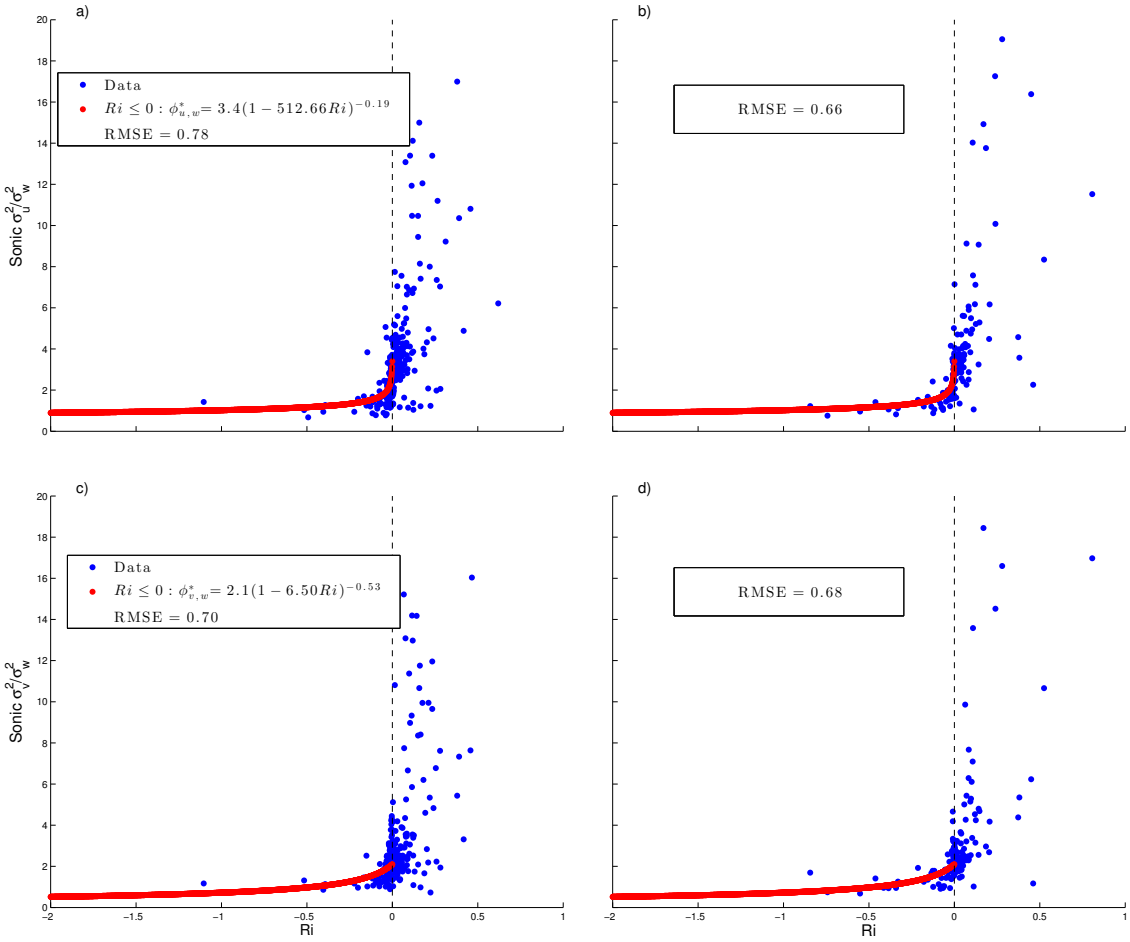

Figure 7.5: As in Fig. 7.1 but for 60-m data at the ARM site.

The mean values of the fit parameters *b* and *c* changed fairly significantly when the similarity theory fit was applied to data from the ARM site, particularly for parameter *b* for the σ_u^2 fit, which had a mean value of 566.72 and a standard deviation of 259.22 (Table 7.3). The values of *Ri* tended to be smaller at the ARM site under

Training: σ_u^2						
b	**c**	**RMSE**	**Slope: Orig.**	**R^2: Orig.**	**Slope: Corrected**	**R^2: Corrected**
566.72 (259.22)	-0.20 (0.03)	0.73 (0.08)	1.10 (0.03)	0.83 (0.02)	0.89 (0.04)	0.72 (0.05)
Testing: σ_u^2						
-	-	0.74 (0.05)	1.09 (0.02)	0.83 (0.01)	0.89 (0.02)	0.72 (0.03)
Training: σ_v^2						
9.78 (3.06)	-0.45 (0.12)	0.69 (0.07)	1.46 (0.02)	0.89 (0.01)	0.93 (0.05)	0.62 (0.06)
Testing: σ_v^2						
-	-	0.69 (0.05)	1.46 (0.02)	0.89 (0.01)	0.93 (0.03)	0.61 (0.04)

Table 7.3: As in Table 7.1, but for 60-m data at the ARM site.

unstable conditions in comparison to the BAO, although values of ϕ^* were similar. The change in fit parameters could be an effect of using different measurement heights to calculate *Ri* at the different sites (4 and 60 m at the ARM site and 10 and 100 m at the BAO) or conditions may have been less strongly convective at the ARM site. It is difficult to make this determination without having similar instrumentation at the same measurement heights at both sites. However, these low values of *Ri* were likely what caused parameter b to be so large for the σ_u^2 fit at the ARM site. As the value of *Ri* decreases, the value of b will have to increase to match similar values for $\phi_{u,w}^*$. Thus, the method is strongly affected by the values of *Ri* measured at a site. Ideally, if the training dataset is long enough, a significant range of *Ri* values can be measured such that the fit is not strongly site-dependent. RMSE values for the similarity theory fit decreased for the ARM site, although this could be caused by the smaller data set available at the ARM site (N = 682 and 783 for the 50- and 100-m data at the BAO, respectively, and N = 468 for the 60-m data at the ARM site).

Similar to the BAO, the WindCube lidar often overestimated the u and v variance, with larger overestimates occurring for the v variance (Fig. 7.6). Slopes of the WindCube variance regression lines were between those of the 50- and 100-m BAO data (Tables 7.1-7.3). This further confirms the finding that WindCube variance overestimation generally increases with height as scales of turbulence increase and the effects of volume averaging decrease (Sathe et al. 2011). At

the ARM site, the similarity theory correction method also decreased WindCube-estimated variance significantly, with regression slopes becoming less than one after the correction was applied.

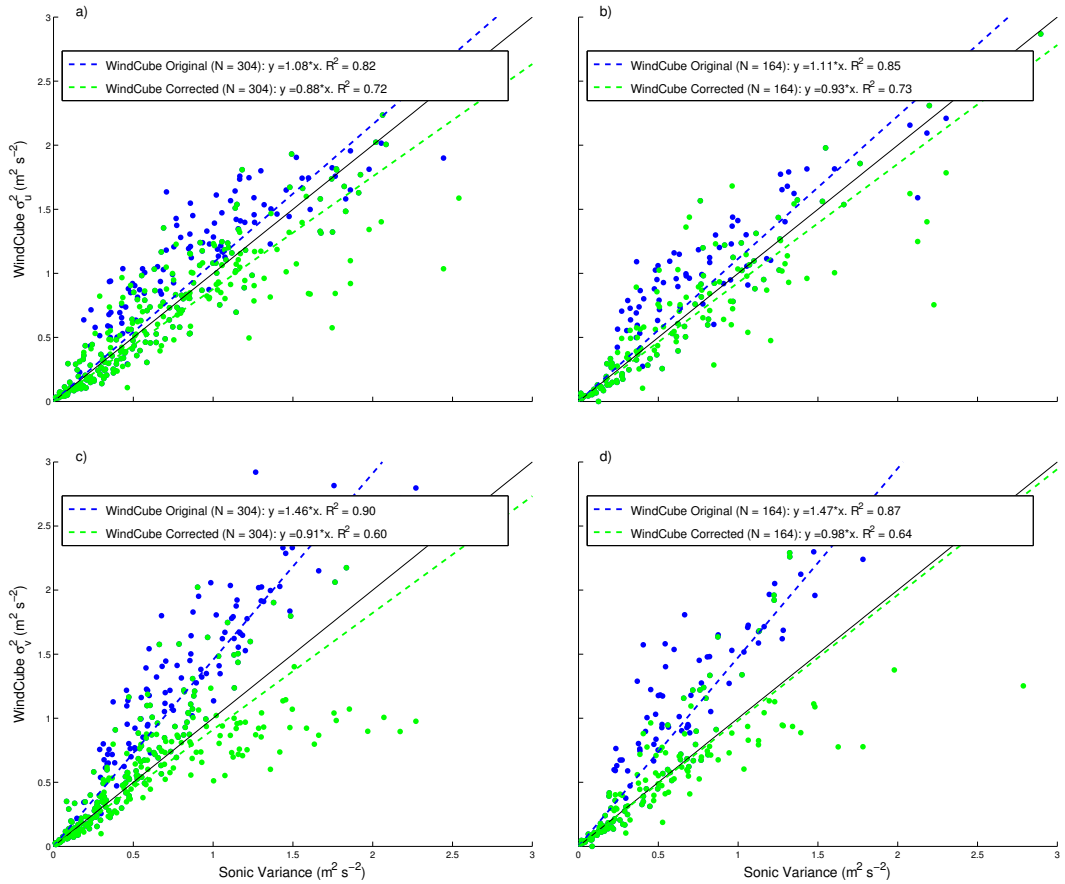

Figure 7.6: As in Fig. 7.3, but for 60-m data at the ARM site.

7.1.3.3 Conclusions

In summary, the similarity theory method reduced WindCube overestimates of the *u* and *v* variance at both the BAO and the ARM site and brought them closer to the sonic anemometer measurements. This variance reduction is evident in the variance time series plots shown in Fig. 7.7, which is identical to Fig. 6.2 except for the application of the similarity theory correction method. The corrected $\sigma^2_{u,WC}$

and $\sigma^2_{v,WC}$ values are much closer to the sonic-measured values under unstable conditions. Under stable conditions, the correction was not applied and the corrected and original WindCube variance values are the same. The correction was not needed under these conditions, as the original WindCube variance values were already close to those measured by the sonic anemometer.

The similarity functions were different at the two different sites, suggesting that the similarity theory fit could be site-dependent, although this difference is also likely due to the different heights (and possibly different seasons) used at the different sites. In the future, variance ratios from similar instruments at similar heights should be compared for different sites to investigate the site dependence of the similarity theory fit. Planned work with the BAO dataset will include evaluation of the similarity theory correction method at additional heights to investigate the height dependence of variance overestimation and the similarity function.

7.1.4 Application to wind energy

The turbulence quantity typically used in the wind energy field is the turbulence intensity (TI), defined as the ratio between the wind speed standard deviation and the mean wind speed over a particular time period. The IEC classifies wind turbines into several categories depending on the inflow conditions under which the turbine can perform at a wind farm site. Classes are largely divided by the maximum expected 50-year wind gust at hub height and the expected value of the TI when the

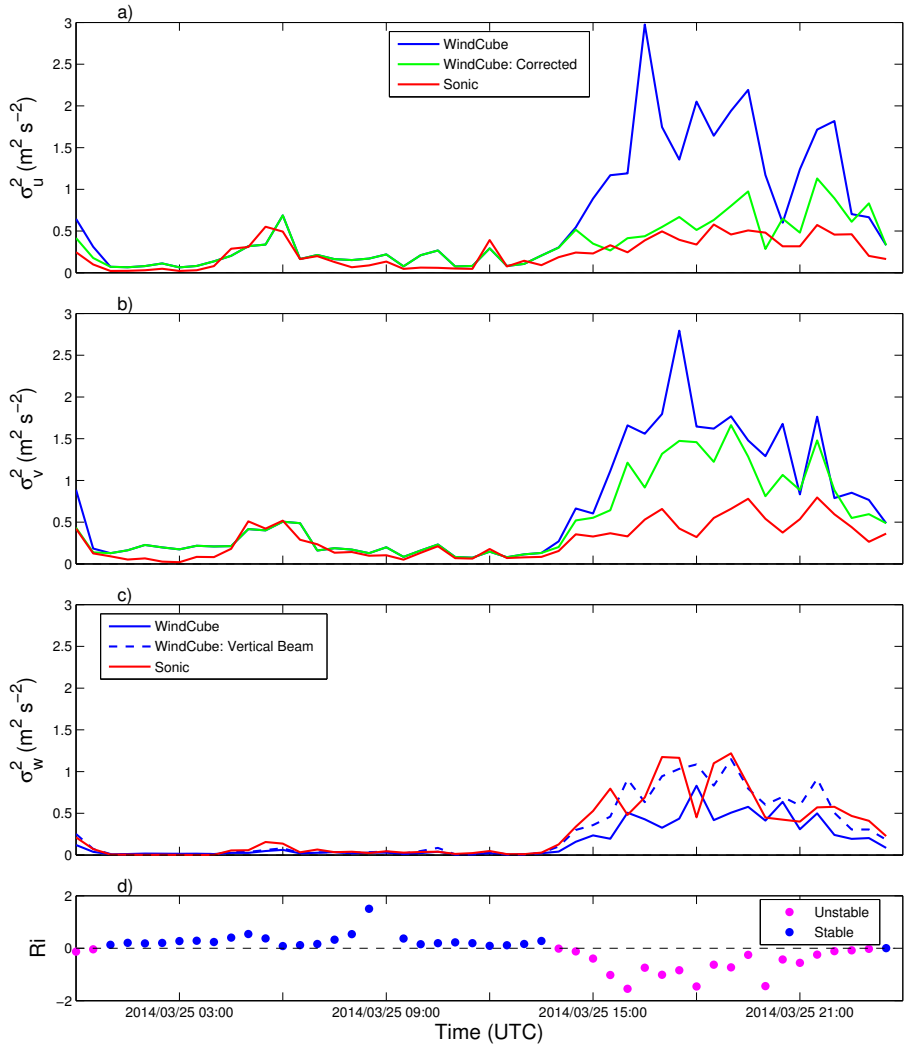

Figure 7.7: 30-min a) *u* variance b) *v* variance, and c) *w* variance at 100 m from sonic anemometers, WindCube DBS technique, and corrected WindCube measurements at BAO and d) Richardson number calculated from tower data. Data are shown from 25 March 2014. In c), solid blue line indicates DBS-calculated *w* variance and dashed blue line indicates *w* variance calculated from vertically pointing beam.

mean wind speed is 15 m s^{-1}, referred to as I_{ref} (International Electrotechnical Commission 2005a).

Wind speed and turbulence should be measured by a cup anemometer for wind power performance tests according to IEC standards (International Electrotechnical Commission 2005b). Cup anemometers only measure the horizontal wind

speed and are not capable of separating wind speed standard deviations into different components. Thus, the TI calculation used for site classification is the ratio of the standard deviation of the horizontal wind speed to the mean horizontal wind speed (International Electrotechnical Commission 2005b). In order to match the horizontal TI typically used in wind energy, the following equation was applied to the WindCube and sonic anemometer data, as in Wharton and Lundquist (2012a):

$$TI = \frac{\sqrt{\sigma_u^2 + \sigma_v^2}}{\overline{u}}, \tag{7.21}$$

where σ_u^2 and σ_v^2 are the 10-min variance values (m^2 s^{-2}) and $\overline{u}$ is the 10-min mean horizontal wind speed (m s^{-1}).

In addition to the 30-min variance values, the similarity theory correction method was applied to the 10-min WindCube variance values at the BAO, as the standard averaging time in wind energy is 10 min. These corrected variance values were then used in Eq. 7.21 to estimate the difference in horizontal TI obtained through the similarity theory correction. Results from 100 cross-validation procedures are summarized in Table 7.4 and sample scatter plots are shown in Fig. 7.8. In order to avoid large TI values that were caused by low wind speeds, TI values where the mean wind speed was lower than 5 m s^{-1} were excluded.

The similarity theory correction decreased WindCube estimates of TI and brought them closer to the sonic estimates, although there was more scatter about the regression line than for the variance corrections (see lower R^2 values in Table 7.4 and larger scatter in Fig. 7.8). However, differences of 2% in TI are used to

Training: TI			
Slope: Orig.	**R^2: Orig.**	**Slope: Corrected**	**R^2: Corrected**
1.09 (0.02)	0.51 (0.05)	0.99 (0.02)	0.43 (0.05)
Testing: TI			
1.09 (0.03)	0.51 (0.08)	1.01 (0.03)	0.44 (0.08)

Table 7.4: Results from 100 cross-validation procedures at the BAO, with 60% of available data used for training and 40% of data used for testing. Values for the slope and correlation coefficient (R^2) of the regression line for the original WindCube TI compared to the sonic TI, and the slope and correlation coefficient of the regression line for the corrected WindCube TI are shown. Mean values are listed with standard deviations shown in parentheses.

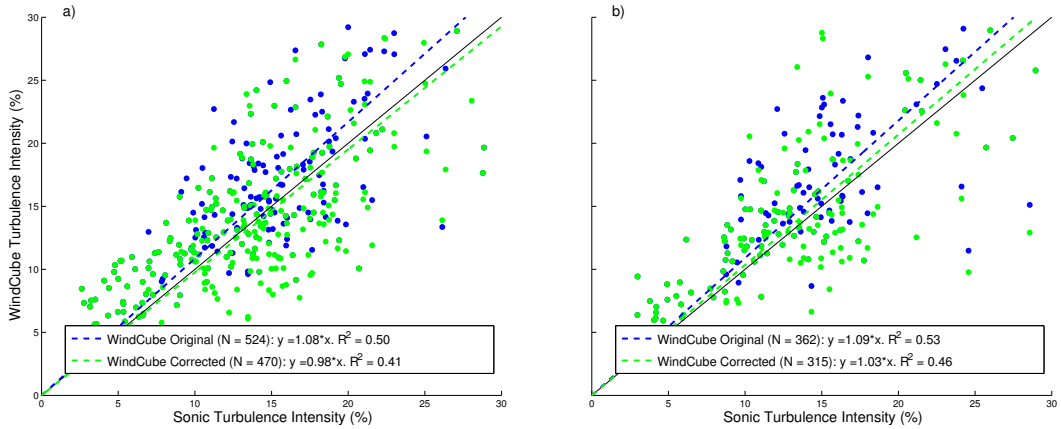

Figure 7.8: Scatter plots of sonic TI versus original and corrected WindCube TI at the BAO. Regression fits are denoted by dashed lines with equations and R^2 values shown in figure legends. Results are shown for a) training set and b) testing set. Black line denotes one-to-one line for reference.

separate wind turbines into different classes, such that even the small reduction in regression slope shown in Table 7.4 would have a significant effect on turbine classification. Very few valid TI values were associated with mean wind speeds of 15 m s^{-1}, as most high wind speeds in the dataset were associated with westerly winds coming from the direction of the Rocky Mountains, which were excluded from the analysis. Thus, the dataset was not large enough to calculate I_{ref}, which is the quantity that is actually used in the turbine classification process.

7.2 Applying Taylor's frozen turbulence hypothesis

In the DBS technique used by the WindCube lidar, it is assumed that flow is horizontally homogeneous across the scanning circle. However, as discussed in Sect. 2.4.2.3, this assumption is often violated, which can induce errors in the variance estimates. The violation of the horizontal homogeneity assumption may have caused large errors in the WindCube-estimated u and v variance values at the BAO as a result of the contribution of vertical velocity to the horizontal velocity components (Sect. 6.2.1.1). The correction method discussed in this section uses velocity values measured by the WindCube's vertical beam to estimate the values of w at either side of the scanning circle and in turn, reduce the contribution of w to the horizontal velocity components.

As discussed in Sect. 2.4.2.1, the WindCube lidar scans include a vertical beam position to provide a direct measure of the vertical velocity at the center of the scanning circle. By applying Taylor's frozen turbulence hypothesis, these vertical beam values can be moved forward and backward in time to times that correspond to the distance that a turbulent eddy would have moved from the center of the scanning circle to a different position along the perimeter of the scanning circle. For a northerly mean wind, the method involves modifying the following equations, which describe the radial wind speeds measured by the north and south beams of a lidar:

$$v_{rN} = v\cos(\phi) + w\sin(\phi), \tag{7.22}$$

$$v_{rS} = -v\cos(\phi) + w\sin(\phi). \tag{7.23}$$

If v and w, the instantaneous meridional and vertical wind speeds, are the same for both the north and south beams, the w terms cancel out when Eqs. 7.22 and 7.23 are combined to calculate the DBS-estimated v, as in Eq. 2.29. However, if different values of w are assumed for both the north and south beams (w_N and w_S, respectively), then the following equation for the lidar-estimated v is produced:

$$v = \frac{v_{rN} - v_{rS} - (w_N - w_S)\sin(\phi)}{2\cos(\phi)}, \tag{7.24}$$

where, for a northerly wind,

$$w_N(t) = v_{rz}(t + \Delta t), \tag{7.25}$$

$$w_S(t) = v_{rz}(t - \Delta t), \tag{7.26}$$

and

$$\Delta t = \frac{\Delta x}{\overline{u}}, \tag{7.27}$$

where v_{rz} is the radial velocity measured by the vertical beam (m s^{-1}), Δx is the distance from the center to the outer edge of the lidar scanning circle (m), and $\overline{u}$ is the 30-min mean wind speed (m s^{-1}). A schematic of the method is shown in Fig. 7.9.

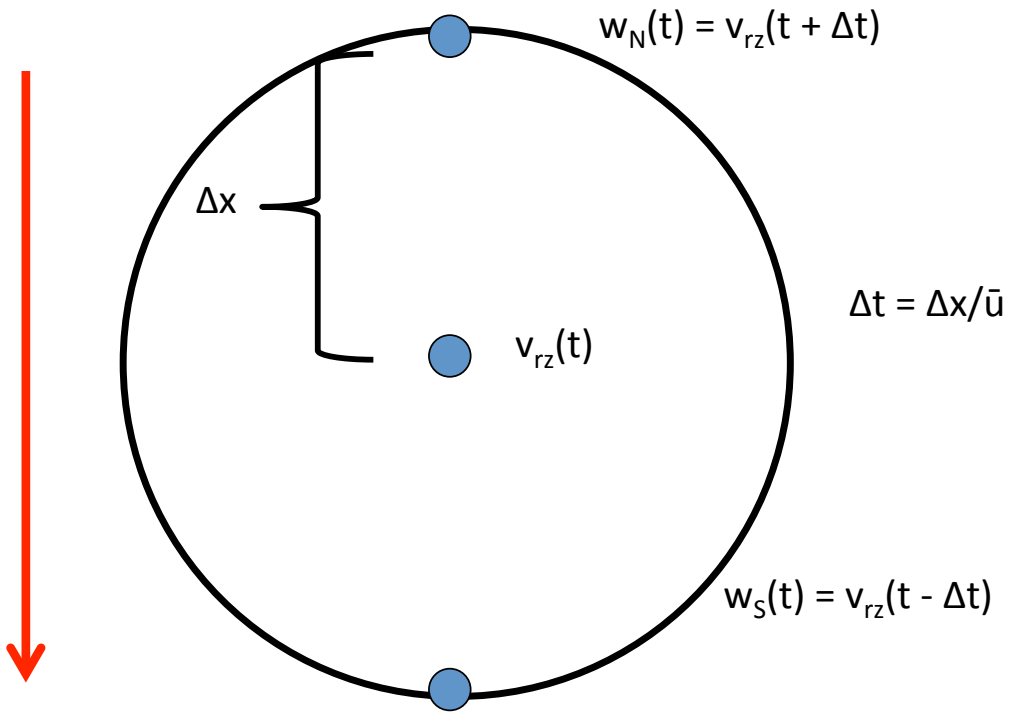

Figure 7.9: Schematic depicting the application of Taylor's frozen turbulence hypothesis to vertical velocity data from WindCube lidar. Red arrow depicts direction of mean wind.

7.2.1 Results

This new method of calculating v from the DBS technique was evaluated using WindCube data from 1330 to 2330 UTC on 22 March 2014. Winds were nearly constantly from the north during the afternoon on 22 March (Fig. 6.1e) such that eddies would primarily travel from the north to the south side of the WindCube scanning circle. The presence of northerly winds simplifies the evaluation of Eq. 7.24, as it can be assumed that eddies were only moving in the north-south direction, not the east-west direction.

Using information from the WindCube vertical beam along with the 30-min mean wind speed and Taylor's frozen turbulence hypothesis, values of w_N and w_S were estimated for each full WindCube scan on 22 March 2014. These values were then used in Eq. 7.24 to calculate a new "corrected" time series of v. Variance calculated from this v time series was compared to variance calculated from the normal DBS v time series (estimated using Eq. 2.29) and variance from the sonic anemometers (Fig. 7.10). The v variance calculated from the corrected DBS time series is nearly always smaller than the original v variance, although both estimates of the v variance from the WindCube lidar are overestimates in comparison to the sonic variance. Throughout most of the time series, the DBS correction reduced the WindCube v variance by approximately 20-40%, with many of the largest reductions in variance occurring at times when the wind direction was close to northerly (Fig. 7.10) and the north-south movement of turbulent eddies was most prominent. These results suggest that assuming horizontal homogeneity in the w component across the scanning circle can increase the horizontal variance estimates by up to 40%. However, some improvement in variance estimates can be made by including a vertical beam position and using vertical velocity data from this beam position to estimate w at different points along the scanning circle.

The technique was also applied to data from the afternoon of 24 March 2014, when winds were primarily from the east and southeast (Fig. 6.1e). Results for the correction method are shown in Fig. 7.11. When winds were from the northeast at the beginning of the time series, corrected variance values were nearly the same

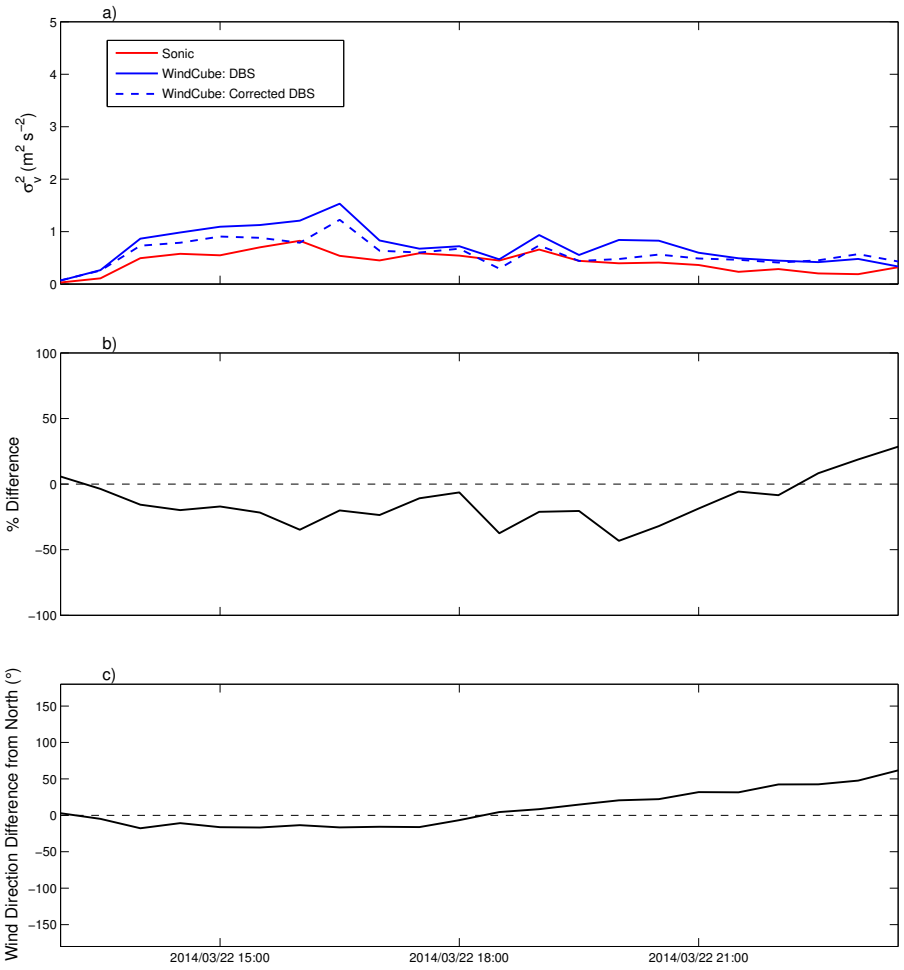

Figure 7.10: a) Time series of 30-min v variance from sonics and different WindCube measurement techniques b) percent difference in variance obtained by applying DBS correction to WindCube data and c) wind direction difference from 0° (north) at 100 m on the afternoon of 22 March 2014 at the BAO.

as the original variance values. As the wind direction shifted from northeasterly to southeasterly from 1500 to 2330 UTC, the correction method began to produce larger variance values than the original WindCube variance values, likely because turbulent eddies were moving from the south to the north of the scanning circle, which is opposite of what was assumed in the correction method. To test this hypothesis, the correction method was applied again to data from 24 March 2014, but with the assumption that turbulent eddies were traveling from south to north

(Fig. 7.12). Although the correction method still overestimates the variance for this dataset, the performance of the correction method is much better when the southerly wind assumption is made, particularly toward the end of the time series when the wind has shifted closer to the southerly direction. This suggests that if the directional dependence of the mean wind is taken into account for the movement of turbulent eddies, Taylor's frozen turbulence hypothesis can be used to correct WindCube variance values under heterogeneous conditions.

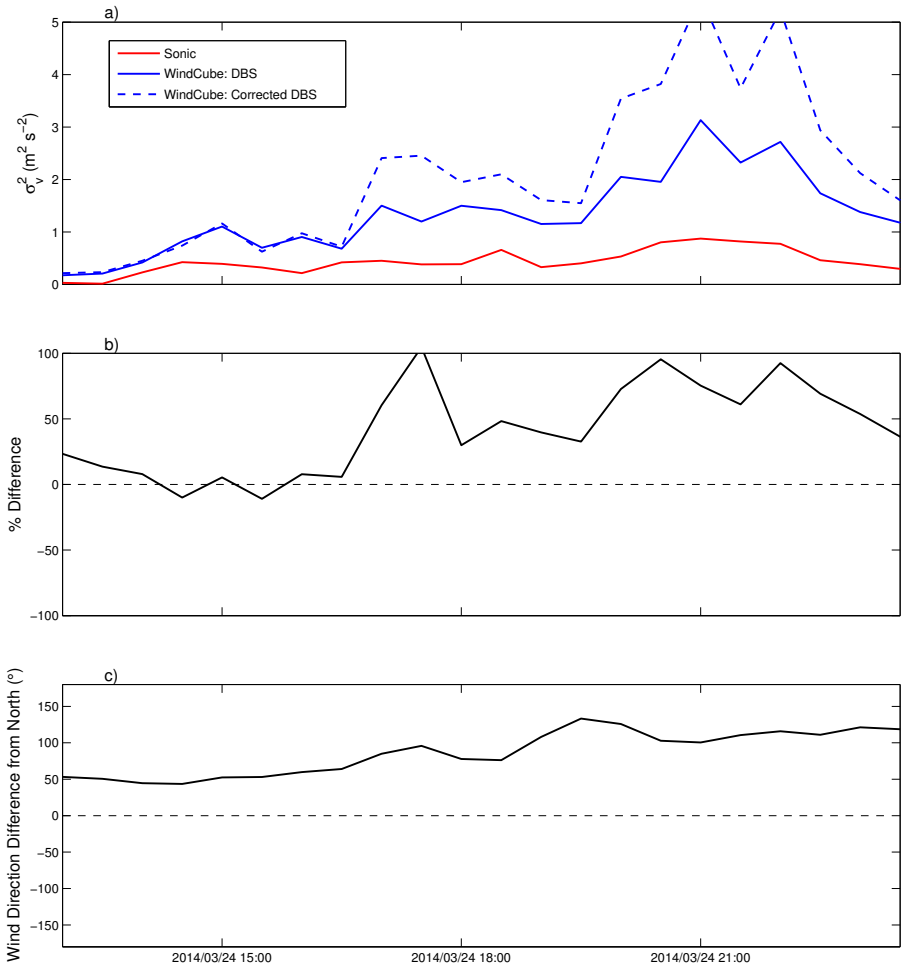

Figure 7.11: As in Fig. 7.10, but for 24 March 2014.

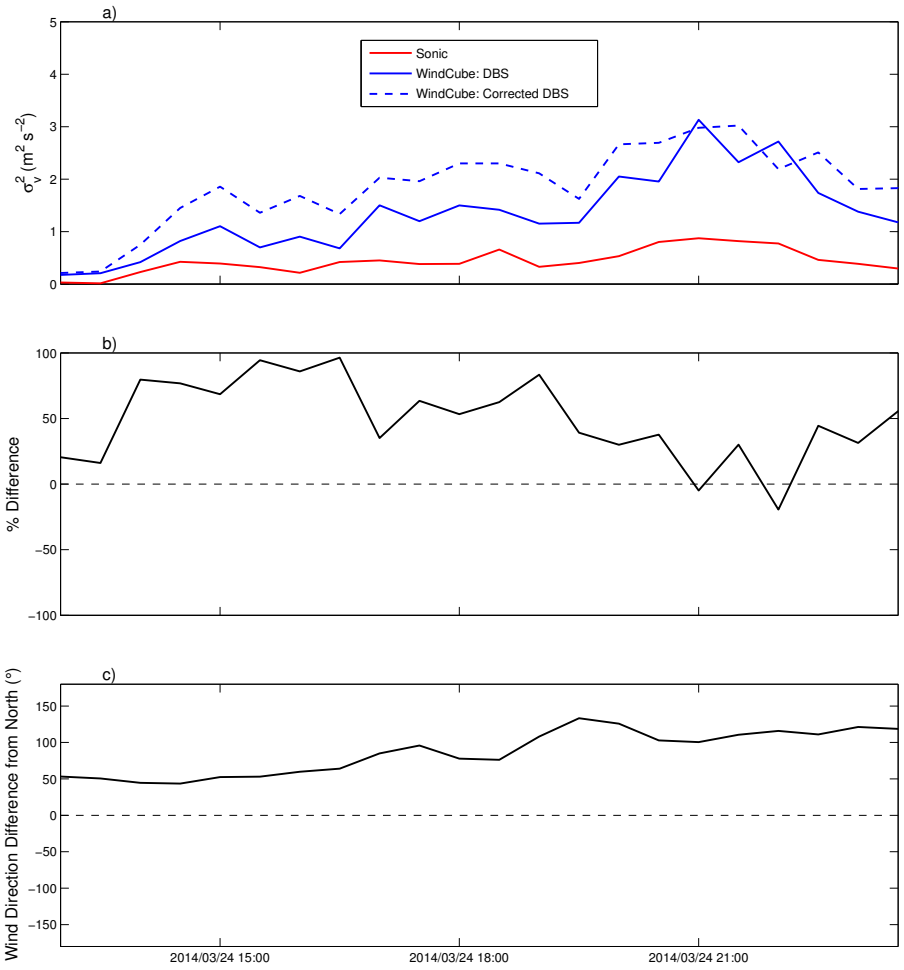

Figure 7.12: As in Fig. 7.11, but with the assumption that turbulent eddies are moving from south to north.

7.2.2 Conclusions

To the author's knowledge, this is the first time that Taylor's frozen turbulence hypothesis has been used to correct horizontal variance estimates with lidar data. Taylor's frozen turbulence hypothesis has previously been validated for large eddies using a scanning lidar (Schlipf et al. 2010), and the method presented here shows promise for providing more accurate horizontal variance estimates from the commonly used DBS scan. The frozen turbulence method should be first verified with in-situ measurements of w at distances spanning a lidar scanning circle, either

from a network of meteorological towers or from a numerical weather prediction model. Future work will likely include running a large-eddy simulation (LES) model for the ARM site to test the ability of this method to estimate values of the vertical velocity at different points in space.

Chapter 8

Summary and conclusions

Turbulence is an important parameter for wind power production, site selection, and turbine design. Traditionally, turbulence was measured by cup anemometers on towers. However, as wind energy expands and modern hub heights increase, it has become more and more difficult to install tall towers at potential wind farm sites. In addition, interest in offshore wind energy is growing and there is a need for turbulence measurements at offshore locations, where it is even more difficult and costly to install tall towers. In response to these issues, researchers and wind energy developers have begun using lidars to measure wind speeds and turbulence for wind energy studies. However, several factors cause discrepancies between lidar-measured and cup or sonic anemometer-measured turbulence, including horizontal heterogeneity across the scanning circle and variance contamination that results from the combination of data from different lidar beam positions. This dissertation aimed to examine different ways to use lidars to accurately measure turbulence. Data from two field campaigns were used to answer the research questions posed in Ch. 1, and responses to the questions are summarized in the next section.

8.1 Research questions

What additional turbulence information can be obtained from multi-lidar scanning strategies that is not available from a vertically profiling lidar? A multi-lidar scanning campaign was conducted at the ARM site in northern Oklahoma to test the ability of the tri-Doppler technique (Sect. 2.4.3.2) and the virtual tower technique (Sect. 2.4.3.3) to measure mean wind speeds and turbulence. These techniques had been evaluated before, but extensive studies to determine their ability to measure turbulence had not yet been conducted. Measurements from these techniques were also compared to measurements from a WindCube vertically profiling lidar, which uses a standard DBS technique.

The tri-Doppler technique can accurately measure mean wind speed and direction profiles by combining line-of-sight velocity data from two of the scanning lidars. The technique can also measure high-frequency turbulence at one analysis height without the use of a scanning circle. Results indicated that the tri-Doppler technique measured higher crosswise variance values than the WindCube lidar under stable conditions, when turbulence scales are small. In addition, a spectral analysis suggested that the tri-Doppler technique reduced variance contamination under unstable conditions, which affects lidars that use the DBS and VAD techniques. As commercial lidar variance estimates are generally most inaccurate under unstable conditions (Ch. 6), the tri-Doppler technique shows promise for improving variance estimates under these conditions. However, more data should be collected under unstable conditions to verify this hypothesis.

The virtual tower technique provided mean wind speed and variance estimates at several heights, although these estimates were based on 10 min of data collected at each measurement height each hour. Thus, the virtual tower technique was unable to capture temporal changes in the variance values. This lack of temporal information was not significant under stable conditions, when variance estimates did not change significantly throughout the hour. However, under unstable conditions, the virtual tower technique was unable to capture the changes in variance values that were measured by the WindCube lidar.

In summary, the tri-Doppler technique offers the most advantages over a standard DBS or VAD technique, as it can measure mean wind speeds and turbulence under all stability conditions. The additional turbulence information that can be gained from a tri-Doppler technique are as follows: the measurement of small scales of turbulence under stable conditions and the measurement of accurate turbulence under unstable conditions. Although turbulence can only be measured at one height, recent research has indicated that a profile of turbulence measurements is not necessary for the prediction of wind power production (Bulaevskaya et al. 2015).

How well do the six-beam scanning technique and commonly used scanning techniques measure turbulence under different stability conditions? The

six-beam technique was developed by Sathe (2012) to mitigate the variance contamination that affects commercially available lidars. The experiment we conducted at the Boulder Atmospheric Observatory marked the first time the technique had been validated with sonic anemometers and commercially available lidars. The availability of sonic anemometers at several heights on a 300-m tower provided an unparalleled opportunity to also validate turbulence measurements from the DBS and VAD techniques, which are used by the WindCube and ZephIR lidars, respectively.

The DBS, VAD, and six-beam techniques measured turbulence fairly accurately under stable conditions, although volume averaging resulted in underestimates in comparison to sonic anemometers. In order to measure vertical variance accurately, the lidar beam should be pointed vertically once per scan. The six-beam technique and the WindCube v2 scans include this vertical beam position, although the ZephIR 300 does not.

All three techniques posed problems in the estimation of variance under unstable conditions. The WindCube and ZephIR lidars, which use high elevation angles, were affected by both variance contamination and horizontal heterogeneity across the scanning circle under unstable conditions. These high elevation angles led to a large contribution of the vertical velocity to the horizontal velocity estimates, which in turn, increased the horizontal variance estimates. The overestimation was most significant for the WindCube lidar, as it only takes 4 s to complete a full scan, while the ZephIR takes 15 s, which allows the WindCube to measure larger

values of variance, as it can capture turbulence at higher frequencies. The six-beam technique involves combining the variance of the radial velocity measured at all six beam locations to estimate the u and v variance components, while the w variance is simply taken as the variance of the radial velocity measured by the vertical beam. When different degrees of variance underestimation are present in measurements from the different beam positions, the u and v variance values can be strongly underestimated. This problem may occur because of horizontal heterogeneity across the scanning circle, although further research with model data is needed to investigate the effect of heterogeneity on the variance measured by the different radial beams. Low wind speeds that were measured at the BAO under unstable conditions also may have contributed to inaccurate variance estimates. The six-beam technique still shows promise for reducing variance contamination, although it is highly sensitive to measurement errors at the different beam locations.

How can available lidar data be used in new ways to correct errors in lidar turbulence measurements? Based on data collected during the ARM and BAO experiments, the largest errors in lidar-measured variance often occur under unstable conditions as a result of horizontal heterogeneity within the lidar scanning circle and variance contamination. Thus, two correction techniques were developed which use information from the lidar itself to provide more accurate horizontal variance estimates. The techniques were developed and tested on WindCube lidar data from the ARM site and the BAO.

The first technique used similarity theory to provide a relationship between the ratio of the horizontal variance components to the vertical variance and the Richardson number. Since the WindCube's vertical beam measurements are not affected by horizontal heterogeneity or variance contamination, these measurements could be used along with stability information from the site to estimate values of the u and v variance. The technique reduced variance overestimation at 50 and 100 m at the BAO and at 60 m at the ARM site. Currently, the application of the technique requires measurements from a tower to estimate the Richardson number. However, the WindCube lidar accurately measures a profile of mean wind speeds, so the shear parameter, p, that is often used in wind energy can be estimated from the WindCube lidar. The shear parameter can then be related to Ri through similarity theory, as shown in Newman and Klein (2014).

The second technique involves using the vertical beam data from the WindCube to estimate the value of the vertical velocity at either side of the scanning circle. With this method, horizontal homogeneity in the w component does not need to be assumed, although Taylor's frozen turbulence hypothesis must be applied. The method was tested on the v variance component at the BAO for an afternoon with a nearly constant northerly wind. The technique reduced WindCube variance estimates up to 50%, bringing them much closer to the estimates from the sonic anemometers. The method was also tested on a day with easterly and southeasterly wind directions, indicating, not surprisingly, that the method needs to take the mean wind direction into account.

8.2 Future work

One of the underlying findings of this work was the difficulty of comparing turbulence measurements from different lidars. While mean wind speeds can be measured accurately by all different kinds of lidars with different scanning techniques, the accuracy of turbulence measurements is extremely sensitive to the operating characteristics of each lidar. Therefore, it is recommended that multi- and single-lidar scanning strategy experiments be conducted with identical scanning lidars that have been extensively validated against one another and against sonic anemometer data. The use of identical lidars will allow the effects of scanning circle size, probe volume depth, focus height, and scanning technique on variance estimates to be examined separately.

Another option is to use a lidar simulator with input from an LES to simulate the effects of different scanning techniques on variance estimates. This option will likely be explored through the author's post-doctoral research. Several remote sensing simulators already exist (e.g., Stawiarski et al. 2013; Wainwright et al. 2014; Lundquist et al. 2015), but these simulators have not yet been used to evaluate the accuracy of turbulence measurements with different scanning strategies. The use of a lidar simulator would be very advantageous, as the true turbulence field would be known from the LES and the same flow field could be applied to lidars with different operating characteristics and scanning strategies.

Next, although this dissertation discussed several commonly used scanning strategies, this list of strategies is by no means exhaustive. In their review of

lidar turbulence measurements, Sathe and Mann (2013) discuss several scanning strategies that were originally designed for the measurement of turbulence with Doppler radars. For example, Frisch (1991) showed mathematically that the turbulent components can be measured without the assumption of horizontal homogeneity by using three different elevation angles. These techniques, to the author's knowledge, have not been evaluated with Doppler lidars and could be promising scanning strategies for future evaluation.

Finally, the evaluation of lidar turbulence accuracy should be extended to include specific scenarios that strongly impact wind power production, including ramping events, turbine waking, and terrain-induced flow. This dissertation largely focused on periods of quiescent flow without influences of terrain or strong wind gusts. However, lidars must also be able to accurately measure turbulence under these conditions, which are often associated with outliers in the wind speed distribution at a wind farm (e.g., Jaramillo and Borja 2004). Recent work by Lundquist et al. (2015) examined errors caused by the use of a DBS scan to measure mean wind speeds in the wake of a turbine, although turbulence parameters were not calculated. The measurement of wind and turbulence profiles in complex terrain is an active area of research (e.g., Wharton et al. 2015) and will be a focus of the upcoming DOE-sponsored Wind Forecasting Improvement Project.

Bibliography

Abkar, M. and F. Porté-Agel, 2013: The effect of free-atmosphere stratification on boundary-layer flow and power output from very large wind farms. *Energies*, **6**, 2338–2361.

Albers, A., T. Jakobi, R. Rohden, and J. Stoltenjohannes, 2007: Influence of meteorological variables on measured wind turbine power curves. *European Wind Energy Conference and Exhibition*, Milan, Italy.

Antoniou, I., S. M. Pedersen, and P. B. Enevoldsen, 2009: Wind shear and uncertainties in power curve measurement and wind resources. *Wind Engineering*, **33**, 449–468.

Antoniou, I., R. Wagner, S. Markkilde Petersen, U. Schmidt Paulsen, H. Madsen Aagaard, H. Ejsing Jørgensen, K. Thomsen, P. Enevoldsen, and L. Thesbjerg, 2007: Influence of wind characteristics on turbine performance. *European Wind Energy Conference and Exhibition*, Milan, Italy.

Arya, S. P., 2001: *Introduction to Micrometeorology*, volume 79 of *International Geophysics Series*. Academic Press, Cornwall, UK, 2nd edition, 420 pp.

Balsley, B. B. and K. S. Gage, 1980: The MST radar technique: Potential for middle atmospheric studies. *Pure Appl. Geophys.*, **118**, 452–493.

Banta, R. M., Y. L. Pichugina, and W. A. Brewer, 2006: Turbulent velocity-variance profiles in the stable boundary layer generated by a nocturnal low-level jet. *J. Atmos. Sci.*, **63**, 2700–2719.

Barthelmie, R. J., P. Crippa, H. Wang, C. M. Smith, R. Krishnamurthy, A. Choukulkar, R. Calhoun, D. Valyou, P. Marzocca, D. Matthiesen, G. Brown, and S. C. Pryor, 2013: 3D wind and turbulence characteristics of the atmospheric boundary layer. *Bull. Amer. Meteor. Soc.*, **95**, 743–756.

Bingöl, F., J. Mann, and D. Foussekis, 2009: Conically scanning lidar error in complex terrain. *Meteor. Z.*, **18**, 189–195.

Blanco, M. I., 2009: The economics of wind energy. *Renewable and Sustainable Energy Reviews*, **13**, 1372 – 1382.

Bodine, D., P. M. Klein, S. C. Arms, and A. Shapiro, 2009: Variability of surface air temperature over gently sloped terrain. *J. Appl. Meteor. Climatol.*, **48**, 1117–1141.

Bonin, T. A., W. G. Blumberg, P. M. Klein, and P. B. Chilson, 2015: Thermodynamic and turbulence characteristics of the Southern Great Plains nocturnal boundary layer under differing turbulent regimes. *Bound.-Layer Meteor.*, submitted.

Boyle, G., 2004: *Renewable Energy*. Oxford University Press, 2nd edition, 452 pp.

Bradley, E. F. and R. A. Antonia, 1979: Structure parameters in the atmospheric surface layer. *Quart. J. Roy. Meteor. Soc.*, **105**, 695–705.

Brown, S. S., J. A. Thornton, W. C. Keene, A. A. P. Pszenny, B. C. Sive, W. P. Dubé, N. L. Wagner, C. J. Young, T. P. Riedel, J. M. Roberts, T. C. VandenBoer, R. Bahreini, F. Öztürk, A. M. Middlebrook, S. Kim, G. Hübler, and D. E. Wolfe, 2013: Nitrogen, Aerosol Composition, and Halogens on a Tall Tower (NACHTT): Overview of a wintertime air chemistry field study in the front range urban corridor of Colorado. *J. Geophys. Res.: Atmospheres*, **118**, 8067–8085.

Browning, K. A. and R. Wexler, 1968: The determination of kinematic properties of a wind field using Doppler radar. *J. Appl. Meteor.*, **7**, 105–113.

Bulaevskaya, V., S. Wharton, A. Clifton, G. Qualley, and W. O. Miller, 2015: Wind power curve modeling in complex terrain using statistical models. *Journal of Renewable and Sustainable Energy*, **7**, 013103.

Businger, J. A., J. C. Wyngaard, Y. Izumi, and E. F. Bradley, 1971: Flux-profile relationships in the atmospheric surface layer. *J. Atmos. Sci.*, **28**, 181–189.

Cañadillas, B., A. Westerhellweg, and T. Neumann, 2011: Testing the performance of ground-based wind LiDAR system. *DEWI Magazine*, 58–64.

Calhoun, R., R. Heap, M. Princevac, R. Newsom, H. Fernando, and D. Ligon, 2006: Virtual towers using coherent Doppler lidar during the Joint Urban 2003 Dispersion Experiment. *J. Appl. Meteor.*, **45**, 1116–1126.

Capps, S. B., A. Hall, and M. Hughes, 2014: Sensitivity of southern California wind energy to turbine characteristics. *Wind Energy*, **17**, 141–159.

Cariou, J.-P. and M. Boquet, 2010: LEOSPHERE Pulsed Lidar Principles. Contribution to UpWind WP6 on Remote Sensing Devices.
URL `http://www.upwind.eu/Publications/~/media/UpWind/Documents/Publications/6%20-%20Remote%20Sensing/D611.ashx`

Castellani, F., A. Vignaroli, and E. Piccioni, 2010: Wind shear investigation for site-specific wind turbine performance assessment. *Journal of Energy*, **4**, 1–8.

Chang, W. S., 2005: *Principles of Lasers and Optics*. Cambridge University Press.

Cheong, B. L., R. D. Palmer, T.-Y. Yu, K.-F. Yang, M. W. Hoffman, S. J. Frasier, and F. J. Lopez-Dekker, 2008: Effects of wind field inhomogeneities on Doppler beam swinging revealed by an imaging radar. *J. Atmos. Oceanic Technol.*, **25**, 1414–1422.

Clifton, A., L. Kilcher, J. K. Lundquist, and P. Fleming, 2013: Using machine learning to predict wind turbine power output. *Environmental Research Letters*, **8**, 024009.

Clifton, A. and R. Wagner, 2014: Accounting for the effect of turbulence on wind turbine power curves. *Journal of Physics: Conference Series*, **524**, 012109.

Courtney, M., R. Wagner, and P. Lindelöw, 2008: Commercial lidar profilers for wind energy: A comparative guide. *European Wind Energy Conference*, Brussels, Belgium.

de Vries, O., 1979: Fluid dynamic aspects of wind energy conversion. Technical Report AGARD-AG-243, Advisory Group for Aerospace Research and Development.

Defant, F., 1951: *Compendium of Meteorology*, Amer. Meteor. Soc., chapter on Local Winds. 655–672.

Elliott, D. L. and J. B. Cadogan, 1990: Effects of wind shear and turbulence on wind turbine power curves. *European Community Wind Energy Conference and Exhibition*, Madrid, Spain.

Emeis, S., 2010: *Measurement Methods in Atmospheric Sciences: In-Situ and Remote*. Borntraeger Science Publishers, 257 pp.

—, 2011: *Surface-Based Remote Sensing of the Atmospheric Boundary Layer*, volume 40 of *Atmospheric and Oceanographic Sciences Library*. Springer, 174 pp.

Emeis, S., M. Harris, and R. M. Banta, 2007: Boundary-layer anemometry by optical remote sensing for wind energy applications. *Meteor. Z.*, **16**, 337–347.

Fleagle, R. G. and J. A. Businger, 1980: *An Introduction to Atmospheric Physics*, volume 25 of *International Geophysics Series*. Academic Press, 2nd edition, 432 pp.

Foken, T., 2008: *Micrometeorology*. Springer Science & Business Media, 306 pp.

Frisch, A. S., 1991: On the measurement of second moments of turbulent wind velocity with a single Doppler radar over non-homogeneous terrain. *Bound.-Layer Meteor.*, **54**, 29–39.

Fritts, D. C., C. Nappo, D. M. Riggin, B. B. Balsley, W. E. Eichinger, and R. K. Newsom, 2003: Analysis of ducted motions in the stable nocturnal boundary layer during CASES-99. *J. Atmos. Sci.*, **60**, 2450–2472.

Fuertes, F. C., G. V. Iungo, and F. Porté-Agel, 2014: 3D turbulence measurements using three synchronous wind lidars: Validation against sonic anemometry. *J. Atmos. Oceanic Technol.*, **31**, 1549–1556.

Gage, K. and B. Balsley, 1984: MST radar studies of wind and turbulence in the middle atmosphere. *J. Atmos. Terr. Phys.*, **46**, 739 – 753.

Galperin, B., S. Sukoriansky, and P. S. Anderson, 2007: On the critical Richardson number in stably stratified turbulence. *Atmospheric Science Letters*, **8**, 65–69.

Hahn, C., 1981: A study of the diurnal behavior of boundary-layer winds at the Boulder Atmospheric Observatory. *Bound.-Layer Meteor.*, **21**, 231–245.

Hau, E. and H. Von Renouard, 2013: *Wind turbines: Fundamentals, technologies, application, economics*. Springer Science and Business Media, 879 pp.

Hicks, B. B., 1976: Wind profile relationships from the "Wangara" experiment. *Quart. J. Roy. Meteor. Soc.*, **102**, 535–551.

Højstrup, J., 1993: A statistical data screening procedure. *Measurement Science and Technology*, **4**, 153–157.

Holtslag, A. A. M., 1984: Estimates of diabatic wind speed profiles from near-surface weather observations. *Bound.-Layer Meteor.*, **29**, 225–250.

Howell, J. and J. Sun, 1999: Surface-layer fluxes in stable conditions. *Bound.-Layer Meteor.*, **90**, 495–520.

Huffaker, R. M. and R. M. Hardesty, 1996: Remote sensing of atmospheric wind velocities using solid-state and CO_2 coherent laser systems. *Proceedings of the IEEE*, **84**, 181–204.

International Electrotechnical Commission, 2005a: Wind turbines - Part 1: Design requirements. Technical report, IEC 61400-1.

—, 2005b: Wind turbines - Part 12-1: Power performance measurements of electricity producing wind turbines. Technical report, IEC 61400-12-1.

Jaramillo, O. A. and M. A. Borja, 2004: Wind speed analysis in La Ventosa, Mexico: A bimodal probability distribution case. *Renewable Energy*, **29**, 1613–1630.

Kaimal, J. and J. Finnigan, 1994: *Atmospheric Boundary Layer Flows: Their Structure and Measurement*. Oxford University Press, 289 pp.

Kaimal, J. C., J. C. Wyngaard, Y. Izumi, and O. R. Coté, 1972: Spectral characteristics of surface-layer turbulence. *Quart. J. Roy. Meteor. Soc.*, **98**, 563–589.

Karlsson, C. J., F. Å. A. Olsson, D. Letalick, and M. Harris, 2000: All-fiber multifunction continuous-wave coherent laser radar at 1.55 μm for range, speed, vibration, and wind measurements. *Appl. Opt.*, **39**, 3716–3726.

Kelley, N. D., B. J. Jonkman, and G. N. Scott, 2006: The Great Plains turbulence environment: Its origins, impact and simulation. Technical Report NREL/CP-500-40176., National Renewable Energy Laboratory.

Kelley, N. D., M. Shirazi, D. Jager, S. Wilde, J. Adams, M. Buhl, P. Sullivan, and E. Patton, 2004: Lamar low-level jet project interim report. Technical Report NREL/TP-500-34593, National Renewable Energy Laboratory.

Khadiri-Yazami, Z., L. Pauscher, T. Klaas, S. Prus, and B. Lange, 2013: Realization of a virtual met mast using three pulsed lidars on maneuverable tilting platforms. *European Wind Energy Association Annual Meeting*, Vienna, Austria.

Klein, P., T. A. Bonin, J. F. Newman, D. D. Turner, P. B. Chilson, C. E. Wainwright, W. G. Blumberg, S. Mishra, M. Carney, E. P. Jacobsen, S. Wharton, and R. K. Newsom, 2015: LABLE: A multi-institutional, student-led, atmospheric boundary-layer experiment. *Bull. Amer. Meteor. Soc.*, Accepted.

Kolmogorov, A. N., 1941: The local structure of turbulence in incompressible viscous fluid for very large Reynolds numbers. *Doklady AN SSSR*, **30**, 301–304.

Koscielny, A. J., R. J. Doviak, and D. S. Zrnic, 1984: An evaluation of the accuracy of some radar wind profiling techniques. *J. Atmos. Oceanic Technol.*, **1**, 309–320.

Krishnamurthy, R., A. Choukulkar, R. Calhoun, J. Fine, A. Oliver, and K. Barr, 2013: Coherent Doppler lidar for wind farm characterization. *Wind Energy*, **16**, 189–206.

Kropfli, R. A., 1986: Single Doppler radar measurements of turbulence profiles in the convective boundary layer. *J. Atmos. Oceanic Technol.*, **3**, 305–314.

Kundu, P. K. and I. M. Cohen, 2008: *Fluid Mechanics*. Academic Press, 4th edition, 872 pp.

Lee, X., W. Massman, and B. E. Law, 2004: *Handbook of Micrometeorology: A Guide for Surface Flux Measurement and Analysis*. Kluwer Academic Publishers, 250 pp.

Lenschow, D. H., J. Mann, and L. Kristensen, 1994: How long is long enough when measuring fluxes and other turbulence statistics? *J. Atmos. Sci.*, **11**, 661–673.

Lenschow, D. H., V. Wulfmeyer, and C. Senff, 2000: Measuring second-through fourth-order moments in noisy data. *J. Atmos. Oceanic Technol.*, **17**, 1330–1347.

Lhermitte, R. M. and D. Atlas, 1961: Precipitation motion by pulse Doppler radar. *Proc. Ninth Weather Radar Conf.*, Amer. Meteor. Soc. Boston, MA, 218–223.

Lumley, J. and H. A. Panofsky, 1964: *The Structure of Atmospheric Turbulence*. Wiley-Interscience, 239 pp.

Lundquist, J., L. Glascoe, and J. Obrech, 2010: Operational forecasting based on a modified Weather Research and Forecasting model. *5th International Symposium on Computational Wind Engineering*, International Association for Wind Engineering, Chapel Hill, NC.

Lundquist, J. K., M. J. Churchfield, S. Lee, and A. Clifton, 2015: Quantifying error of lidar and sodar Doppler beam swinging measurements of wind turbine wakes using computational fluid dynamics. *Atmos. Meas. Tech.*, **8**, 907–920.

Machta, M. and M. Boquet, 2013: State of the art of measuring wind turbulence with pulsed lidars. *European Wind Energy Association Annual Meeting*, Vienna, Austria.

Mahrt, L., 1985: Vertical structure and turbulence in the very stable boundary layer. *J. Atmos. Sci.*, **42**, 2333–2349.

Mahrt, L., R. C. Heald, D. H. Lenschow, B. B. Stankov, and I. Troen, 1979: An observational study of the structure of the nocturnal boundary layer. *Bound.-Layer Meteor.*, **17**, 247–264.

Mahrt, L. and D. Vickers, 2006: Extremely weak mixing in stable conditions. *Bound.-Layer Meteor.*, **119**, 19–39.

Mann, J., 1994: The spatial structure of neutral atmospheric surface-layer turbulence. *J. Fluid Mech.*, **273**, 141–168.

Mann, J., J.-P. Cariou, M. S. Courtney, R. Parmentier, T. Mikkelsen, R. Wagner, P. Lindelöw, M. Sjöholm, and K. Enevoldsen, 2008: Comparison of 3D turbulence measurements using three staring wind lidars and a sonic anemometer. *IOP Conference Series: Earth and Environmental Science*, **1**, 012012.

Mann, J., A. Peña, F. Bingöl, R. Wagner, and M. S. Courtney, 2010: Lidar scanning of momentum flux in and above the atmospheric surface layer. *J. Atmos. Oceanic Technol.*, **27**, 959–976.

Markowski, P. and Y. Richardson, 2010: *Mesoscale Meteorology in Midlatitudes*. Wiley-Blackwell, 407 pp.

Mather, J. H. and J. W. Voyles, 2013: The ARM climate research facility: A review of structure and capabilities. *Bull. Amer. Meteor. Soc.*, **94**, 377–392.

Mathisen, J.-P., 2013: Measurement of wind profile with a buoy mounted lidar. *Proceedings of DeepWind Conference*, Trondheim, Norway.

Mikkelsen, T., J. Mann, M. Courtney, and M. Sjöholm, 2008: Windscanner: 3-D wind and turbulence measurements from three steerable Doppler lidars. *IOP Conference Series: Earth and Environmental Science*, **1**, 012018.

Monin, A. and A. Obukhov, 1954: Basic laws of turbulent mixing in the surface layer of the atmosphere. *Contrib. Geophys. Inst. Acad. Sci. USSR*, **151**, 163–187.

Newman, J. F. and P. M. Klein, 2014: The impacts of atmospheric stability on the accuracy of wind speed extrapolation methods. *Resources*, **3**, 81–105.

Newsom, R. K., L. K. Berg, W. J. Shaw, and M. L. Fischer, 2015: Turbine-scale wind field measurements using dual-Doppler lidar. *Wind Energy*, **18**, 219–235.

Oklahoma Climatological Survey, 2013: Oklahoma monthly climate survey: June 2013. Technical report, Oklahoma Climatological Survey.

Panofsky, H. A. and J. A. Dutton, 1984: *Atmospheric Turbulence: Models and Methods for Engineering Applications*. John Wiley & Sons, Inc., 397 pp.

Panofsky, H. A., H. Tennekes, D. H. Lenschow, and J. C. Wyngaard, 1977: The characteristics of turbulent velocity components in the surface layer under convective conditions. *Bound.-Layer Meteor.*, **11**, 355–361.

Pearson, G., F. Davies, and C. Collier, 2009: An analysis of the performance of the UFAM pulsed Doppler lidar for observing the boundary layer. *J. Atmos. Oceanic Technol.*, **26**, 240–250.

Peinke, J., S. Barth, F. Böttcher, D. Heinemann, and B. Lange, 2004: Turbulence, a challenging problem for wind energy. *Physica A: Statistical Mechanics and its Applications*, **338**, 187–193.

Peña, A., C. B. Hasager, S.-E. Gryning, M. Courtney, I. Antoniou, and T. Mikkelsen, 2009: Offshore wind profiling using light detection and ranging measurements. *Wind Energy*, **12**, 105–124.

Peña, A., P.-E. Réthoré, and O. Rathmann, 2014: Modeling large offshore wind farms under different atmospheric stability regimes with the park wake model. *Renewable Energy*, **70**, 164–171.

Petersen, E. L., N. G. Mortensen, L. Landberg, J. Højstrup, and H. P. Frank, 1998: Wind power meteorology. Part I: Climate and turbulence. *Wind Energy*, **1**, 25–45.

Pichugina, Y. L., S. C. Tucker, R. M. Banta, W. A. Brewer, N. D. Kelley, B. J. Jonkman, and R. K. Newsom, 2008: Horizontal-velocity and variance measurements in the stable boundary layer using Doppler lidar: Sensitivity to averaging procedures. *J. Atmos. Oceanic Technol.*, **25**, 1307–1327.

Reynolds, O., 1894: On the dynamical theory of incompressible viscous fluids and the determination of the criterion. *Philosophical Transactions of the Royal Society of London*, **186**, 123–161.

Rohatgi, J. and G. Barbezier, 1999: Wind turbulence and atmospheric stability — their effect on wind turbine output. *Renewable Energy*, **16**, 908–911.

Sathe, A., 2012: *Influence of wind conditions on wind turbine loads and measurement of turbulence using lidars*. Ph.D. thesis, Delft University Wind Energy Research Institute, Delft, The Netherlands.

Sathe, A. and J. Mann, 2012: Measurement of turbulence spectra using scanning pulsed wind lidars. *J. Geophys. Res.: Atmospheres*, **117**, D01201.

—, 2013: A review of turbulence measurements using ground-based wind lidars. *Atmos. Meas. Tech.*, **6**, 3147–3167.

Sathe, A., J. Mann, J. Gottschall, and M. S. Courtney, 2011: Can wind lidars measure turbulence? *J. Atmos. Oceanic Technol.*, **28**, 853–868.

Sathe, A., J. Mann, N. Vasiljevic, and G. Lea, 2015: A six-beam method to measure turbulence statistics using ground-based wind lidars. *Atmos. Meas. Tech.*, **8**, 729–740.

Schlipf, D., D. Trabucchi, O. Bischoff, M. Hofsäß, J. Mann, T. Mikkelsen, A. Rettenmeier, J. J. Trujillo, and M. Kühn, 2010: Testing of frozen turbulence hypothesis for wind turbine applications with a scanning LIDAR system. *International Symposium for the Advancement of Boundary Layer Remote Sensing*, Paris, France.

Schreck, S., J. Lundquist, and W. Shaw, 2008: U.S Department of Energy workshop report: Research needs for wind resource characterization. Technical Report NREL/TP-500-43521, National Renewable Energy Laboratory.

Scorer, R. S., 1949: Theory of waves in the lee of mountains. *Quart. J. Roy. Meteor. Soc.*, **75**, 41–56.

Sheinman, Y. and A. Rosen, 1992: A dynamic model of the influence of turbulence on the power output of a wind turbine. *J. Wind Eng. Ind. Aerodyn.*, **39**, 329–341.

Sjöholm, M., T. Mikkelsen, J. Mann, K. Enevoldsen, and M. Courtney, 2008: Time series analysis of continuous-wave coherent Doppler lidar wind measurements. *IOP Conference Series: Earth and Environmental Science*, **1**, 012051.

Slinger, C. and M. Harris, 2012: Introduction to continuous-wave Doppler lidar. *Summer School in Remote Sensing for Wind Energy*, Boulder, CO.

Song, J., K. Liao, R. L. Coulter, and B. M. Lesht, 2005: Climatology of the low-level jet at the Southern Great Plains Atmospheric Boundary Layer Experiments site. *J. Appl. Meteor.*, **44**, 1593–1606.

Sorbjan, Z., 1989: *Structure of the Atmospheric Boundary Layer*. Prentice Hall New Jersey, 317 pp.

Stawiarski, C., K. Träumner, C. Knigge, and R. Calhoun, 2013: Scopes and challenges of dual-Doppler lidar wind measurements — An error analysis. *J. Atmos. Oceanic Technol.*, **30**, 2044–2062.

Strauch, R. G., D. A. Merritt, K. P. Moran, K. B. Earnshaw, and D. V. De Kamp, 1984: The Colorado wind-profiling network. *J. Atmos. Oceanic Technol.*, **1**, 37–49.

Strauch, R. G., B. L. Weber, A. S. Frisch, C. G. Little, D. A. Merritt, K. P. Moran, and D. C. Welsh, 1987: The precision and relative accuracy of profiler wind measurements. *J. Atmos. Oceanic Technol.*, **4**, 563–571.

Stull, R. B., 1988: *An Introduction to Boundary Layer Meteorology*. Kluwer Academic Publishers, 666 pp.

—, 2000: *Meteorology for Scientists and Engineers*. Brooks/Cole, 2nd edition, 502 pp.

Sumner, J. and C. Masson, 2006: Influence of atmospheric stability on wind turbine power performance curves. *Journal of Solar Energy Engineering*, **128**, 531–538.

Taylor, G. I., 1938: The spectrum of turbulence. *Proceedings of the Royal Society of London. Series A - Mathematical and Physical Sciences*, **164**, 476–490.

Tennekes, H. and J. Lumley, 1972: *A First Course in Turbulence*. MIT Press, 300 pp.

Testud, J., P. Amayenc, M. Chong, B. Nutten, and A. Sauvaget, 1980: A Doppler radar observation of a cold front: Three-dimensional air circulation, related precipitation system, and associated wavelike motions. *J. Atmos. Sci.*, **37**, 78–98.

United States Energy Information Administration, 2014: Annual energy outlook 2014.
URL `http://www.eia.gov/forecasts/aeo/pdf/0383(2014).pdf`

U.S. DOE, 2008: 20% wind energy by 2030: Increasing wind energy's contribution to U.S. electricity supply. Technical Report DOE/GO-102008-2567, Department of Energy.

—, 2015: Atmosphere to electrons.
URL http://energy.gov/eere/wind/atmosphere-electrons

Vanderwende, B. J. and J. K. Lundquist, 2012: The modification of wind turbine performance by statistically distinct atmospheric regimes. *Environ. Res. Lett.*, **7**, 034035.

Vickers, D. and L. Mahrt, 1997: Quality control and flux sampling problems for tower and aircraft data. *J. Atmos. Oceanic Technol.*, **14**, 512–526.

Wagner, R., I. Antoniou, S. M. Pedersen, M. S. Courtney, and H. E. Jørgensen, 2009: The influence of the wind speed profile on wind turbine performance measurements. *Wind Energy*, **12**, 348–362.

Wagner, R., C. Michael, L. Torben, and P. Uwe, 2010: Simulation of shear and turbulence impact on wind turbine performance. Technical report, Risø National Laboratory for Sustainable Energy, Roskilde, Denmark.

Wainwright, C. E., P. M. Stepanian, P. B. Chilson, R. D. Palmer, E. Fedorovich, and J. A. Gibbs, 2014: A time series sodar simulator based on large-eddy simulation. *J. Atmos. Oceanic Technol.*, **31**, 876–889.

Weitkamp, C., 2005: *Lidar: Range-Resolved Optical Remote Sensing of the Atmosphere*, volume 102 of *Springer Series in Optical Sciences*. Springer Science & Business Media, 455 pp.

Wharton, S. and J. K. Lundquist, 2012a: Assessing atmospheric stability and its impacts on rotor-disk wind characteristics at an onshore windfarm. *Wind Energy*, **15**, 525–546.

—, 2012b: Atmospheric stability affects wind turbine power collection. *Environ. Res. Lett.*, **7**, 014005.

Wharton, S., J. F. Newman, G. Qualley, and W. O. Miller, 2015: Measuring turbine inflow with vertically-profiling lidar in complex terrain. *J. Wind Eng. Ind. Aerodyn.*, In press.

Wilczak, J. M., S. P. Oncley, and S. A. Stage, 2001: Sonic anemometer tilt correction algorithms. *Bound.-Layer Meteor.*, **99**, 127–150.

Wilks, D. S., 2006: *Statistical Methods in the Atmospheric Sciences*. Elsevier, New York, NY, 2nd edition, 627 pp.

Wyngaard, J. C., 2010: *Turbulence in the Atmosphere*. Cambridge University Press, 393 pp.

Appendix A: List of Acronyms

A2e	Atmosphere to Electrons
ABL	Atmospheric boundary layer
AEP	Annual energy production
AGL	Above ground level
ARM	Atmospheric Radiation Measurement
BAO	Boulder Atmospheric Observatory
DBS	Doppler beam-swinging
DOE	Department of Energy
IEC	International Electrotechnical Commission
JU2003	Joint Urban 2003
LABLE	Lower Atmospheric Boundary Layer Experiment
LATTE	Lower Atmospheric Thermodynamics and Turbulence Experiment
LES	Large-eddy simulation
LLJ	Low-level jet
LLNL	Lawrence Livermore National Laboratory
MO	Monin-Obukhov

NCAR	National Center for Atmospheric Research
OU	University of Oklahoma
RHI	Range-height indicator
RIN	Relative intensity noise
RMS	Root-mean square
RMSE	Root-mean squared error
SNR	Signal-to-noise ratio
TI	Turbulence intensity
TKE	Turbulence kinetic energy
UTC	Coordinated Universal Time
VAD	Velocity-azimuth display

Appendix B: Weather Conditions During LATTE

Date	Weather
2/14/2014	
2/15/2014	Fairly strong southwesterly winds in morning, shifting to northeasterly winds in the afternoon with cold frontal passage.
2/16/2014	
2/17/2014	Cold frontal passage in early morning hours and strong westerly winds in morning.
2/18/2014	
2/19/2014	
2/20/2014	Strong westerly winds in afternoon. Some light snow around 0400 UTC with overnight cloudiness and cold frontal passage.
2/21/2014	
2/22/2014	Clear skies most of day with some cloudiness in late afternoon/evening associated with cold frontal passage.
2/23/2014	Weak variable winds, snow between 0300 and 0600 UTC.
2/24/2014	
2/25/2014	
2/26/2014	Snow from 0200 to 0500 UTC followed by clear skies all day.
2/27/2014	
2/28/2014	Cold frontal passage in late afternoon.
3/1/2014	Fog until 1200 UTC, snow and low clouds most of day
3/2/2014	Low clouds and some intermittent snow until 1700 UTC, followed by mostly clear skies. Warm frontal passage in afternoon.
3/3/2014	
3/4/2014	
3/5/2014	Low clouds and snow between 0300 and 0900 UTC, clear skies all day afterward.
3/6/2014	
3/7/2014	Low clouds and snow after 1400 UTC. Cold frontal passage in afternoon.
3/8/2014	Snow until 0400 UTC, clouds lift and clear out after 1200 UTC.
3/9/2014	

3/10/2014	
3/11/2014	High clouds move in around 1200 UTC, snow starts at 1700 UTC. Cold frontal passage in early morning hours.
3/12/2014	
3/13/2014	
3/14/2014	
3/15/2014	Cold front moves through around 1700 UTC.
3/16/2014	
3/17/2014	Cold frontal passage in late afternoon.
3/18/2014	
3/19/2014	
3/20/2014	
3/21/2014	Cold frontal passage around 1200 UTC.
3/22/2014	Cold frontal passage around 0600 UTC. Some snow during late afternoon.
3/23/2014	
3/24/2014	Cold frontal passage around 0400 UTC.
3/25/2014	
3/26/2014	Scattered light showers in area between 2000 and 2200 UTC causing periods of gusty/shifting winds.

Table B.1: Summary of weather conditions during LATTE.